Strain effects on phase transitions in 2H-$NbSe_2$ and $Ca_3Ru_2O_7$

Jedrzej Robert Wieteska

Submitted in partial fulfillment of the
requirements for the degree of
Doctor of Philosophy
under the Executive Committee
of the Graduate School of Arts and Sciences

COLUMBIA UNIVERSITY

2021

Abstract

Strain effects on phase transitions in 2H-$NbSe_2$ and $Ca_3(Ru_{1-x}Ti_x)_2O_7$

Jedrzej Robert Wieteska

Strain control of correlated electron phenomena has been a theme of condensed matter research in recent years. Two primary areas of investigation have been controllable symmetry breaking and measurements of susceptibility with respect to elastic deformation and in this thesis we present an example of each. In 2H-$NbSe_2$ explore the effect of lattice anisotropy on the charge-ordered superconductor. Using a novel strain apparatus, we measure the superconducting transition temperature T_{sc} as a function of uniaxial strain. It is found that T_{sc} is independent of tensile(compressive) strain below a threshold of 0.2% (0.1%), but decreases strongly with larger strains with an average rate of 1.3 K/% (2.5 K/%). Transport signatures of charge order are largely unaffected as a function of strain. We employ theoretical considerations to show that the change in the behavior of T_{sc} with strain coincides with a phase transition from 3Q to 1Q charge order in the material. The spectral weight on one of the Fermi surface bands is found to change strongly as a consequence of this phase transition, providing a pathway to tune superconducting order. In the bilayer ruthenate $Ca_3(Ru_{1-x}Ti_x)_2O_7$, a material that is unique among correlated insulators for its hybrid improper ferroelectricity and, at elevated temperatures, transitioning to a polar metallic phase, we investigate phase textures and their susceptibility to strain. Through multi-messenger low-temperature infrared and Kelvin probe nano-imaging, we reveal a spontaneous striped texture of coexisting insulating and

metallic domains in single crystals across their insulator-metal phase transition at T=50-100K. Under in situ uniaxial strain, we image anisotropic nucleation and growth of these domains, rationalized through on-demand control of a spontaneous Jahn-Teller distortion. Through spatially correlative transmission electron microscopy and nano-scale strain mapping, we also reveal the selective interplay between this textured phase coexistence and domain boundaries between polar twins in these crystals. We study the strain susceptibility of the striped phase mixture and explain our results in terms of homogeneous phase susceptibilities and the strain susceptibility of domains. We study the anisotropy in bulk response functions (resistivity and elastosusceptibility) and we find that the results are consistent with a network model of the phase texture. We also perform low-temperature infrared nanoimaging and elastosusceptibility of the nonequilibrium current-driven metal-insulator transition in $Ca_3(Ru_{1-x}Ti_x)_2O_7$. Our results are consistent with the emerging consensus explanation in terms of Joule heating.

Table of Contents

List of Figures

Acknowledgements

The past six years have been an incredibly rewarding time. I would like first and foremost, to thank my advisor, Prof. Abhay Pasupathy, for accepting me as his student and guiding my research for this entire time. It has been as exciting an experience as I could have hoped! I would like to thank then-postdocs Zurab Guguchia and Alex McLeod for their collaboration on the projects described in this thesis, and Ben Foutty and Ben Mazel for working alongside me during their undergraduate studies. I learned a tremendous amount from all of you! I would like to thank Professors Dmitri Basov, Andrew Millis and Tomo Uemura for their and their groups' collaboration on the projects that constitute this thesis. I am also grateful to Professors Aleiner and Altshuler for their lecture series at Columbia; to Professors Marianetti, Flicker and Wenzel for explaining my results on $2H$-$NbSe_2$; to Professor Danny Shahar for invaluable experimental help; and to Professors Littlewood, Moller and Chau who supervised my undergraduate research projects. Finally, I would like to thank my friends at Columbia who include, in no particular order, Dennis Wang, Apoorv Jindal, Alex Kerelsky, Evan Telford, Sai Sunku, Konrad Wenz, Minghao Cheng, Augusto Ghiotto, Sara Shabani and Zurab Guguchia, for their support and for making this time livelier than it would otherwise have been!

Chapter 1: Strain in condensed matter physics

Strain a completely generic concept in solids. A solid consists of atomic cores and electrons. The generic Hamiltonian of a solid state system is

$$\mathcal{H} = \mathcal{H}_{\text{atom}} + \mathcal{H}_{\text{el}} + \mathcal{H}_{\text{el-atom}} \tag{1.1}$$

In this thesis we focus on electronic behavior through measuring electronic response functions in two solid state systems (2H-$NbSe_2$ and $Ca_3(Ru_{1-x}Ti_x)_2O_7$) and correlate the results to our expectations based on assumptions about the particular form of the generic Hamiltonian which applies. At a high level application of strain can be thought of as modifying the atomic system and how, via $\mathcal{H}_{\text{el-atom}}$, it influences the electronic component.

1.1 Correlated electron systems

A basic tenet of our understanding of electronic motion in crystalline materials is that under the vast majority of circumstances electrons act as if they were single particles who do no interact with each other. This is a seemingly contradictory notion because when one computes the Coulomb interaction between two electrons in a solid over a distance that, on average, separates an electron from the other closest nearby electron, that energy is on the order of the kinetic energy of the electron and therefore one expects it to play a role on par with the kinetic part in determining their motion. Much effort was expended in the latter half of the previous century to establish a theoretical understanding of why the electrostatic interaction between electron often does not change their qualitative behavior within a solid.

In a small but extremely interesting subset of solid state phenomena the electron-electron interaction plays the chief role by driving a system into a new phase, be it magnetism, su-

perconductivity or charge order. Such systems are typically referred to as correlated electron systems. Examples of correlated electron systems include the copper oxide and iron pnictide materials where high temperature superconductivity is found, the manganite compounds that exhibit colossal magnetoresistance and the vanadates and ruthenates that exhibit a rich gamut of phenomena associated with interaction-driven insulation. It so happens that these classes of materials are extremely complex, with multiple phenomena occurring simultaneously, whether by accident, cooperatively or in competition with each other, and that makes their experimental and theoretical understanding a Herculean task.

1.2 Tuning parameters in condensed matter physics

Following the oft-cited credo of Richard Feynman [1] a popular approach to this problem is to "tune" the parameters of these systems and understand how the system responds. Concretely, a common tuning parameter in such studies is doping: the injection of a controlled amount of electronically active impurities that in effect alter the electron density of the system and shift its Fermi level either up or down. Other common examples of tuning parameters are hydrostatic pressure, controlled disorder, dimensionality and the subject of this thesis, uniaxial strain.

Every tuning parameter has its advantages and disadvantages. Primarily, physicists are interested in whether the application of the stimulus produces changes in electronic behavior that are of interest to us. Secondly, it is important for a correct interpretation of results to have a detailed understanding of the situation. For example, in doping control studies a recurring question is whether or not the level of disorder in the system varies with the concentration of dopants. Thirdly, the set of measurement tools that can be applied is particular to any given tuning parameter. For example, surface sensitive measurements are difficult to perform on samples under hydrostatic pressure. The inability to perform torque magnetometry measurements on thin samples due to their small volume is a practical

[1] "What I cannot create I do not understand"

limitation to the information that can be gained using dimensionality control.

1.3 Spatial symmetry breaking in correlated electron systems

A recent area of emphasis in the field of correlated matter has been symmetry breaking. Symmetry breaking phenomena have been well known to occur and have been the subject of copious investigations in the field of statistical physics generally [1] and in the context of condensed matter specifically [2]. This reinvigorated interest from the correlated electron community is rooted in their recent discovery in the high-temperature superconductors [3, 4] leading to broader questions about the scenarios that can take place when these phases occur in the vicinity or concurrently with phenomena such as superconductivity, Mott insulation and magnetism.

1.4 Uniaxial strain as a symmetry breaking perturbation

The concept of a uniaxial strain measurement is study a system's response to an external field, anisotropic strain, ϵ, that directly breaks the symmetry. It is typically of interest to study the variation in the system's behavior as function of the strength of the symmetry breaking field, in which case one would like the application of uniaxial strain to be tunable within some reasonable range.

1.5 Uniaxial strain application through physical stretching

Physical stretching is the most compelling way to realize a tunable uniaxial strain in a sample. Other ways include epitaxial strain where one grows a (thin but possibly thick enough to be considered three dimensional) film on top of a substrate and the film experiences a strain field due to the binding between the film and the substrate enforcing a match. There are multiple advantages of physical stretching over an epitaxial strain application. Firstly, growth of epitaxial films of high electronic quality is a task that requires a tremendous amount

of expertise and patience whereas one could, in principle, apply a mechanical deformation to any bulk crystalline sample. Secondly, the physical deformation method involves repeated measurements of the same sample which means that, to a good approximation, other system parameters - most pertinently, the disorder distribution - are held constant throughout the experiment making the uniaxial strain effect on system properties easier to isolate.

Generally speaking there exist in the literature two types of studies on crystalline systems that involve the application of tunable uniaxial strain: elastosusceptibility and strain control studies.

1.6 Elastosusceptibility measurements

The concept of elastosusceptibility, pioneered by [5], concerns the the linear response part of the dependence of a system observable, O, which is typically resistance or magnetic susceptibility, to strain of a particular orientation. Concretely, the elastosusceptibility of the observable O is defined by

$$\chi_O = \frac{1}{O} \left. \frac{dO}{d\epsilon} \right|_{\epsilon \to 0} \quad (1.2)$$

One measures this quantity in the linear response limit, i.e. for a range of strain ϵ small enough that $O(\epsilon) \propto \epsilon$. In a set of important works χ_O was studied over a region of a material's phase diagram that contains phenomena of interest such as phase transitions. In the phase transition case, the second step is to relate the elastosusceptibility with the susceptiblity of the order parameter ψ of the phase transition, $\chi_O \propto \chi_\psi$, i.e. an argument based on microscopic considerations must be made to argue that $\chi_O \propto \chi_\psi$ or possibly a more complicated functional form $\chi_O \propto f(\chi_\psi)$. The measurement of χ_O thus places constrains on the possible form of the theory of the phase transitions to ones that are consistent with the experimental χ_ψ obtained from susceptibility.

Prominent studies that utilized this technique in recent years include [5]. The novel contributions of this thesis to that body of literature are measurements of elastosusceptibility

across phase lines in $Ca_3(Ru_{1-x}Ti_x)_2O_7$, including as function of a nonequilibrium parameter (d.c. current). The phase transitions involved are strongly first order so to explain our results we introduce a framework to model the elastosusceptibility of a phase mixture, accounting for the possibility that the phase composition is affected by strain.

1.7 Ultra-high strains

The application of a high (to provide a ballpark: $> 0.1\%$) uniaxial strain can be regarded as a means of "tuning" a material. Meaning that as long as the deformation is performed in an equilibrium fashion one essentially obtains a "new" solid state system which differs from the original system by a deformation of the lattice parameters by a known amount. In principle, all other parameters such as, crucially, disorder distribution, are unchanged. In practice, there is always a small degree of disorder introduced by the application of ultra-high strains (see Chapter 3) but it is generally a much weaker effect than the effect of doping.

The maximum strains one can apply through this technique are a few % at most. In most materials that kind of strain does not create effect of particular interest. For example, in a high-density metal, crudely speaking one expects the effect of strain perturbation to be to modulate the density of carriers; or in a large bandgap insulator one expects the effect of such a perturbation to be to a modulation of the size of the energy gap. While those phenomena may be of interest in any particular case, this thesis and the literature which surrounds it targets the instances where a strain perturbation may have a dramatic and exciting effect: phase transitions.

In CTRO we use strain to modulate the composition of a metal-insulator phase mixture by $\pm 40\%$. In 2H-$NbSe_2$ we drive a system across a phase transition between two charge ordered states of differing symmetry. To provide an example of others' work that I personally found particularly appealing, in [6] the authors use uniaxial strain to drive a material ($ZrTe_5$) through a topological phase transition.

Chapter 2: Experimental methods

This chapter describes the experimental methods that were used to perform the measurements on 2H-$NbSe_2$ and $Ca_3(Ru_{1-x}Ti_x)_2O_7$. It contains two main sections: a description of the novel strain application apparatus which was developed as part of this thesis and, secondly, a description of the Scanning Near-field Optical Microscopy technique which we utilized in the series of experiments on $Ca_3(Ru_{1-x}Ti_x)_2$.

2.1 Strain application technique

2.1.1 Strain device design

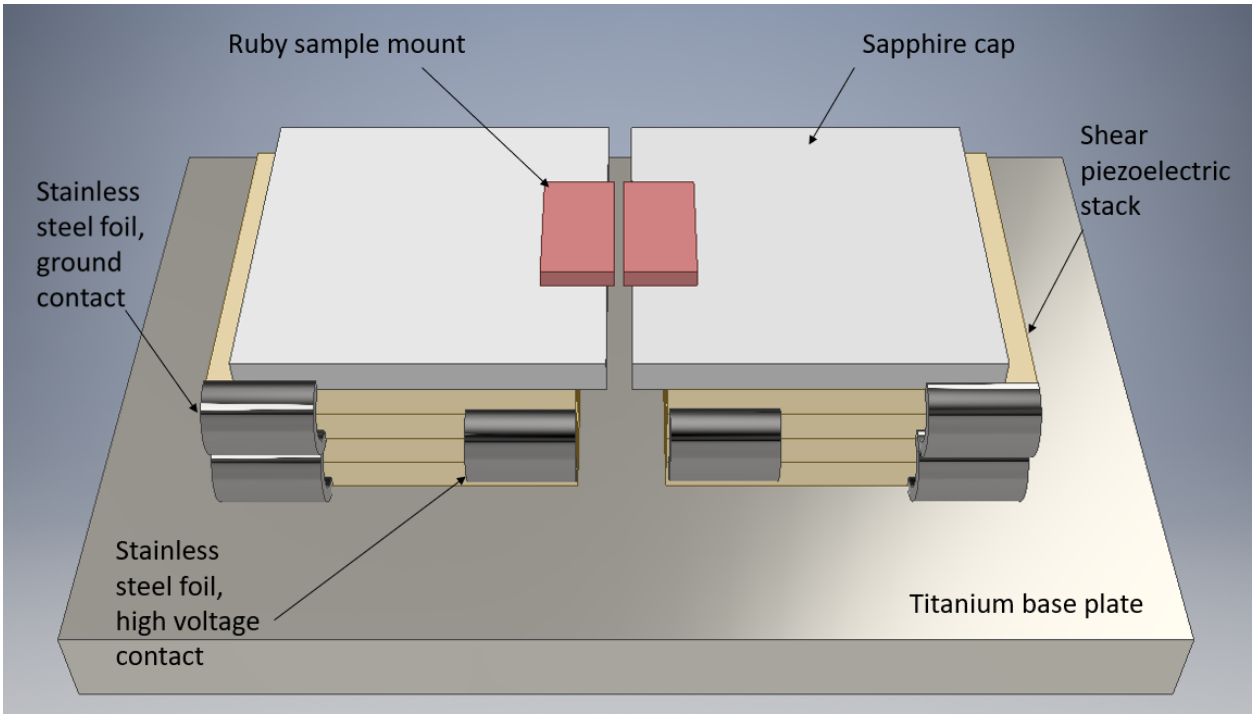

Figure 2.1: A schematic outline of the strain application device with annotations. A detailed description of the components is provided in the main text.

The strain application device is composed of two adjacent stacks of piezoelectric shear actuators. Each stack consists of four Noliac CSAP02 shear piezoelectric actuators. we fasten the actuators together using H20E silver epoxy, Hysol 1C epoxy, and stainless steel foil. The stacks are glued to a titanium plate with about a 1.5 mm gap between them. To insulate a sample from the large voltages applied to the piezoelectric elements each is capped with sapphire squares.

Two small sapphire rectangles are mounted on top of these caps, hanging over the gap between the stacks. These are glued down aligned with a typical gap of 50-150 μm. The sample is mounted across this gap and fastened down with epoxy such that the epoxy runs up to the edge of the sapphire rectangles.

2.1.2 Calibration

To zeroth order the strain applied to the region of the sample under measurement is given by

$$\varepsilon_{xx} = \frac{\Delta L}{L} \tag{2.1}$$

Given the dimensions of the device a continual measurement of sample length is a significant technical challenge. Below we outline the series of factors included in the strain estimates we present in the works presented here.

2.1.3 Differential Thermal Contraction

Given that the length scale of displacements that take place during strain application is on the order of 10^{-7} m and the experiments take place at cryogenic temperatures, we studied the effect of thermal contraction on these devices. We used COMSOL Multiphysics to model the thermal contraction of the assembly of parts that constitute the device, including sapphire caps[7], the PZT (lead zirconate titanate) actuators[8], and the titanium base. We note that while the expansion mode of piezoelectric materials is known to have significant temperature dependence, our device depends on the shear mode [9]. There are two key findings of

this model. Firstly, that the majority of thermal contraction takes place between room temperature and 85K, such that this is a temperature-independent effect in the temperature range of this study. Secondly, for a 2H-$NbSe_2$ crystal of the typical dimensions used in this study (details in Chapters 2 and 3 for 2H-$NbSe_2$ and $Ca_3(Ru_{1-x}Ti_x)_2$, respectively) the effect of thermal contraction to apply a small compression of 0.08% to the sample.

2.1.4 Temperature Dependence of Shear Actuators

It is known that piezoelectric coefficients respond strongly to temperature. d_{15}, the relevant coefficient for shear actuators, has been measured at cryogenic temperatures [10]. However, due to the large voltages applied in this study, we must consider nonlinear components of d_{15}, i.e., the way this coefficient depends itself on the field applied when that field is large [11, 12]. We therefore performed a calibration of our devices via a capacitative method akin to that used by Bukhari, et. al. [10]. The results are summarized in panel b of figure 1 in the main text. In the course of collecting the data in this study the voltage applied to piezoelectric actuator was adjusted according to this calibration so as to provide a constant strain to the sample as temperature was varied.

Figure 2.2: A sample of raw capacitance data. At the temperatures relevant to this study piezoelectric displacement is linear as function of applied voltage. The gradient of the dependence lessens with decreasing temperature.

2.1.5 Higher-order Strain Estimation

There are two significant mechanical effects for which one must account to accurately estimate strain transmission to the sample.

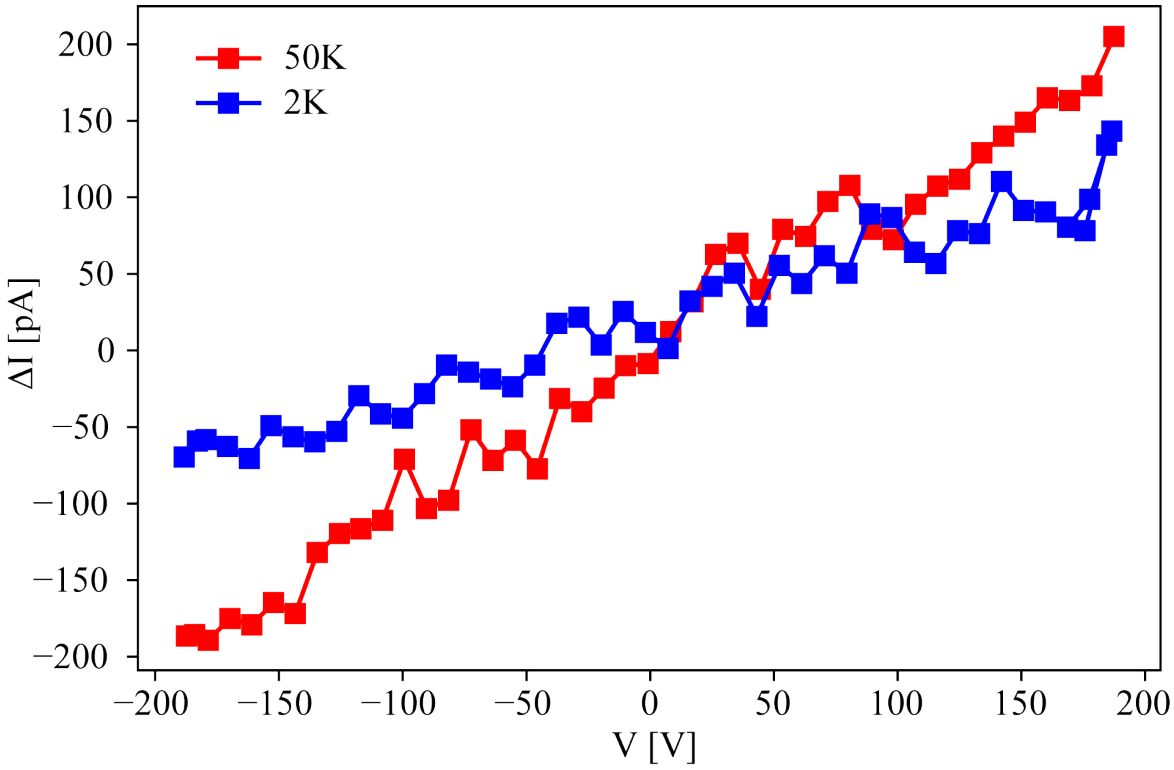

Stiffness of piezoelectric actuators

This is the effect of the sample pushing back on the actuators when a voltage is applied that induces them to move. We model this behaviour within a a linear response framework. If ΔL_0 is the free stroke motion correspondent to an applied voltage, the actual motion is

$$\Delta L = \Delta L_0 \left(\frac{k_p}{k_p + k_s} \right) \tag{2.2}$$

where k_p is the axial stiffness of the piezoelectric and k_s is the axial stiffness of the sample. Taking E to be the Young's modulus of $NbSe_2$ (as an example), and A and l to be the cross-sectional area and length of the area respectively, $k_s = \frac{EA}{l}$. The axial stiffness of the shear piezo is given by $\frac{F_b}{\delta}$ where δ is the free-stroke displacement and F_b is the blocking force. Using the model of shear piezoelectrics provided in [13] , we take $k_p = \frac{t_p}{s_{44}^E}$ where t_p is the thickness of the piezoelectric plate and s_{44}^E is a component of the elastic compliance matrix. Inserting numerical values [14, 15] into these formulae we find that this effect reduces our

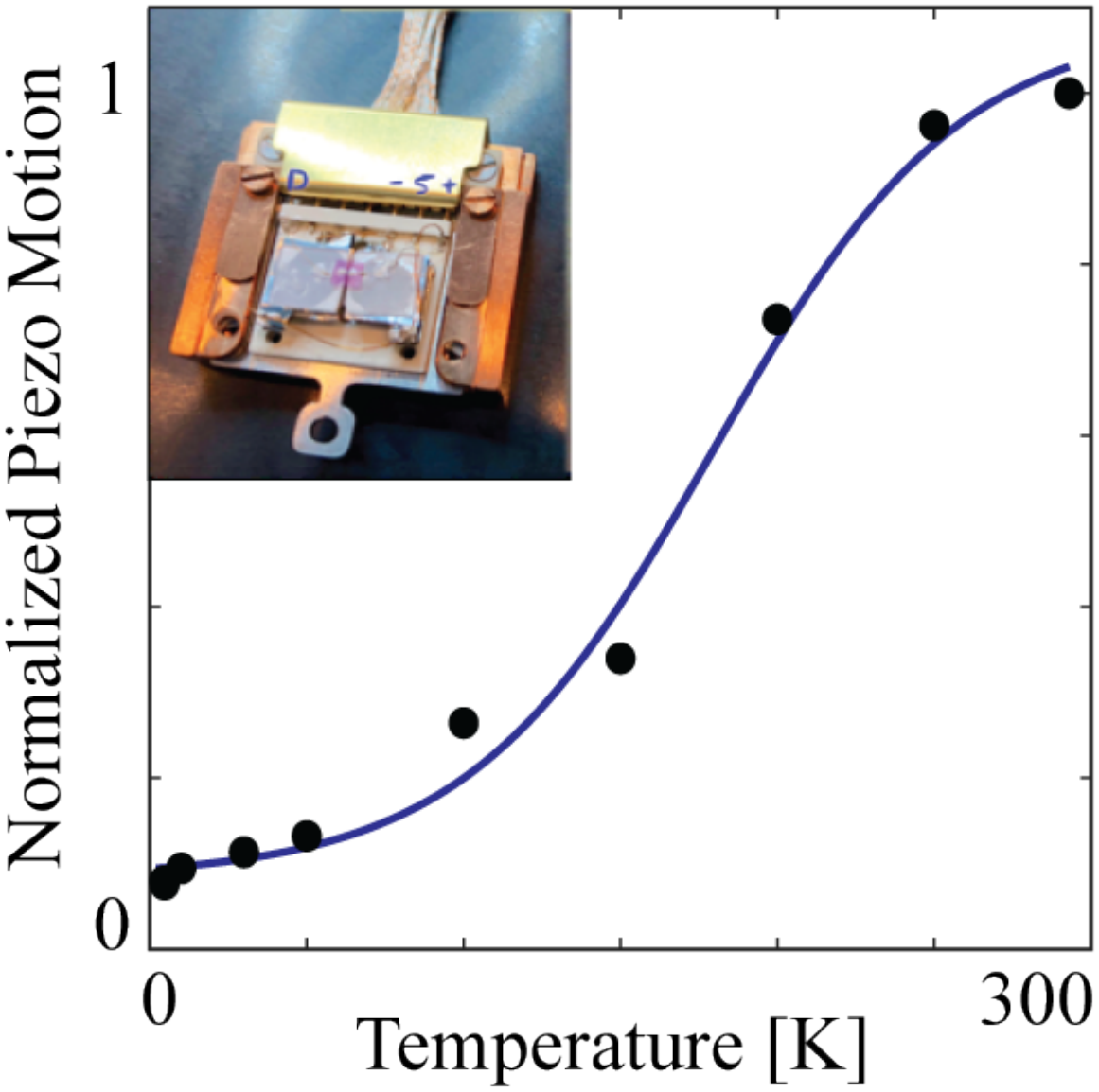

Figure 2.3: Temperature dependence of normalized motion of Noliac CSAP02 shear piezoelectric actuator.

strain applied by a factor of $2-6\%$.

2.1.6 Inhomgeneous strain at the boundary and epoxy effects

Our estimates in this section closely track the discussion in [16]. The strength of the epoxy binding the sample to the piezoelectric plates impacts strain transmission to the sample. Finite element analyses presented by [16] demonstrate that the "bridge" geometry

used in Hicks et al.'s work and the current study is essentially homogeneous in the case of a rectangular sample with a large aspect ratio. However, there is a region of inhomogeneity outside the gap region where the strain field continuously varies from high to low. The lengthscale of that region is set by the elastic constants of the material and sample thickness. For the geometries employed in this paper this is a considerable effect, whose result is to reduce our former strain estimate is reduced by 42%.

2.2 Scanning Near-field Optical Microscopy

Scanning near-field optical microscopy (SNOM) is an atomic force microscope (AFM)-based technique enables imaging of surface optical properties at variable temperatures [17, 18, 19] below the diffraction limit [20], with a resolution strictly limited only by the geometric sharpness of the metallic AFM probe. In this section we provide an overview of the technical aspects of the technique. Further technical details are provided in Chapter 3 where we describe results obtained with SNOM.

In Chapter 3 we present 25 nm-resolved imaging of the locally back-scattered near-field signal amplitude (abbreviated to nano-IR signal, or σ) collected at low temperatures (down to T = 50 K) using a custom-designed cryogenic near-field optical microscope (cryo-SNOM) [21]. In the measurements presented in this thesis measurements, focused infrared light is incident upon and scattered from the metallic tip of an atomic force microscope (AFM) probe (SCM-PtSi, Bruker Nano) oscillating at a frequency $\sim$ 70 kHz near the sample surface while the microscope is operated in amplitude modulation AFM feedback. The back-scattered radiation from the probe encodes information about the optical permittivity of the sample at the frequency of the laser source. Back-scattered radiation is registered by a liquid nitrogen-cooled mercury cadmium telluride photodetector and resolved from the background through Michelson interferometry in a pseudo-heterodyne detection scheme[22]. To a first approximation, the amplitude of back-scattered radiation modulated at high harmonics ($n > 1$) of the cantilever oscillation frequency provides a proportional measure of the local

nearfield optical response of the sample and, by implication, its optical conductivity resolved at the 20-nm scale. However, previous works implicate further multiplicative in fluence from farfield reflectivity of the sample surrounding the probe, with possibility to distort the scale of even demodulated nano-IR signals when scanning length scales of the sample comparable to the wavelength of illuminating radiation (~10 microns) [23]. It is also recognized that nano-IR signals at higher harmonics n provide increasingly strong contrast to material properties [24]. Thus, to remove the influence of far-field reflectivity, we take the nano-IR signal as the ratio of demodulated back-scattered signals demodulated at harmonics $n = 3$ and $n = 2$, thus removing any commonly multiplicative "far-field factor".

Leveraging electrical conductivity of the nano-IR probe, for select images, Kelvin probe force detection is conducted simultaneously to nanoIR imaging using the frequency-modulation Kelvin probe force microscopy (FM-KPFM) method[25]. This method is acknowledged to afford artifact-free detection of the contact-potential difference, $\Delta\Phi = \Phi_{sample} - \Phi_{tip}$ in our case, resolved at length scales comparable to the tapping amplitude of the cantilevered probe.

Chapter 3: Effect of anisotropic strain on a charge-ordered superconductor

3.1 Overview

Unconventional superconductivity is often found in the proximity of symmetry-breaking phases. In cuprate and pnictide high-T_c superconductors there exist multiple phases that break translational [26, 27, 3, 28] and rotational [5, 29, 30] symmetries. Furthermore, rotational symmetry breaking has been reported in the superconducting state of intercalated Bi_2Se_3 [31, 32], in the heavy fermion superconductor URu_2Si_2 [33] and in the recently discovered twisted magic angle bilayer graphene superconductor [34, 35, 36]. The broad question of interplay between symmetry breaking and superconductivity remains the subject of intense debate [37].

3.1.1 Effect of anisotropic strain on superconductivity in 2H-$NbSe_2$

The main result of this chapter change in the superconducting critical temperature T_{sc} in $NbSe_2$ under large, continuously tunable uniaxial strain is the subject of this chapter. Our main result is to reveal a large, negative uniaxial strain effect on T_{sc} in highly strained samples. These data can be interpreted in terms of differences in Fermi surface competition between superconductivity and charge order in the C_3-symmetric and C_3 symmetry-breaking charge ordered phases.

3.2 The unconventional aspects of superconductivity in 2H-$NbSe_2$

The focus of this chapter is the effect of uniaxial strain on superconductivity and, relatedly, charge order in in 2H-$NbSe_2$. We would like to place this work in the millieu of the

literature associated with unconventional superconductivity. This leads us to the question of what an unconventional superconductor is and whether 2H-$NbSe_2$ qualifies as one.

In this thesis we take an unconventional superconductor to be one which deviates in some way from the class of superconductors studied in the early days of the field such as lead or aluminum. On the one hand 2H-$NbSe_2$ bears a similarity to these materials in that it is a matter of widespread belief that the origin of the superconductivity in 2H-$NbSe_2$ is the electron-phonon interaction. Researchers have successfully described the phenomenology of the superconducting state in 2H-$NbSe_2$ using conventional theories of the Bardeen-Cooper-Schrieffer type. The deviation in the case of 2H-$NbSe_2$ is the presence of charge ordering concurrent with superconductivity and the fact that the two phases interact, as discussed in detail in the body of this chapter.

3.3 Overview of strain effects on superconductivity in superconductors

In recent years the application of symmetry-breaking strains to unconventional superconductors has been a fruitful line of investigation. It is a phenomenological fact about the vast majority of known unconventional superconductors that the superconductivity arises in a region of the phase diagram into which one may tune with parameters such as doping or hydrostatic pressure.

In one sense doping is the most powerful way of tuning these materials because it yields large bulk samples of the material, with the chemical potential adjusted, which may be studied in much the same way as the stochiometric material without the hassle of a pressure cell or a strain stage. However, in reality doping, in addition to tuning the chemical potential, adjusts other system parameters such as until cell size and, crucially, the disorder level to which phenomena such as superconductivity and charge or spin ordering are sensitive. Hydrostatic pressure is a cleaner tuning parameter and indeed often produces the same zoo of phase when applied to a compound in a series that exhibits unconventional superconductivity but the application of hydrostatic pressure is a significant experimental feat requiring the

participation of experts.

3.3.1 Order parameter determination in $Ba(Fe_{1-x}Co_x)_2As_2$

In the iron-pnictides, superconductivity often appears in tandem with a nematic transition in which the crystal structure switches from C_4 symmetric (tetragonal) to C_2 symmetric (orthorhombic). The sixty four million dollar question was what drove this transition: whether it was a plain structural transition whose order parameter was some combination of the phonon degrees of freedom, or whether an electronic component was involved which acted in concert with the phonons.

In brief, [5] argue theoretically that the in-plane resistivity anisotropy $\eta = (\rho_a - \rho_b)/(\rho_a + \rho_b)$ is proportional to the order parameter for the nematic transition. They then measure the elastosusceptibility of the said anisotropy for a range of temperature and doping level, which yields a measure of the elastosusceptiblity of the order parameter. The key finding of this work is the presence of a divergence concommittant in location with the nematic transition (see 3.1). It is then argued that the symmetry-dictated Landau theories that are consistent with the susceptibility measurements must include an electronic component in the order parameter used for the nematic transition. This finding sent shockwaves through the high-temperature superconductivity research community and resulted in a body of work that attempts to explain the microscopic origin of the nematic order parameter and its connection to superconductivity. [38]

The key aspect of [5] is that the elastosusceptibility measurement provided a direct probe of the system's propensity broken rotational symmetry and hence of the order parameter of the transition. This landmark work established uniaxial strain experiments as a go-to tool for probing the responses of a system to incremental breaking of rotational symmetry.

3.3.2 Uniaxial strain as an axis of the phase diagram in $Ba(Fe_{1-x}Co_x)_2As_2$

For high strains, uniaxial strain acts as a tuning parameter for the transition [40, 39, 41]. One way to regard these experiments is to view them as investigating the non-linear branch of the susceptibility of resistivity to anisotropic strain. Alternatively one may view these experiments as series of "tuned" systems: sequences of $Ba(Fe_{1-x}Co_x)_2As_2$ with incrementally different lattice spacings.

The spectacular finding of these studies is that the superconducting phase in $Ba(Fe_{1-x}Co_x)_2As_2$ is entirely tunable with anisotropic strain 4.1, up to the point of complete suppression of the superconducting phase. Crudely speaking this is in line with the expectation one has

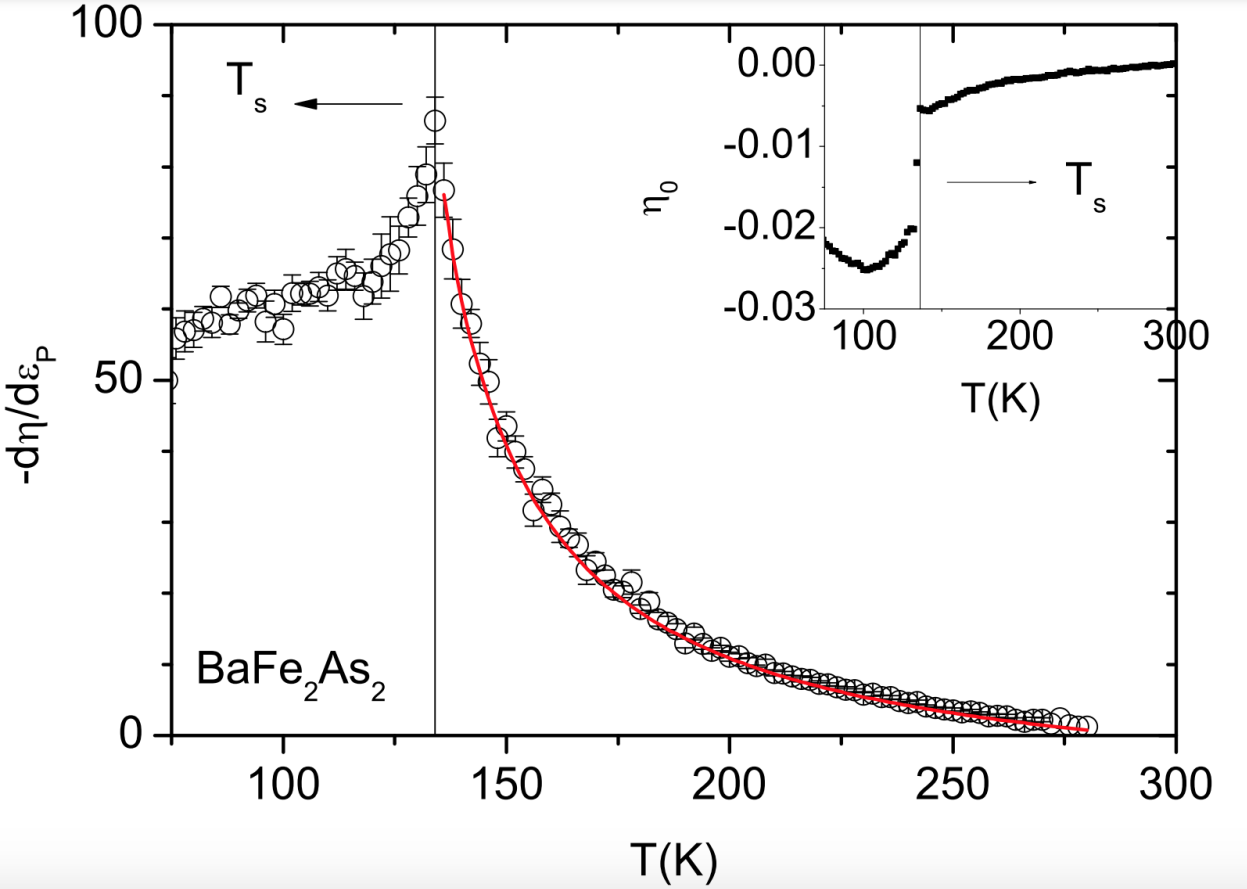

Figure 3.1: Reproduced from [5]. A measurement of the elastosusceptibility of the resistance anisotropy which [5] argue is proportional to the elastosusceptibility of the order parameter. The presence of a divergence in the susceptibility is interpreted as evidence for an electronic component of the order parameter for the nematic transition.

for superconductivity generated by fluctuations of the nematic order parameter but that is a contentious point and under intense debate in the literature.

3.3.3 Sr_2RuO_4

In Sr_2RuO_4, the effects of anisotropic strain on C_4 symmetric superconducting phased are spectacular [42, 43].

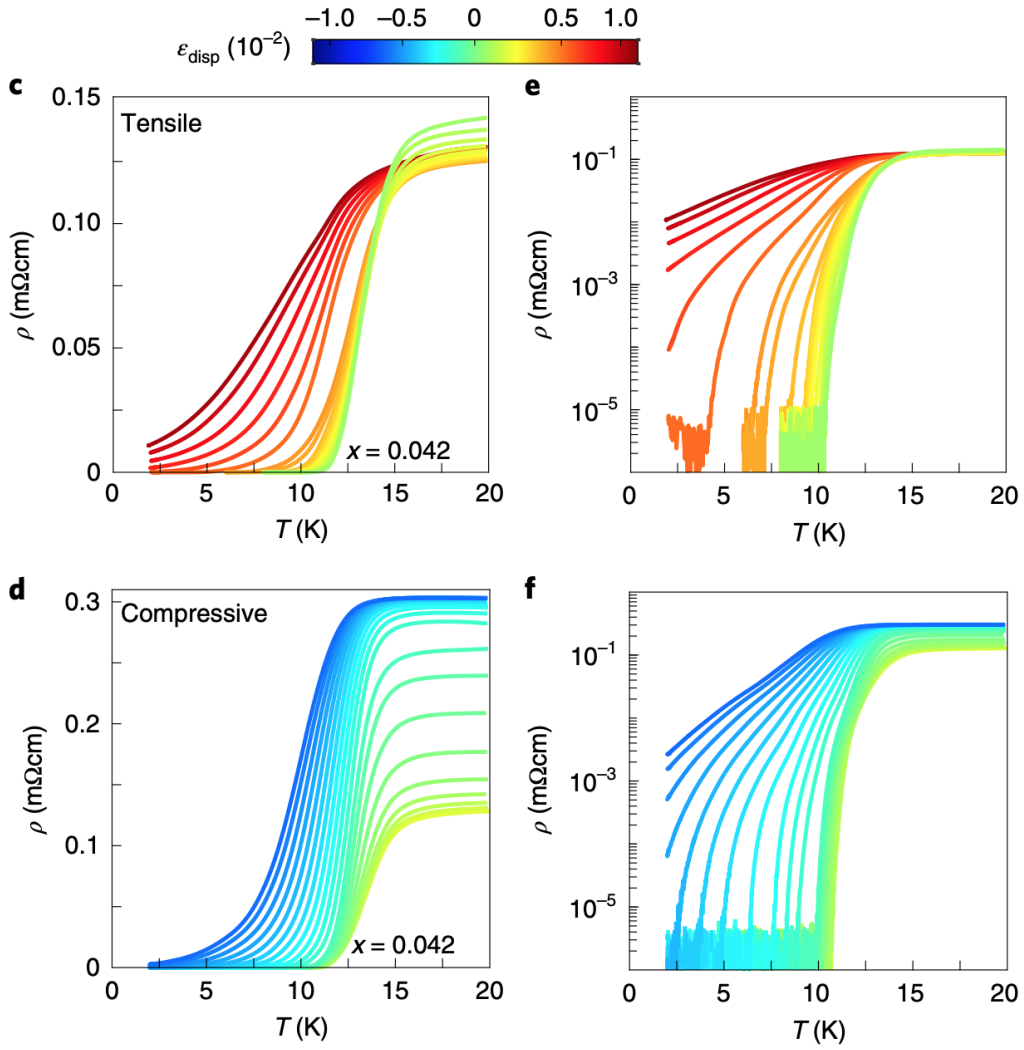

Figure 3.2: Reproduced from [39]. This work shows that application of uniaxial strain to samples of $Ba(Fe_{1-x}Co_x)_2As_2$
can fully tune the superconducting state in this class of compounds, establishing anisotropic strain as a tuning parameter for the phase diagram of the pnictide superconductors.

Sr_2RuO_4 is an archetypal unconventional superconductor. Originally discovered in the 1990s [44] when the excitement about the compound was centered on the existence of a perovskite superconductor that did not contain copper, research on superconductivity in this material has a long and fascinating history. It was suggested early on that the superconducting order parameter in this material may well be of odd parity which would open the door to realizing exotic and potentially technologically relevant phenomena such as topological superconductivity [45, 46]. In recent years aspect of the original proposals have come into question due to contradictory evidence from strain experiments [47].

It had been known for a while that the superconducting transition temperature of Sr_2RuO_4

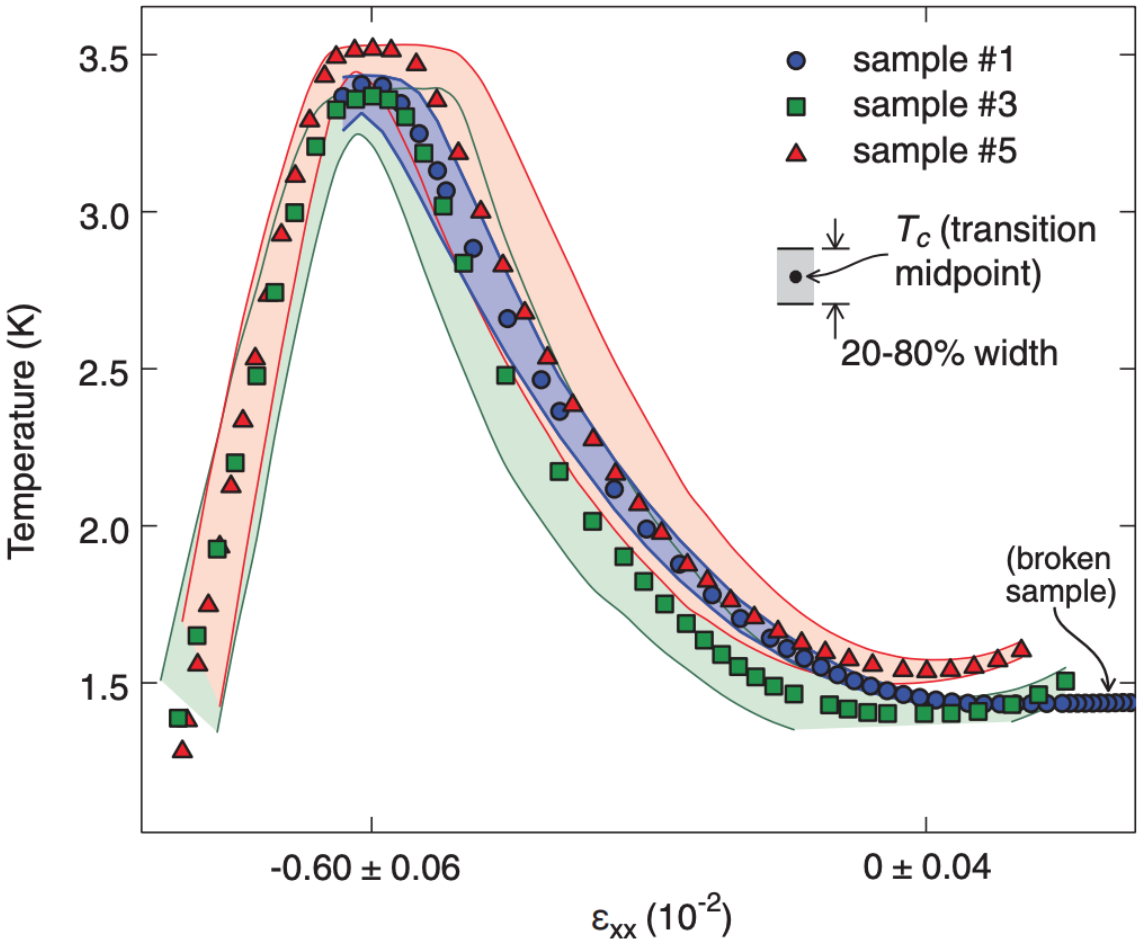

Figure 3.3: [39] showed that application of uniaxial strain to samples of $Ba(Fe_{1-x}Co_x)_2As_2$

is sensitive to strain ([48]). In [42] and [43] it was shown that the superconducting transition temperature may in fact be as much as doubled through the action of uniaxial strain on bulk crystals of the material. Modelling of the coupling of uniaxial strain to the order parameter of the transition results in some striking predictions for the strain dependence of response functions such as the T_c and the heat capacity. A number of those predictions, such as the presence of a peak around zero strain [42] and a split transition visible in temperature dependent heat capacity [49]. The overall contributions of the strain measurements to Sr_2RuO_4 research has been highly significant, throwing doubt on a long-held consensus view of the gap symmetry in this material and igniting a flurry of activity to clarify the situation.

3.4 Charge order in cuprates as inspiration for current work

One of the major discoveries in the field of high-temperature superconductors in the last decade was the finding that heretofore unobserved charge ordering exists in swaths of the phase diagram of these fascinating materials [50].

3.4.1 Phase diagram of cuprate superconductors

We do not seek here to give an overview of the phenomenology of the cuprate superconductors. It is a huge field with a long history. The goal of this section is to give a somewhat high level overview of the aspects of those materials, which continue to be an epicenter of condensed matter research, that are relevant to the physics we address in our study of 2H-$NbSe_2$.

At a phenomenological level the physics of the cuprate superconductors tends to be discussed in terms of a temperature-doping phase diagram. One begins with a parent phase which is an antiferromagnetic Mott insulator and comprehensive characterized from both experimental and theoretical standpoints [51, 52]. One then considers doping this insulator and the phases that arise. We will focus on hole doping, as does the majority of the literature, because doping with holes gives rise to the incredibly high transition temperatures which

fundamentally are the point of interest [53]. As function of doping a superconducting dome appears beginning at a minimum hole doping $p_{min} < 0.1$, reaching a maximum transition temperature $T_c \approx 100K$ (depending on the particularities of the compound one works with). Finally the superconductivity is suppressed at a maximum hole doping $p_{max} > 0.2$.

We do not wish to discuss the theories of cuprate superconductivity here in any depth at all as this is not our expertise or the goal of this work. We will instead discuss the

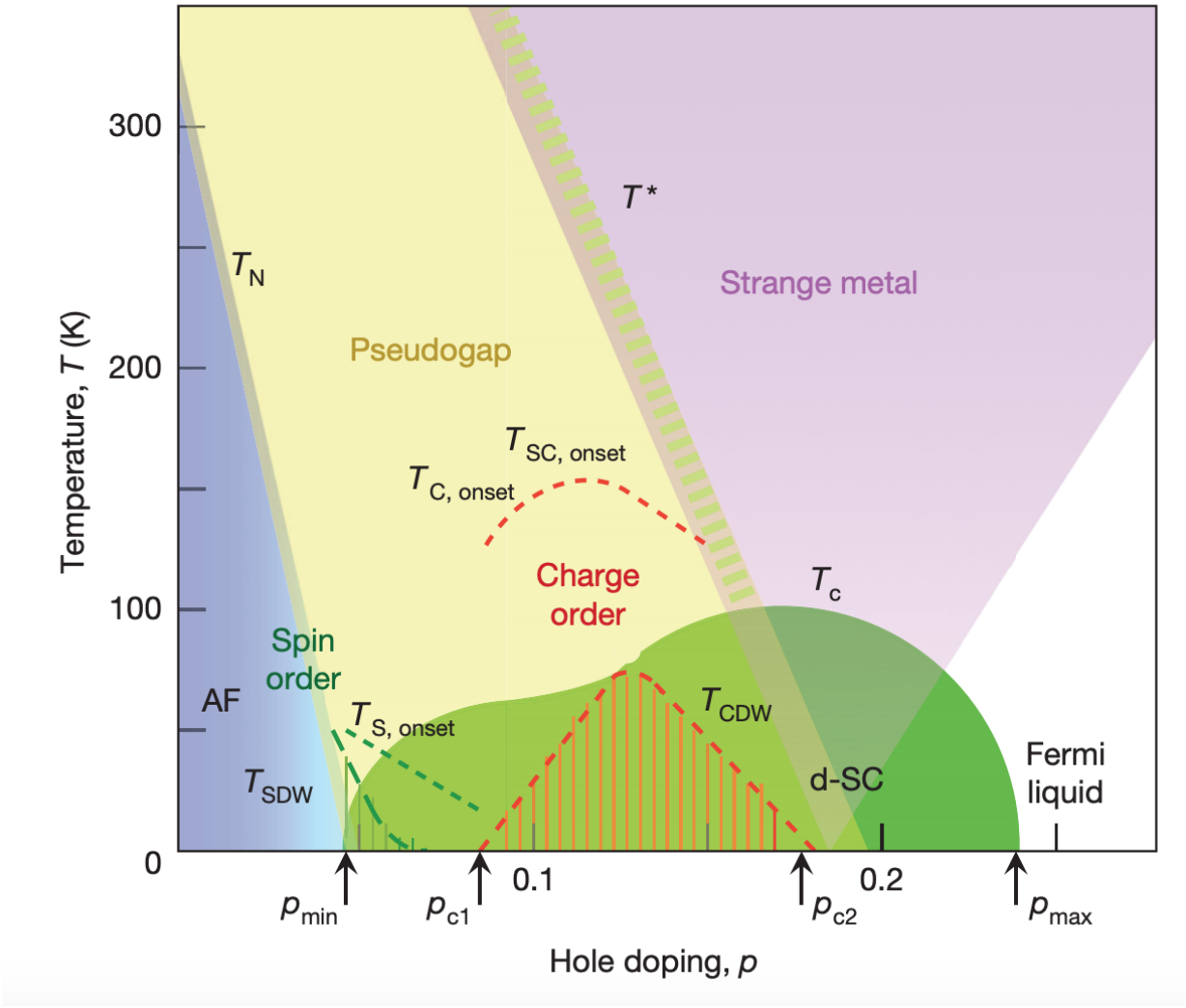

Figure 3.4: Reproduced from [37]. A schematic phase diagram of the cuprate superconductors, indicating the presence for a gamut of (sometimes overlapping) phases, from the dome-shaped superconducting region through the pseudogap phase and the charge ordered regions.

thinking behind theories of this phase diagram in very broad terms because it is relevant to our study. Crudely speaking, one way to attempt an understanding of the cuprate phase diagram is to take a vertical cut in the $p-T$ plane: in other words, to consider a system at a fixed doping. One can then plainly ask: what is the high temperature phase from which the superconductivity condenses? Among the phenomena present in those high-temperature

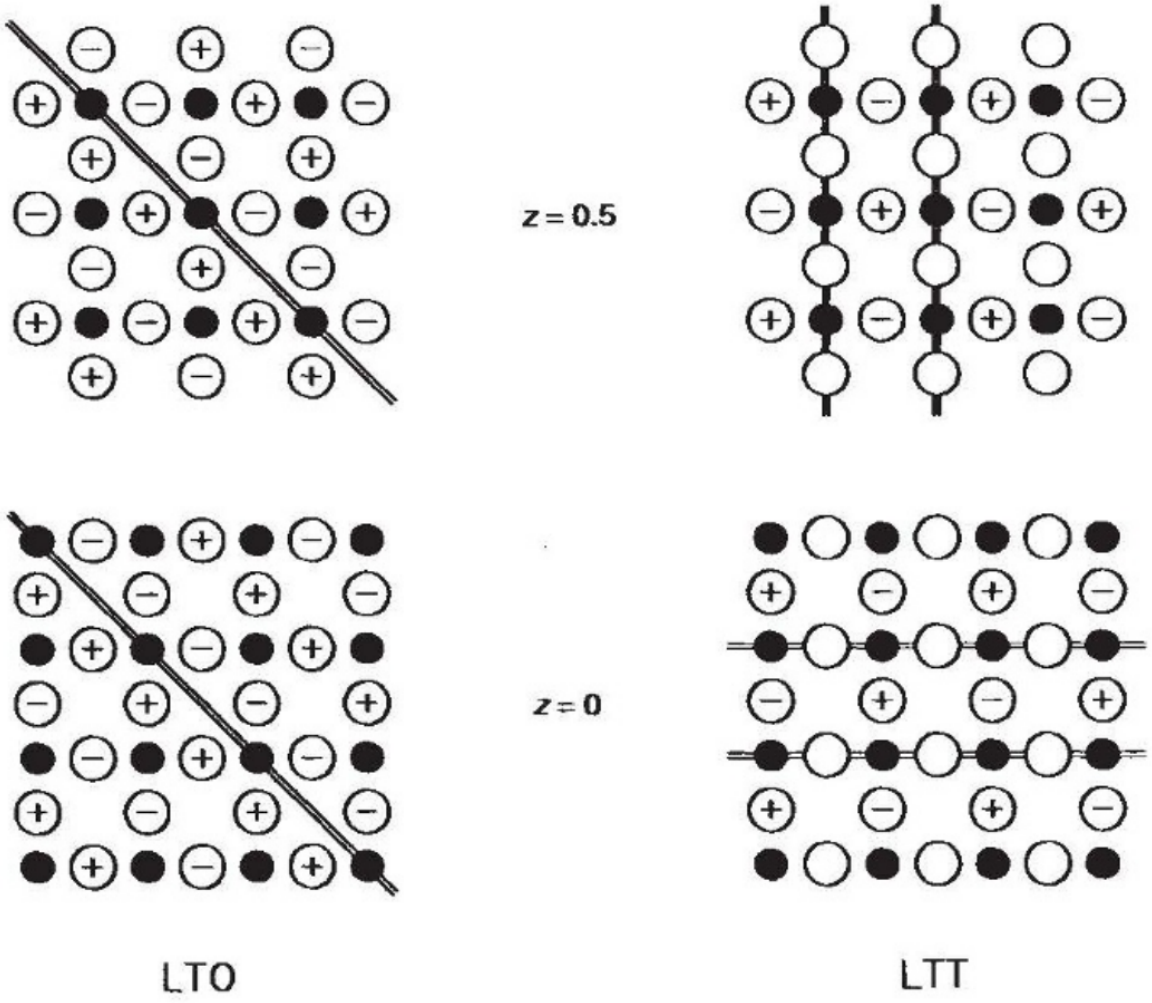

Figure 3.5: Reproduced from [26]. Displacement patterns within the two $Cu0_2$ layers of a unit cell for two structures occurring in $La_{2-x}Ba_xCu0_4$, low-temperature orthorhombic (LTO) and low-temperature tetragonal (LTT). Atoms of oxygen (copper) are represented by open(solid) circles, and their displacements out of plane are indicated by +/-. The doubled lines indicate the tilt axes and it is local rotations about those axis that generate out of plane displacements of the oxygen atoms. z is the height along the c-axis in lattice units. The tilt axes rotate by 90^0 from $z = 0$ to $z = 0.5$ in the LTT structure.

phases is charge order and therein is the intellectual connection between the cuprates and the much simpler phenomenology of 2H-$NbSe_2$.

3.4.2 Charge order in cuprates and the connection to 2H-$NbSe_2$

Charge order was originally discovered in some cuprate compounds in the mid-1990s [26]. A more recent discovery is its ubiquity in the classes of cuprate compounds where previously it had not been known to exist, suggesting that it could play a more generic role in the phenomenology of these materials than previously thought. While this subject remains under heated debate, these discussions *have* given rise to a debate about the interplay of unidirectional (stripe-like, "1Q") and bidirectional ("2Q") charge ordering geometries in these materials [54, 55, 56, 57].

2H-$NbSe_2$ is a material which both superconducts and undergoes and charge density wave distortion. It has been known since [58] that under a moderate amount of uniaxial strain it is possible to tune a triangular ("3Q") charge density wave in this material through a transition to a unidirectional ("1Q") stripe-like density wave. Under a continuously tunable strain, it is then possible to investigate the impact that this transition has on superconductivity in this compound. In brief, that is the goal of the current part of this thesis.

While we do not claim that the strain effect on superconductivity in 2H-$NbSe_2$ is analogous to the corresponding effect in cuprates, we do hope to provide an example of a scenario in which charge order and superconductivity interplay. Indeed, a recent inelastic X-ray scattering study on $YBa_2Cu_3O_{6.67}$ showed that a novel charge-ordered phase forms when samples are put under large uniaxial pressures [59], and authors of that study suggest that in that material superconductivity and charge order compete.

3.5 Phenomenology of 2H-$NbSe_2$

The effect of anisotropic strain on the charge ordered superconductor 2H-$NbSe_2$ is the subject of this letter.

3.5.1 Structure

2H-$NbSe_2$ is a member of the transition metal dichalcogenide family of compounds. First studied decades ago [61], interest in these materials has been sustained by the wealth of phenomena which they exhibit and, more recently, their layered nature. Under the banner of "Van der Waals" materials the transition metal dichalcogenides have received a slew of attention due to researchers' ability to isolate atomically thin, truly two dimensional samples [62, 63] whose properties are exciting and novel. Its structure is shown in Fig. 3.6.

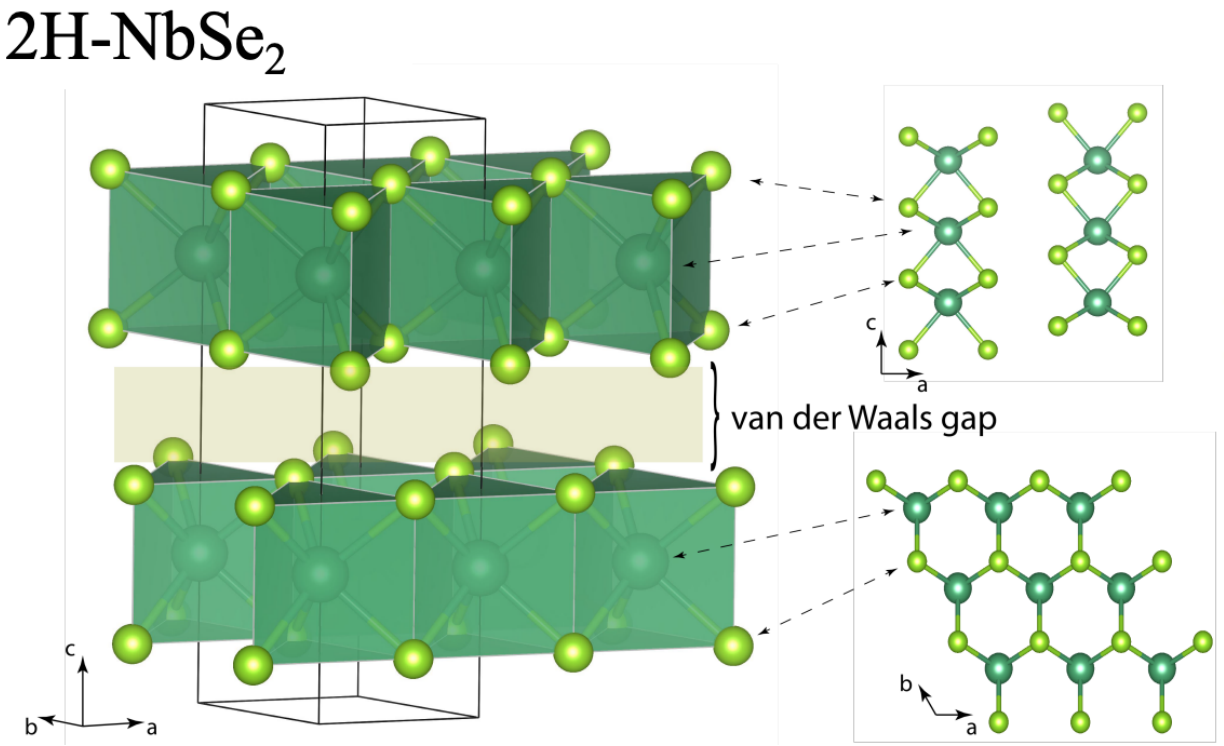

Figure 3.6: Reproduced from [60]. Crystal structure of 2H-$NbSe_2$. 2H-$NbSe_2$ is a quasi-two dimensional material, with planar layers stacked together along an axis (c-axis) into a three-dimesional structure held together by Van Der Waals forces. The inset on the right shows projections of the crystal structure onto the ac and ab planes to help the reader may visualize how the atoms are arranged.

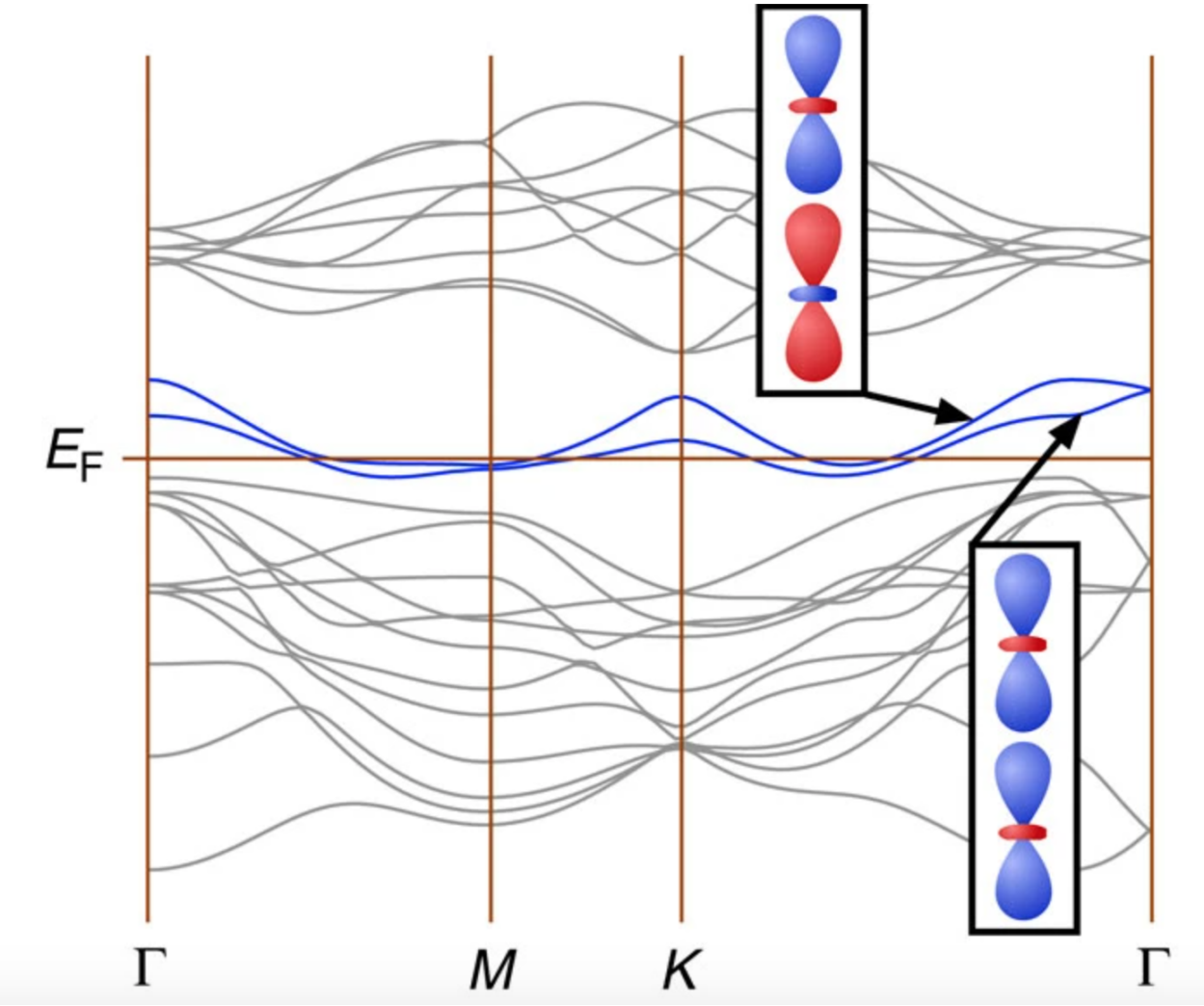

3.5.2 Electronic structure

Figure 3.7: Reproduced from [64]. The band structure of 2H-$NbSe_2$ obtained through a tight-binding fit to both Angle-Resolved Photoemission Spectroscopy (ARPES) data and density functional theory (DFT) band structure calculations. The flat horizontal line labelled E_F is the Fermi energy. The two thick lines, consisting of the bonding and antibonding combinations of Niobium's $d_{3z^2-r^2}$ orbitals, are the electronically active bands.

Electronically transition metal dichalcogenides fall into metallic, semi-metallic and insulating categories. 2H-$NbSe_2$ is a member of the metallic group. Its bandstructure is shown in Fig. 3.5.2. The electronically active bands, indicated by thick lines in panel a of 3.5.2,

originate from the bonding and antibonding combinations of Niobium's $d_{3z^2-r^2}$ orbitals. The Fermi surface which results is shown in Fig. 3.8.

3.5.3 Superconductivity

$NbSe_2$ is a BCS, two-gap *s*-wave superconductor with $T_{sc} = 7.2\,\mathrm{K}$. The superconductivity in this material is multiband in that more than one band takes part in the superconducting pairing. However, there is overwhelming evidence for s-wave pairing and existing works have not identified deviations from this scenario (see Fig. 3.9).

3.5.4 Charge order

A charge density wave distortion onsets below $T_{cdw} = 33.7\,\mathrm{K}$ [66, 67]. This ('3Q') charge ordered phase possesses C_3 rotational symmetry and its period is $\sim 3 \times 3$ lattice constants. The origin of the distortion seems to be strong electron-phonon coupling rather than by a

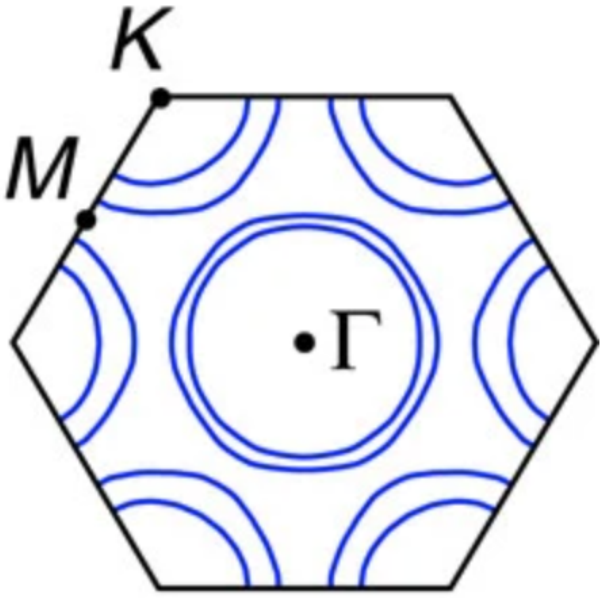

Figure 3.8: Reproduced from [64]. The Fermi surface of 2H-$NbSe_2$ obtained through a tight-binding fit to both Angle-Resolved Photoemission Spectroscopy (ARPES) data and density functional theory (DFT) band structure calculations.

Fermi surface instability [68, 69, 70, 71, 72, 64].

3.5.5 Effect of anisotropic strain on charge order

Two recent scanning tunnelling microscopy studies [58, 73] reported evidence of a novel, unidirectional charge ordering in samples where strain is present.

3.6 Description of measurements

Electrical transport measurements were performed on high-quality single crystals of 2H-$NbSe_2$. Uniaxial strain was applied using a piezoelectric strain application device as described in detail in Chapter 2. We note that the effect of differential thermal contraction between components of the device (see Chapter 2 for details) gives a correction to applied strain (estimated to be about 0.08% tension at superconducting temperatures), but this correction is approximately temperature independent in the range of our measurement (below 85 K). 2H-$NbSe_2$ crystals were mounted with the c-axis perpendicular to the direction of strain

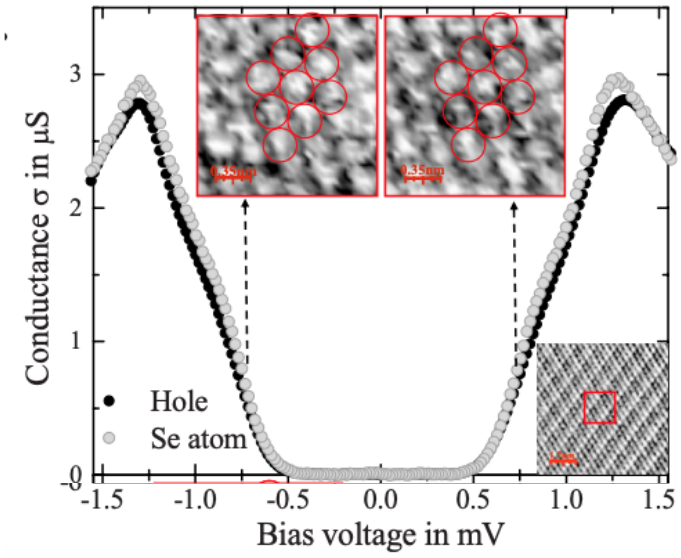

Figure 3.9: Reproduced from [65]. The plot shows a conductance curve $\sigma(V)$ taken with a Scanning Tunnelling Microscope tip on a sample of 2H-$NbSe_2$ below the superconducting transition temperature T_c = 7.2K. The shape of this tunnelling spectrum is consistent with an s-wave pairing scenario.

application. Longitudinal resistivity of the strained crystal was measured in the standard four-probe geometry, with R_{xx} measured across the strained region of the crystal (see Fig. 1a inset). Hall resistivities were extracted through antisymmetrization of magnetoresistivity

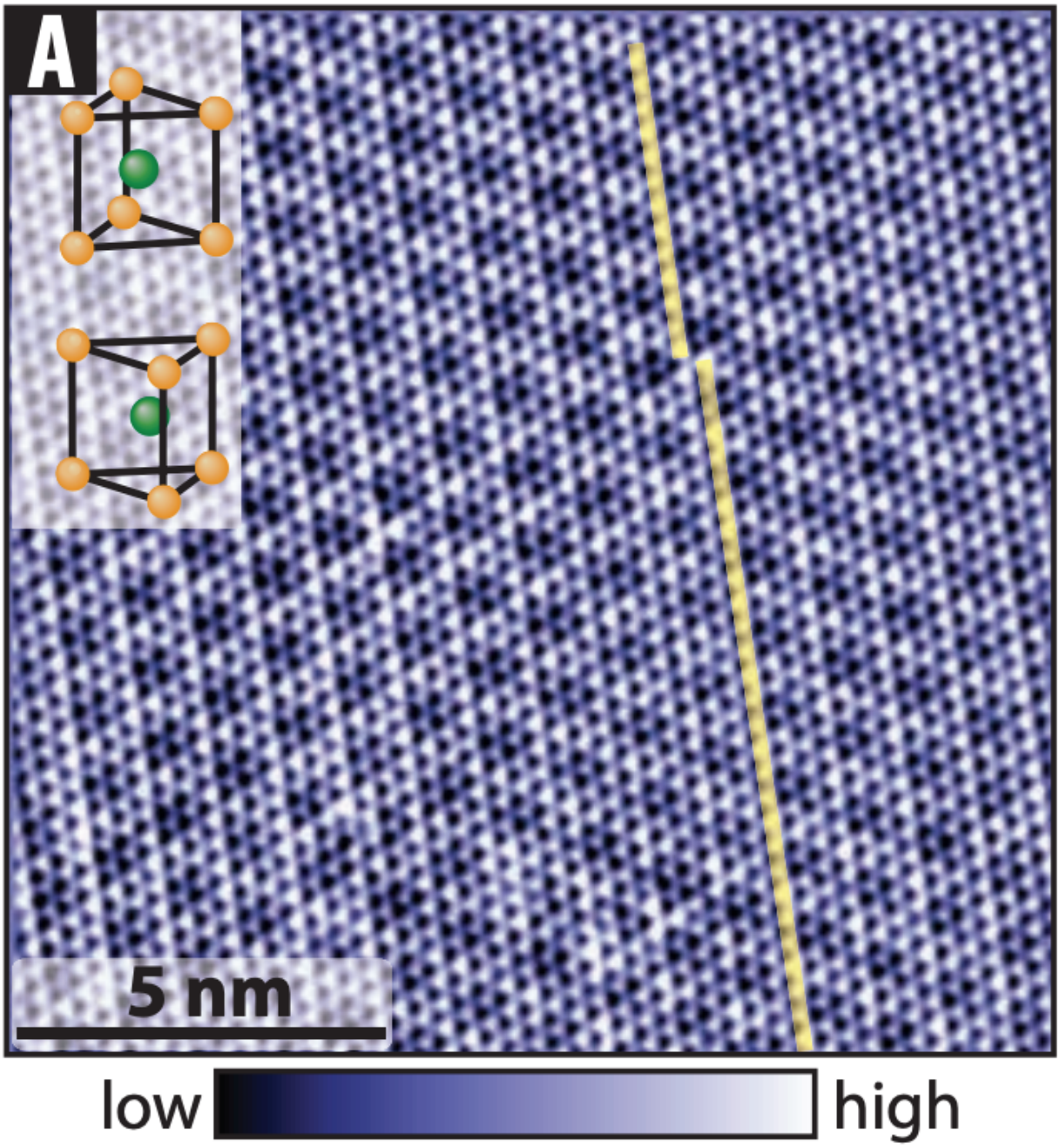

Figure 3.10: An atomically resolved scanning tunnelling microscopy image of the triangular, 3 unit cell periodic charge order in NbSe2 at low temperature ($< T_{CDW}$) under ambient conditions. [58]

measured for the two out-of-plane field directions. A representative resistivity curve for our 2H-$NbSe_2$ samples is shown in redTODO: add this Fig. 1c. Clearly observable are an anomaly around $T_{cdw} = 33.7\,\mathrm{K}$ and a sharp superconducting transition at $T_{sc} = 7.2\,\mathrm{K}$.

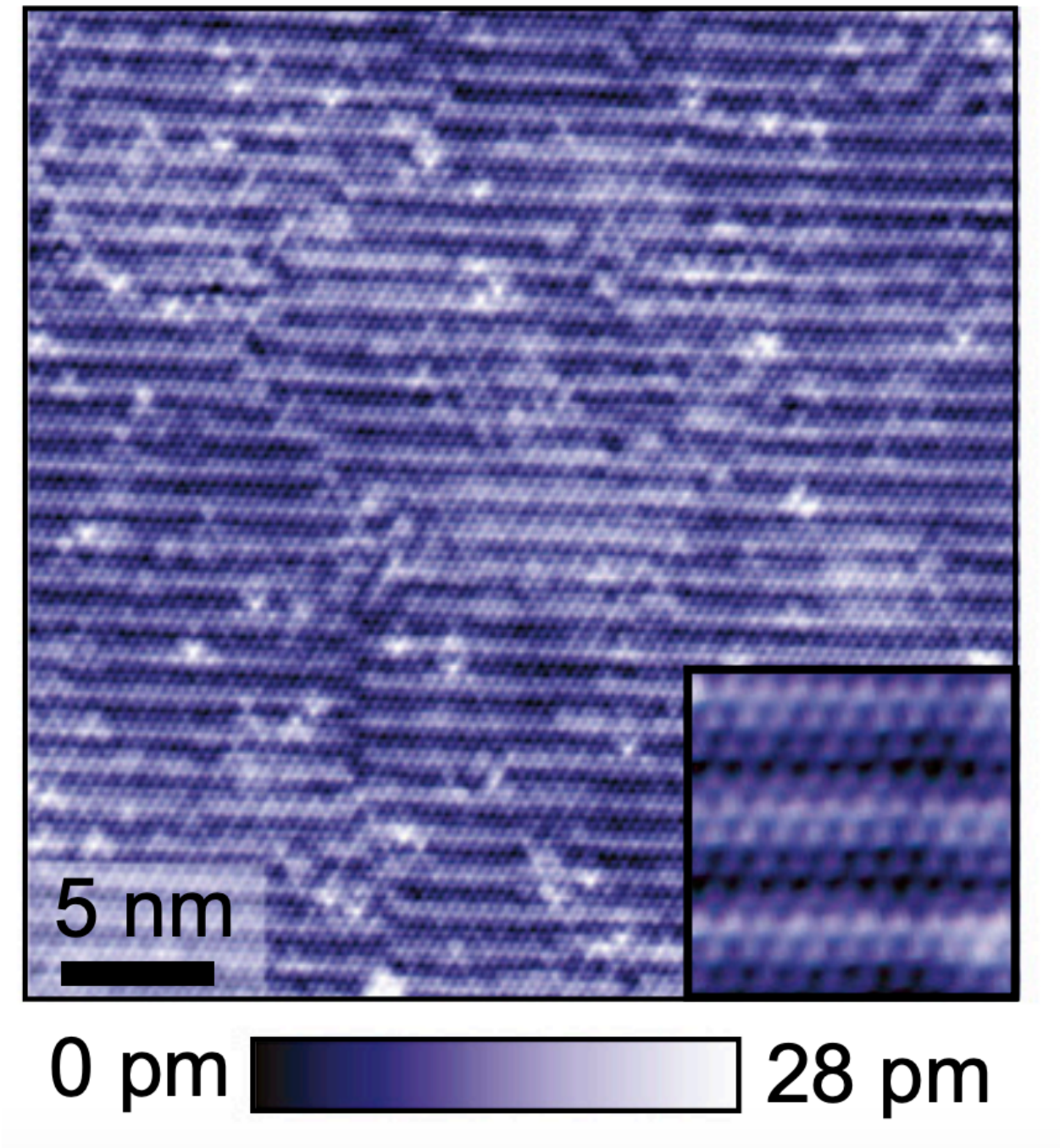

Figure 3.11: Reproduced from [58]. An atomically resolved scanning tunnelling microscopy image of the triangular, 3 unit cell periodic charge order in $NbSe_2$ at low temperature ($< T_{CDW}$) under ambient conditions.

3.7 Thermal phase diagram of 2H-$NbSe_2$ as function of anisotropic strain

3.7.1 Superconductivity

Figures

3.8 Charge order

A natural follow-up question is how T_{cdw} depends on uniaxial strain. Previous works have observed a small signature of the charge density wave transition in the longitudinal resistivity at T_{cdw} in the cleanest samples. This feature is highly dependent on the disorder

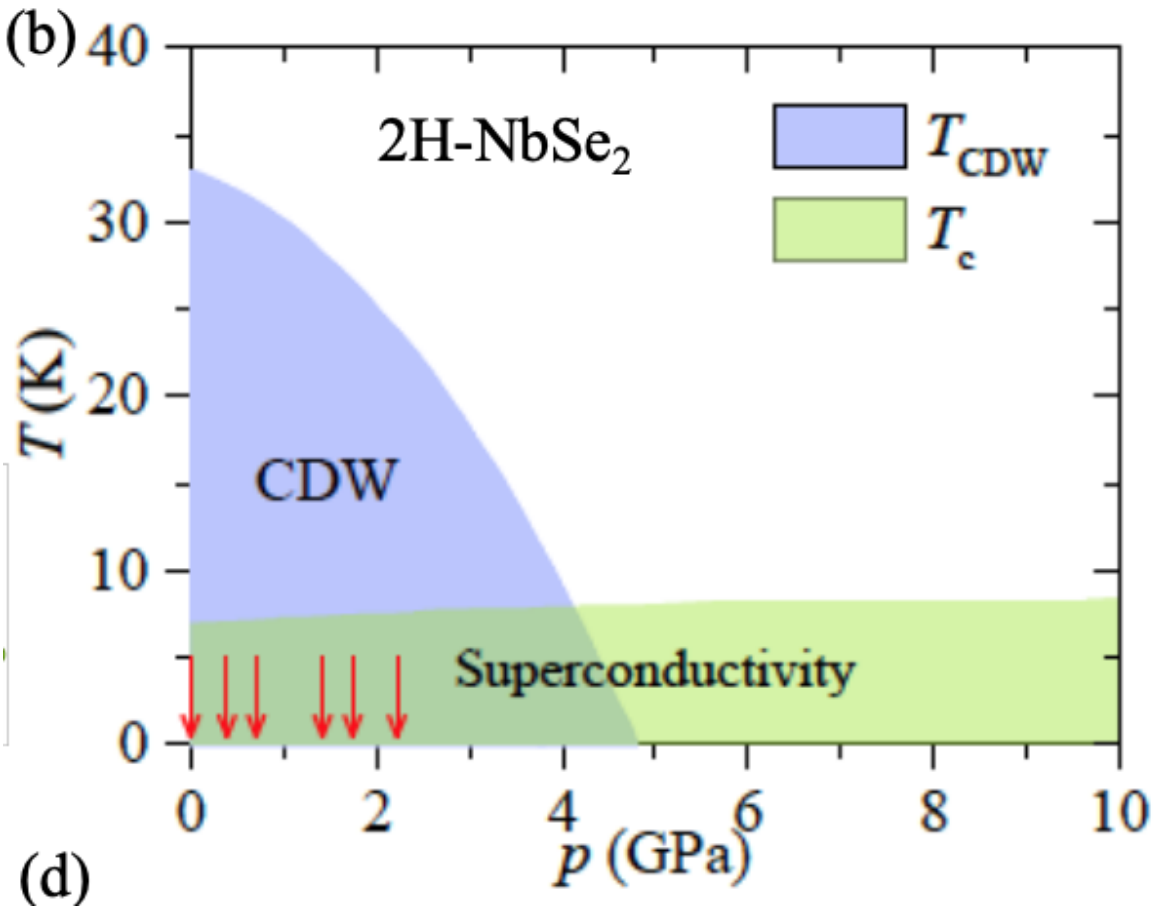

Figure 3.12: Reproduced from [60]. As function of pressure the charge ordering temperature of 2H-$NbSe_2$ is suppressed while the superconducting transition temperature is mildly enhanced.

level of the samples, since in the presence of disorder the CDW transition is significantly smeared out [75]. In our samples, this anomaly in the longitudinal resistivity is extremely weak. We were not able to reliably measure changes in this feature as a function of strain. An alternative signature in transport is provided by the Hall coefficient, which has been shown to have a sign change at a temperature a little below the CDW transition. Figure 3.16 shows the temperature dependence of the Hall resistance for sample A, recorded at zero strain and under the applied tensile strain of 0.4%. We identify T_{cdw} with the onset temperature of a downturn in the Hall resistance, which falls around $T = 35\,\mathrm{K}$. Our measurement shows

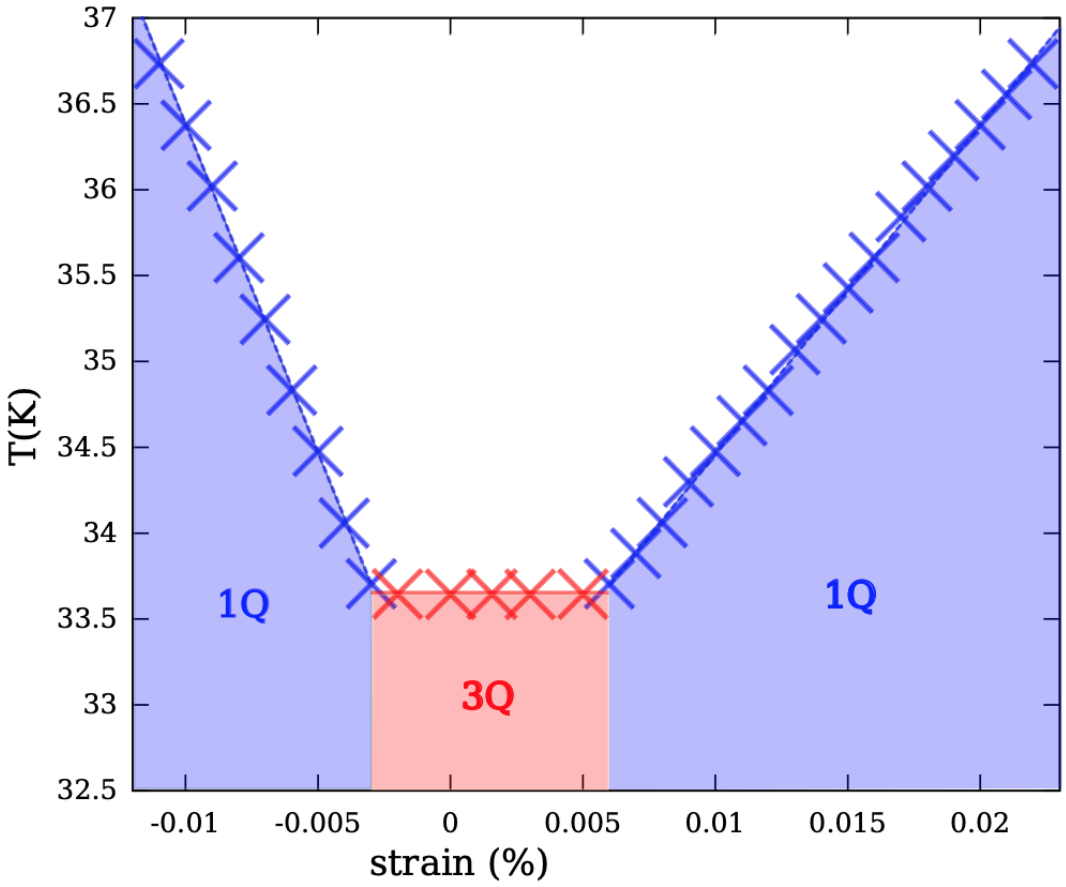

Figure 3.13: Reproduced from [74]. A minimum critical uniaxial strain is required to trigger the transition from '3Q' triangular charge ordering geometry to '1Q' unidirectional ordering. The transition temperature increases moderately over a range of uniaxial strain ±1% with the rate of increase being approxmiately twice as large for compressive strain as for tensile strain.

that the CDW transition temperature does not shift within this strain interval by more than the sensitivity of this measurement, estimated to be $\Delta T \sim 2\,\mathrm{K}$. We note that for the same change in strain, there is a significant drop in T_{sc} (see inset of Fig. 3.16). Consequently, the effect of uniaxial, ab-plane strain on T_{cdw} in this material is weak compared to the effect on T_{sc}. Precise determination of how strain affects T_{cdw} will require combining uniaxial strain with a direct probe of charge order, such as high-resolution X-ray diffraction or Raman spectroscopy.

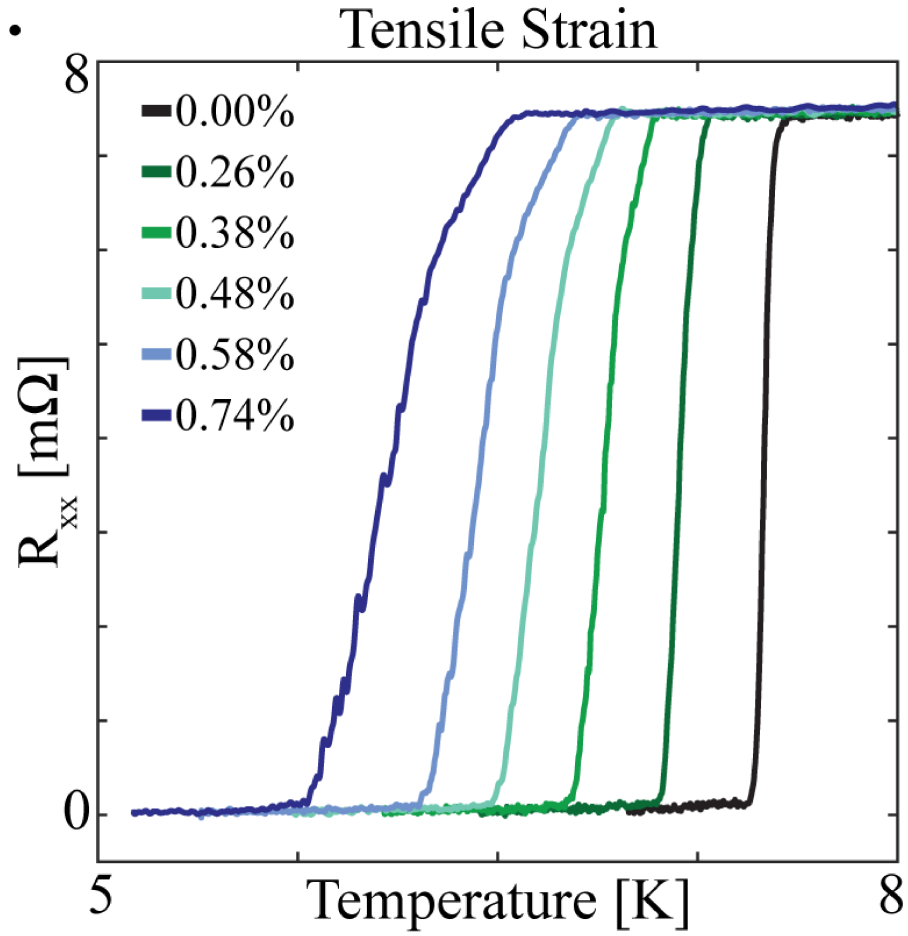

Figure 3.14: Transport properties of 2H-$NbSe_2$ in the 5-8K temperature range for a sample placed under a number of applied tensile strains. We notice a downward shift in the superconducting transition temperature as well as a mild (<1K) broadening of the transition profile.

3.9 Phase diagram

The results are summarized in Fig. 3.17 in the form of a phase diagram showing the dependence of T_{sc} on the tensile and compressive strains. The results are as follows: 1) T_{sc} is insensitive to strain within a region centered around zero strain; 2) beyond this region, T_{sc} is significantly suppressed with both tension and compression; 3) compressive strain has a stronger effect on T_{sc} than tensile strain, by about a factor of two. We contrast these results of measurements as function of uniaxial strain with the hydrostatic pressure dependence of T_{sc}. We have considered the possibility that small strains are not properly transmitted to the

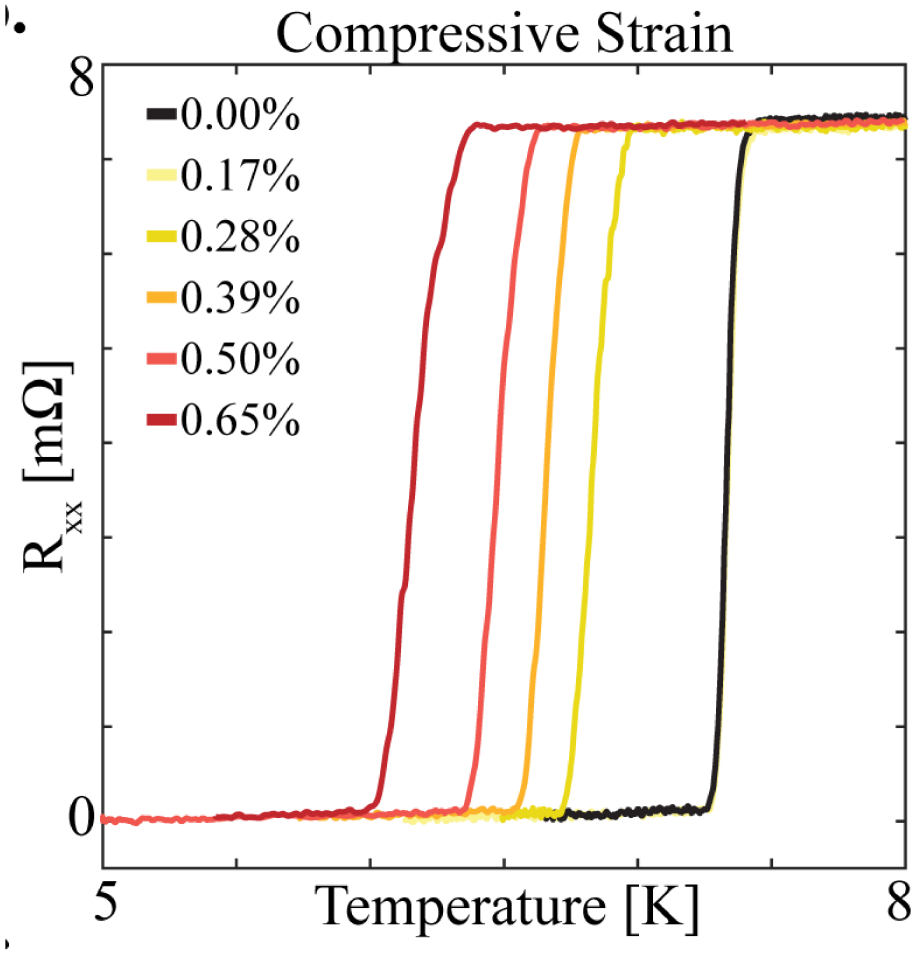

Figure 3.15: Transport properties of 2H-$NbSe_2$ in the 5-8K temperature range for a sample placed under a number of applied compressive strains. We notice a downward shift in the superconducting transition temperature as well as a mild (<1K) broadening of the transition profile.

sample. By measuring the elastoresistance of well-known iron pnictides [5] at small strains, we have confirmed that strains down to <0.01% are transmitted well to the sample.

3.9.1 Anisotropic vs. hydrostatic pressure

In Fig. 3.18 we summarize the hydrostatic pressure data based on the previously known pressure dependence of T_{sc} [76, 77]. Interestingly, the sign of the effect is opposite for uniaxial and hydrostatic pressure: hydrostatic pressure monotonically increases T_{sc} whereas the strain dependence of T_{sc} contains a transition between a region of no dependence to a region where T_{sc} is significantly affected. The magnitude of the uniaxial strain effect is much larger (1.8 K at 0.6%) than the corresponding change under hydrostatic pressure (0.6 K).

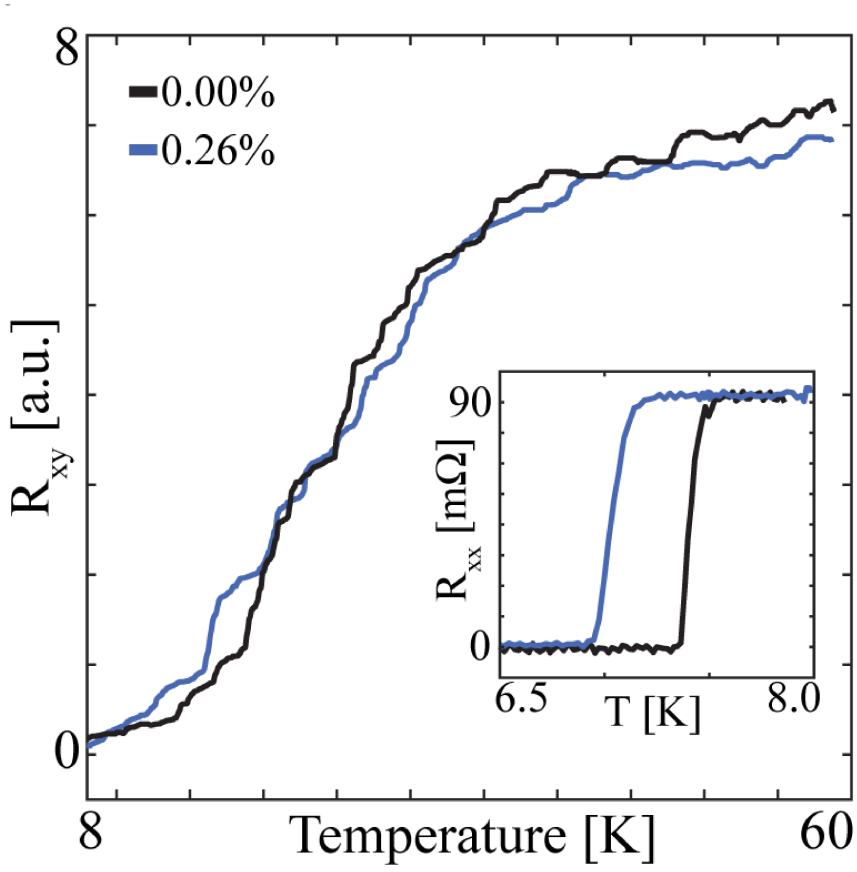

Figure 3.16: The resistivity profile of $NbSe_2$ in the temperature range around T_{CDW} for a sample with and without applied strain. We note the absence of a large shift in the charge ordering transition temperature. A small shift in T_{CDW} is consistent with these data.

3.10 Theoretical picture

We hypothesize that that T_c is dictated by T_{CDW}. In order to test the hypothesis we used the random phase approximation (RPA) to model the charge order as developing from an electron-phonon coupling dependent on both ingoing and outgoing electron momenta, and the orbital content of the electronic bands scattered between. This model has previously been shown to provide a consistent explanation of the full range of experimental results on

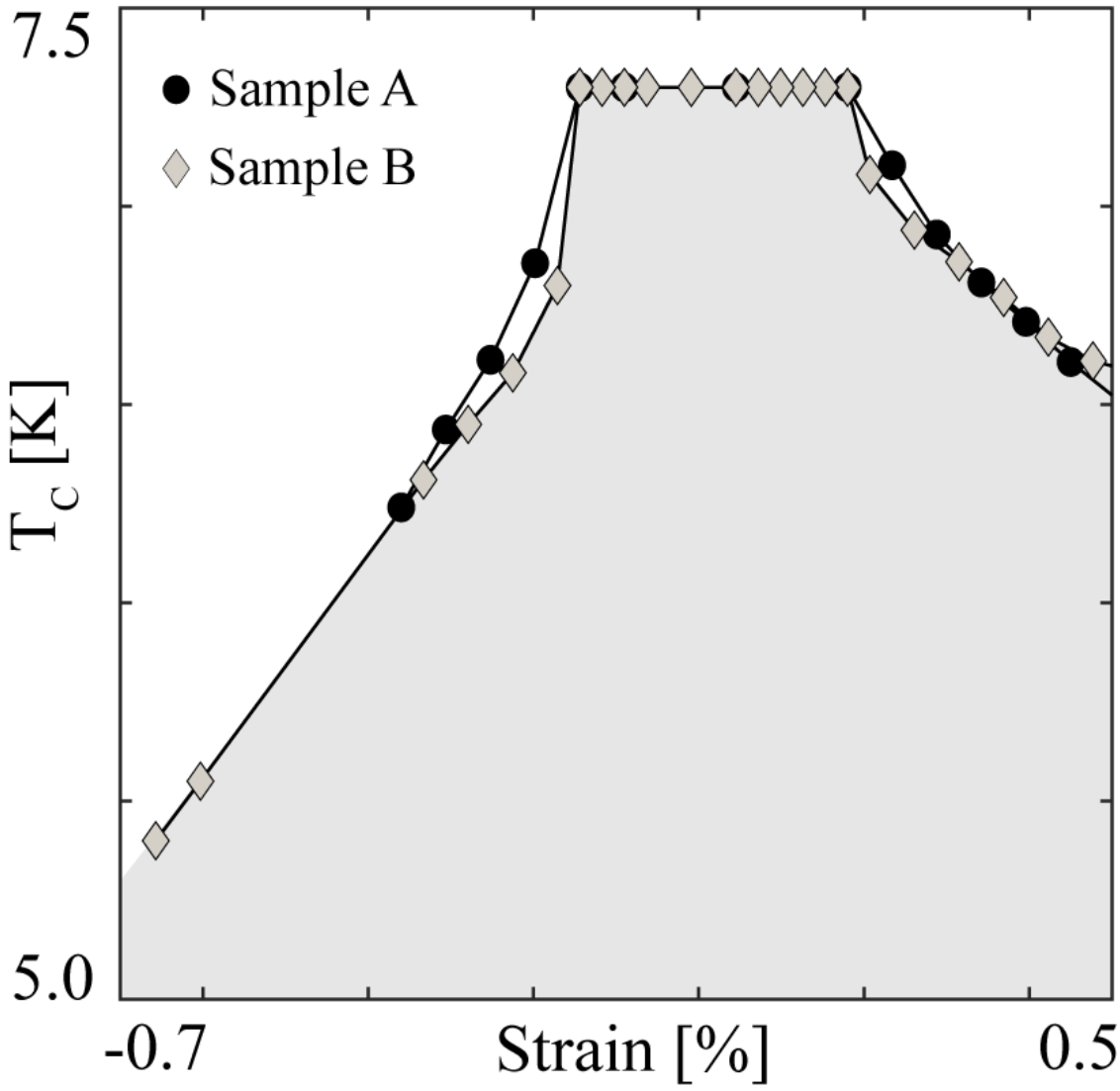

Figure 3.17: Strain dependence of superconducting T_{sc} for two different samples.

the charge order in the unstrained material [64, 78, 79], as well as being able to account for the charge ordering geometries in the strained system [73].

In the unstrained case, inelastic X-ray scattering has established that charge order develops through the softening of a longitudinal acoustic phonon at the CDW wavevector of $\approx 0.986 \cdot \frac{2}{3}\Gamma M$ [80, 81]. We introduce a uniaxial strain σ by increasing the phonon energy

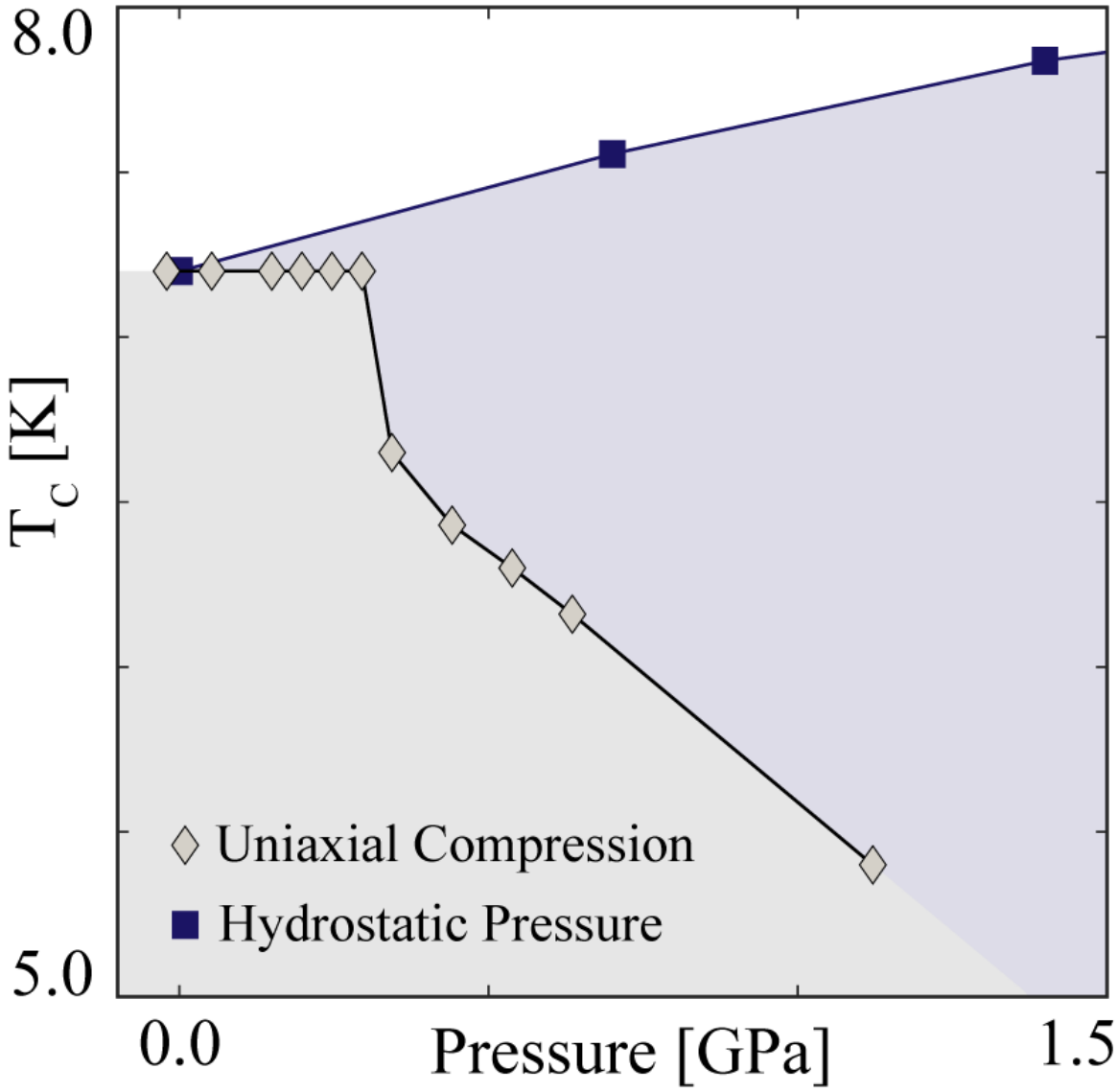

Figure 3.18: Comparison between hydrostatic and uniaxial pressure effects on superconducting T_{sc}.

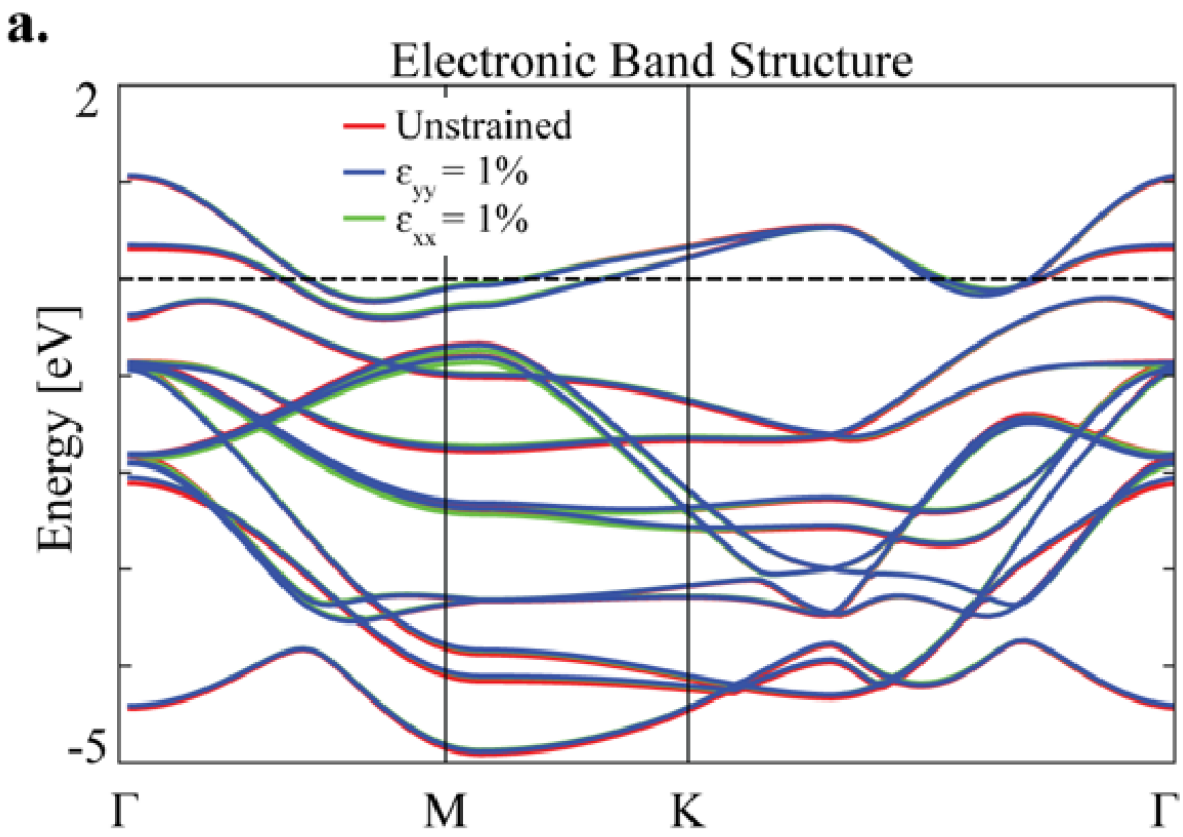

Figure 3.19: Electronic band structure computed from DFT for different uniaxial strains.

$\Omega \to (1+\sigma)\,\Omega$ along one of the ΓM directions, and decreasing by $\Omega \to (1-\sigma/2)\,\Omega$ in the two other directions. This decrease makes a minimal allowance for the Poisson's ratio of the material, assuming the unit cell volume is conserved under small strains.

We employ a Landau free energy expansion, truncated at quartic order in phonon displacements, to find the CDW geometry as a function of strain [79]). The resulting phase diagram is shown in Figure 3.13. For small strains a hexagonal 3Q CDW develops at 33.5 K. Above $\sigma = 10^{-4}$ (tensile) a striped 1Q geometry becomes stable, with an increasing transition temperature as a function of applied strain. Similarly, below -5×10^{-5} (compressive strain) the 1Q state again stabilises. The magnitude of the slope of the transition line $T_{CDW}\,(\sigma)$ is twice that of the tensile case, a direct result of the factor of two asymmetry introduced by the Poisson's ratio. The low values of critical strain are an artefact of the RPA; the predicted critical values of $|\sigma|$ increase to order 0.1% if fluctuations are taken into account [78, 79].

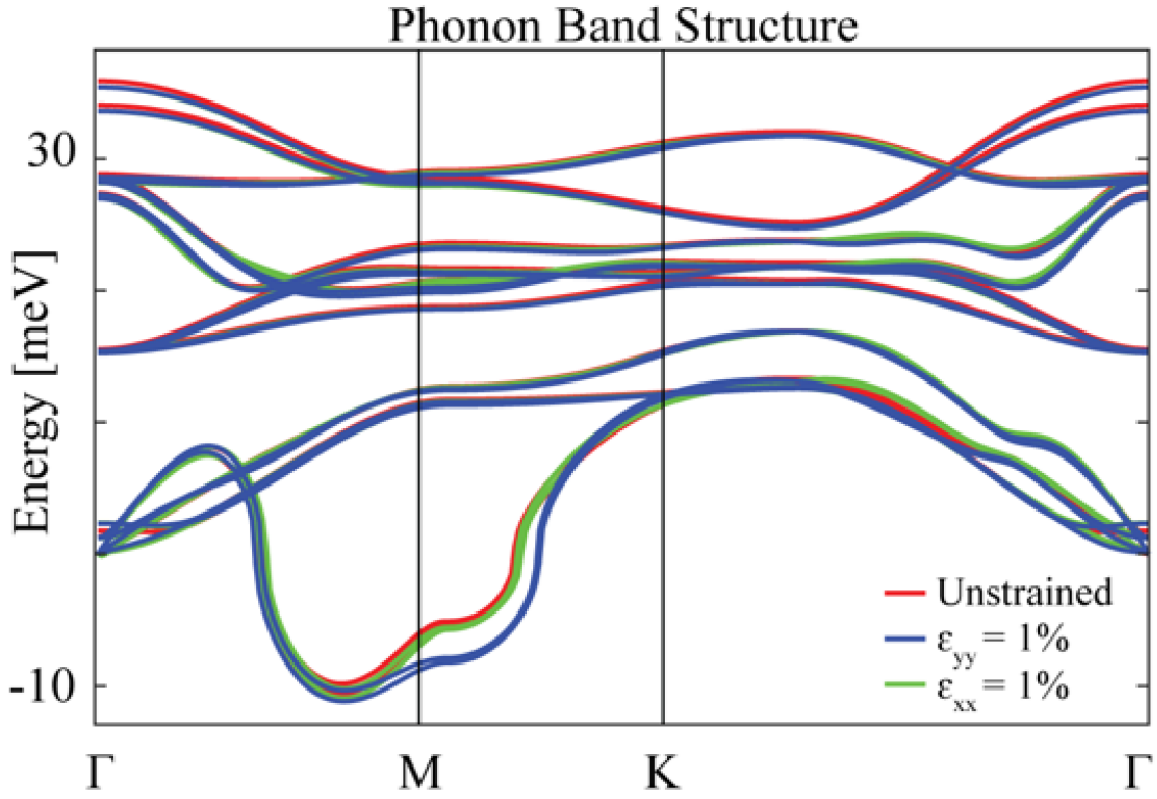

Figure 3.20: Phonon spectra computed from DFT for different uniaxial strains.

Comparing to our experimentally-measured superconductivity phase diagram in Figure 3.17 we see that the two show a remarkably similar structure. This can be explained by a direct competition between the charge order and superconductivity for control of the Fermi surface. In both cases, the transition temperature is constant for small strains, where the hexagonal 3Q geometry is favoured, and T_{CDW} is independent of strain. At larger strains T_{CDW} begins to increase as the uniaxial strain stabilises a 1Q CDW. The CDW gap Δ_{CDW} is expected to increase in proportion to T_{CDW} [2]. This leaves less of the Fermi surface available for superconductivity, decreasing Δ_{SC} when it develops, which then suppresses T_c proportionately. We predict the slope of $T_{CDW}(\sigma)$ at positive strains to be (minus) half that of negative strains; inspecting $T_c(\sigma)$ we find this relationship is again followed, with $T_c(\sigma < 0) \approx -1.9_c(\sigma > 0)$.

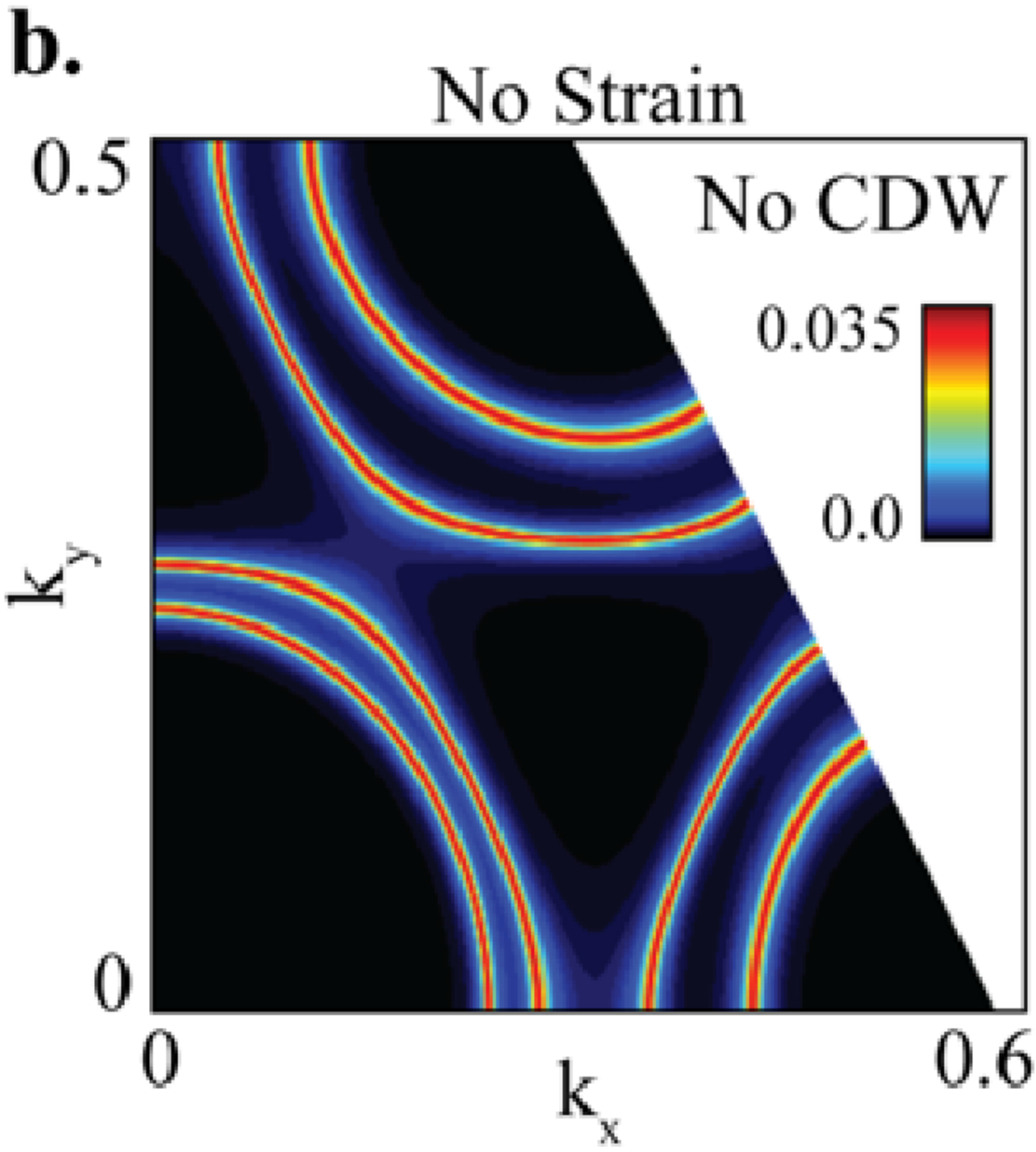

Figure 3.21: ARPES spectral density at the Fermi level for the unstrained and undistorted material.

To confirm the competition between the charge order and superconductivity we calculate the probability of occupation of states at each point $\mathbf{k}$ in the Brillouin zone at the Fermi energy E_F. This is given by the spectral function $A(E_F, \mathbf{k})$, and is proportional to the intensity predicted to be observed in angle-resolved photoemission spectroscopy (ARPES) [82]. Our

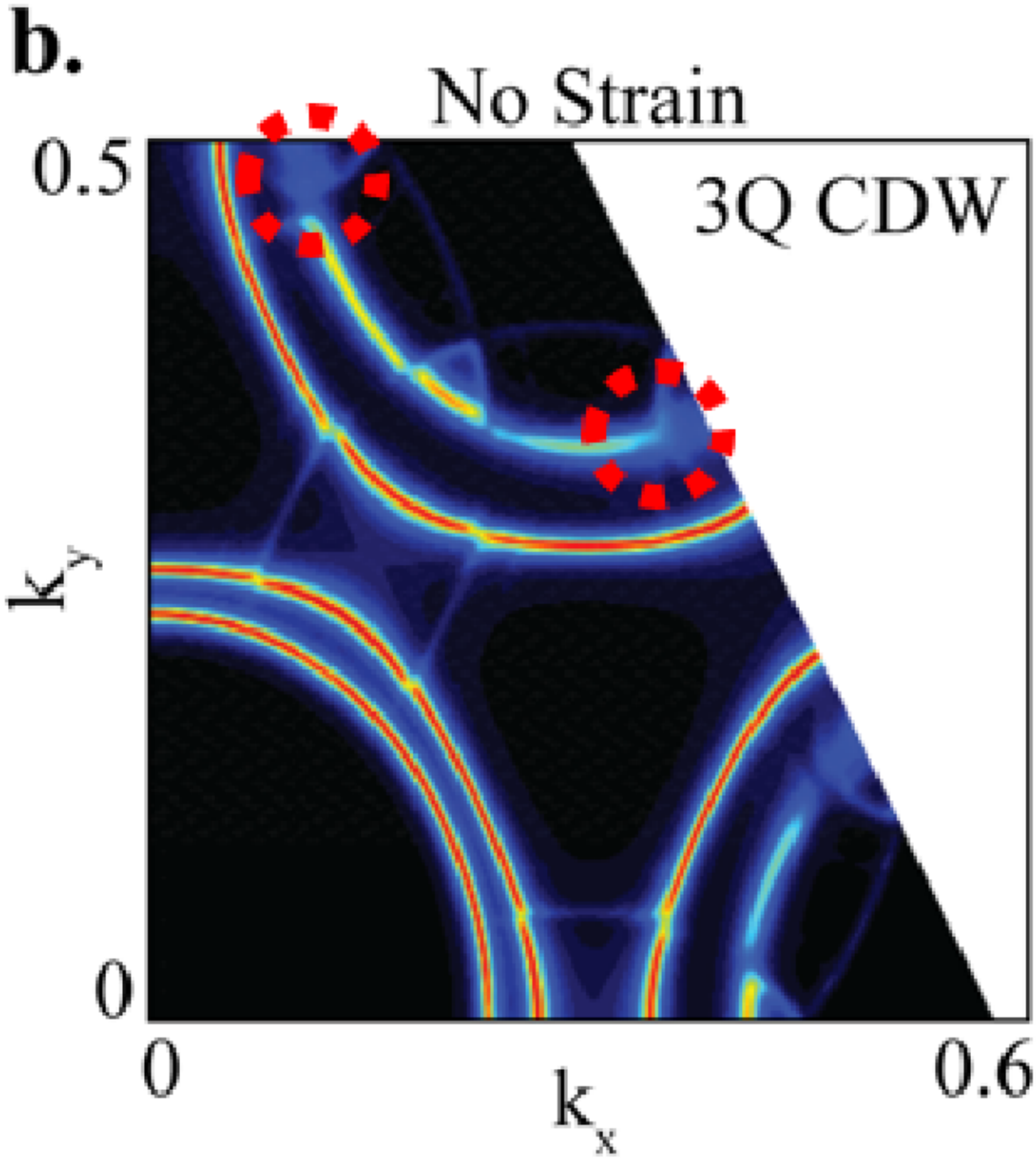

Figure 3.22: ARPES spectral density at the Fermi level for the unstrained and '3Q' distorted material. Regions where the spectral density is suppressed due to charge ordering are highlighted with red circles.

results are shown in Fig. 3.21, 3.22, 3.23 and 3.24 for four cases. In Fig. 3.21 we show the result for zero strain, with no CDW gap. As we used for our electronic structure the two band tight-binding fit to ARPES data provided in [83], this is by construction a perfect match [83,

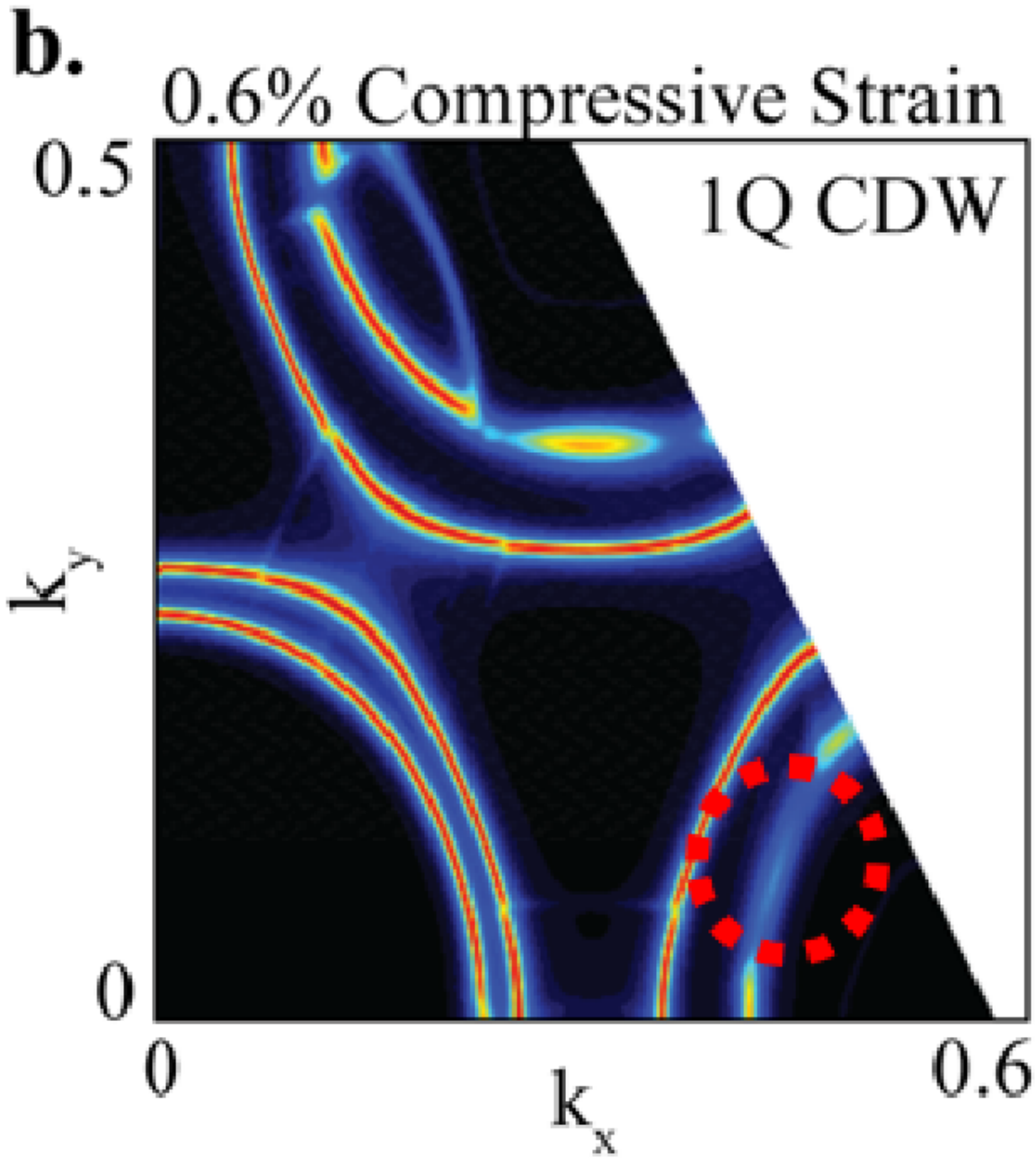

Figure 3.23: ARPES spectral density at the Fermi level for 0.6% compression and '1Q' distorted. Regions where the spectral density is suppressed due to charge ordering are highlighted with red circles.

84]. In Fig. 3.22 we include, at zero strain, the 3Q gap, found self-consistently using the RPA at high-symmetry points in the Brillouin zone and fit to a tight-binding expression taking account of the lattice symmetry [64]. In Fig. 3.23 we include a uniaxial negative

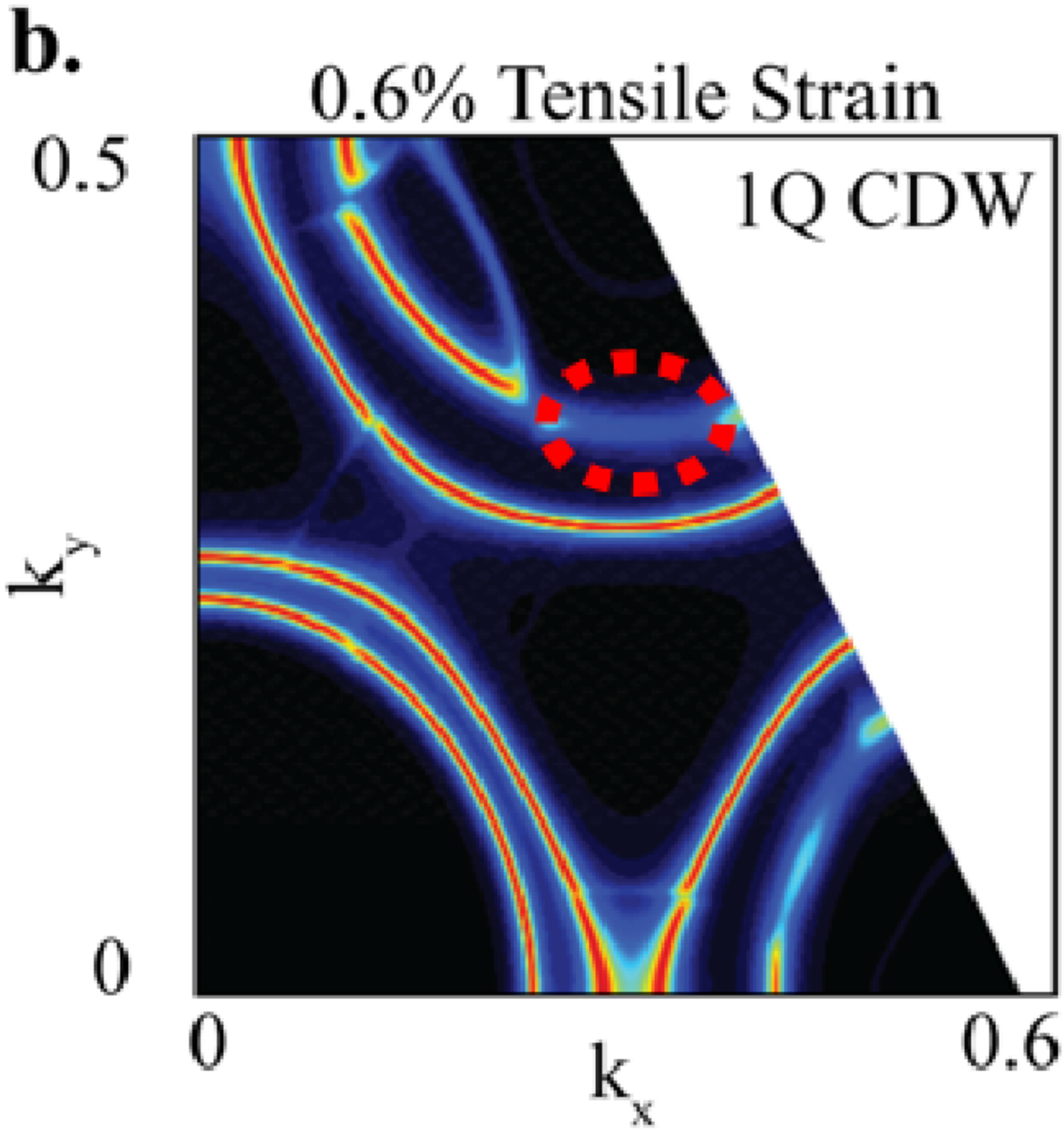

Figure 3.24: ARPES spectral density at the Fermi level for 0.6% extension and '1Q' distorted. Regions where the spectral density is suppressed due to charge ordering are highlighted with red circles.

(compressive) strain along the vertical GM direction by altering the hopping integrals in the electronic bandstructure, and the corresponding terms in the CDW gap expression [73]. The magnitude of the strain equates to around a -0.6% strain in real terms. We include a 1Q gap self-consistently. We find the jump in the free energy across the 3Q to 1Q transition to

be negligible; since the 1Q CDW backfolds less of the Fermi surface, it is important to ensure that the energy gain from the gap opening matches that of the 3Q geometry at the critical point. We calculate the total energy gain in each case by evaluating the average energy $\langle E \rangle$ of the system:

$$\langle E \rangle = \int_{-\infty}^{\infty} \mathrm{d}E E f(E,T) \int_{BZ} \mathrm{d}^2\mathbf{k} A(E,\mathbf{k}) \tag{3.1}$$

where $f(E,T)$ is the Fermi function at temperature T and the $\mathbf{k}$ integral covers the Brilluoin zone. In Fig. 3.24 we include a uniaxial positive (tensile) strain along the same direction via the same method.

Comparing Figs 3.21 and 3.22, at zero strain the 3Q CDW gap opens on the inner pockets around the K points, along the MK lines, in agreement with previous experimental results [83, 84]. Comparing to Figs 3.23 and 3.24 we see that the 1Q gap affects significantly more of the Fermi surface. In particular, the two (now independent) inner K pockets are almost entirely gapped out in both 1Q strain geometries. Since the superconducting gap has to form on whatever remains after the CDW gap develops, this confirms the idea that the suppression of T_c at larger strains is due to competition with the CDW.

3.11 Magnitude comparison to strain effects in other superconductors

The authors of [39] created a plot of the maximal observed strain-induced charge in superconducting transition temperature as a percentage of the superconducting T_c at ambient conditions (Fig. 3.25). We note that by that metric the degree of tunability which we demonstrate in 2H-$NbSe_2$ is only exceeded by Sr_2RuO_4 and the iron pnictides.

3.12 Avenues for further investigation

While the physics of 2H-$NbSe_2$ is an old subject, it is one that over decades continually yielded a wealth of surprises. Our work opens the door on a range of avenues for investiga-

tion which are worth pursuing to obtain a full understanding of the phenomenology of this fascinating material.

In [60], a work which I co-authored, a curious finding is made regarding the pressure dependence of the superconducting order parameters and the superconducting gaps. Those results are summarized in 3.26. It was found that there is a strong pressure dependence of the superconducting order parameter, as measured through the zero temperature superconducting penetration depth extracted through muon spin resonance (μSR) measurements, whereas there does not exist a comparable dependence in the superconducting gaps. An interesting avenue to pursue is the corresponding dependence as function of uniaxial strain, given that there are strong indications from the study presented in this chapter of a transition between

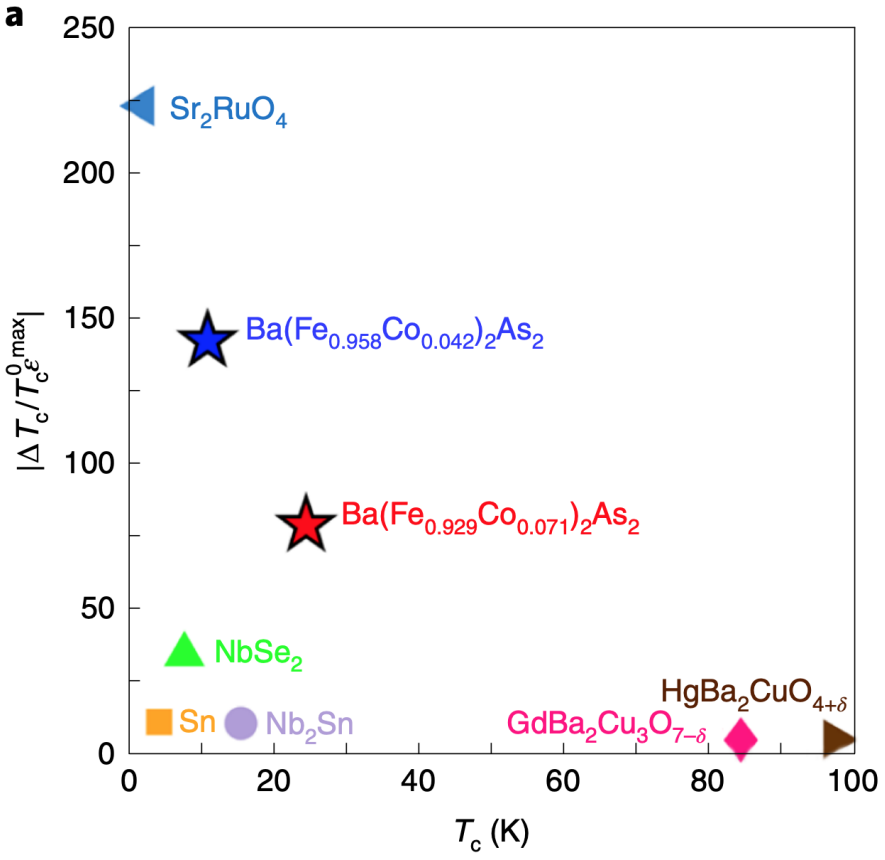

Figure 3.25: Reproduced from [39]. A plot of maximal observed strain-induced shift in superconducting transition temperature, normalized by the ambient superconducting temperature, verus the magnitude of the superconducting transition temperature. The degree of tunability of 2H-$NbSe_2$ is only exceeded by Sr_2RuO_4 and the iron pnictides

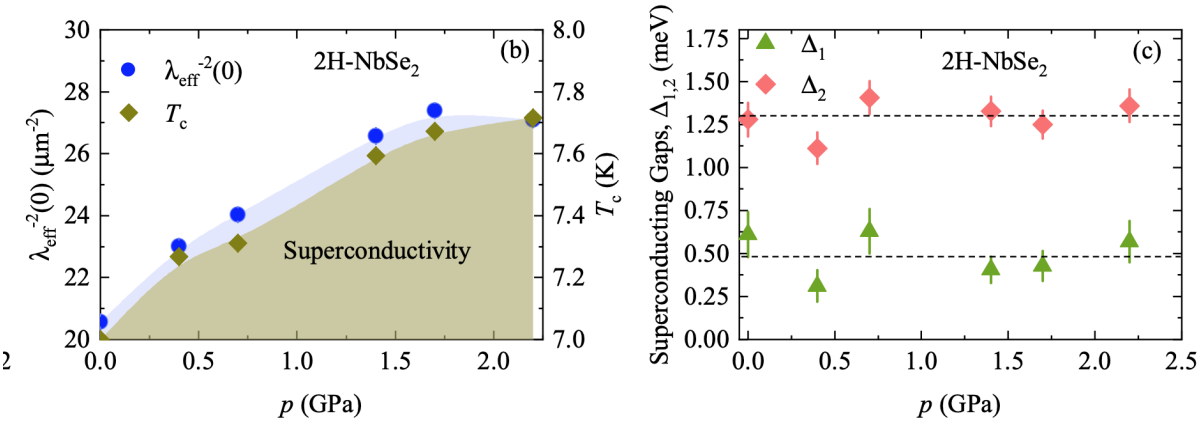

Figure 3.26: Reproduced from [60]. The two panels show the superconducting order parameter (λ_{eff}^{-2}, measured through the zero-temperature inverse squared superconducting penetration depth) and superconducting gap as function of pressure. Curiously the penetration depth shows a large dependence on pressure whereas the pressure dependence of the magnitudes of the two superconducting gaps shows no consistent trend.

alternate charge ordering geometries and their coupling to superconductivity.

Other areas for further study include utilizing scattering probes to investigate the strain dependence of charge ordering in detail. One may study the dependence of the charge ordering parameters (wavevectors) in addition to obtaining the detailed dependence of T_{CDW} which was inaccessible to the techniques employed in the current work.

Another related area is the effect of strain on two-dimensional samples of 2H-$NbSe_2$. Over the last few years a number of high-profile results were obtained in that field [85, 86, 87]. Uniaxial strain is worth investigating as a potential tuning parameter for that system.

Chapter 4: Strain-modulated phase textures in the Mott insulator $Ca_3(Ru_{1-x}Ti_x)_2O_7$

4.1 Introduction

4.1.1 Transition metal oxides

The most exotic physical phenomena manifesting in the solid state are arguably expressed in transition metal oxides, where the interaction of electronic, spin, and lattice degrees of freedom produce "soft" electronic states easily modified by external perturbations [88, 89]. Celebrated hosts for these highly tunable phenomena include high-T_C superconductors, colossal magnetoresistive manganites [90], polar materials like ferroelectrics and ferromagnets [91], and Mott insulators poised near an insulator-metal transition (IMT) [92]. "Passive" strain from substrate epitaxy has emerged as an ubiquitous platform for tuning these phases in oxide thin films, affording stabilization of superconductivity [93, 94] and ferroelectricity[94, 95] while abundantly tuning the insulator-metal transition among classes of correlated oxides like vanadates [96, 97, 98], nickelates [99], ruthenates [100, 101], and manganites [102, 103, 104].

4.1.2 Strain susceptibility effects in transition metal oxides

The phenomenology of transition metal oxides can be understood in terms of the competing influences of reduced dimensionality and crystalline and/or stoichiometric defects. This motivates strain-modulated studies of pristine single crystal of transition metal oxides. These single crystals constitute a playground for working toward an understanding the fundamental mechanisms of strain control in this class of materials.

4.2 "Active" strain control

One mode of strain control, which we may term "active", involves direct mechanical actuation of phase transitions in single crystals. There have been a number of examples of such work in recent years ([5, 105, 106, 107]), including in the context of the insulator-metal transition of 3d metal oxides [108, 96]. Strain studies provide a wealth of new insights into the strain susceptibility of functional electronic phases. Pertinent to the work described here, this approach was recently leveraged to explore lattice coupling of competing phases in the 4d ruthenates [109, 110].

4.3 Intrinsic vs. emergent strain susceptibilities

Intrinsic predisposition of these systems towards coexistence of competing phases, especially in the case of functionally triggered first order phase transitions, now motivates application of microscopic probes capable of discerning strain susceptibilities arising from individual phases. In this work we distinguish such "intrinsic" susceptibility from "emergent" susceptibility associated with textured phase coexistence, a phenomenon owing generically to strain-coupling of phases observed, for example, in many IMTs [111, 112, 17, 113]. Here we demonstrate the emergence of an elastic susceptibility associated directly with domain configurations of phases coexisting in a spontaneous nano-texture across the IMT of a prototypic Mott crystal – Ti-substituted $Ca_3(Ru_{1-x}Ti_x)_2O_7$ (hereafter denoted CTRO).

4.4 Phenomenology of $Ca_3(Ru_{1-x}Ti_x)_2O_7$

The parent bilayer perovskite ruthenate $Ca_3Ru_2O_7$ (CRO) exhibits an IMT at T_{IMT}=48K, although with a directionally gapped Fermi surface surviving to low temperatures [115, 116] characterized by antiferromagnetically coupled ferromagnetic bilayers. This "soft" IMT is ascribed to a Peierls-like charge density wave instability presaged by several competing antiferromagnetic phases. On the other hand, substituting Ru by 3d metals like Ti can

produce an IMT completely distinct from that in CRO. For instance, Ti substitution at x>4% induces a non-Fermi surface-driven magnetic instability to G-type antiferromagnetic ground state, characterized by a gapped band structure along all axes [116, 114] whereby TIMT increases with substitution level [114]. This first-order IMT, identified by a hysteretic jump in resistance over four orders of magnitude tall, could not be predicted at the level of single-particle density functional theory[116], implicating Mott physics. Moreover, that Ti^{4+} and Ru^{4+} cations have similar ionic radii rules out trivial origins for the IMT based on substitutional lattice distortion. Rather, the absence of states near the Fermi level associated with localized Ti t_{2g} orbitals is expected to scatter itinerant carriers, as observed directly by STM probes of quasiparticle scattering in related Ti-substituted strontium ruthenates[117,

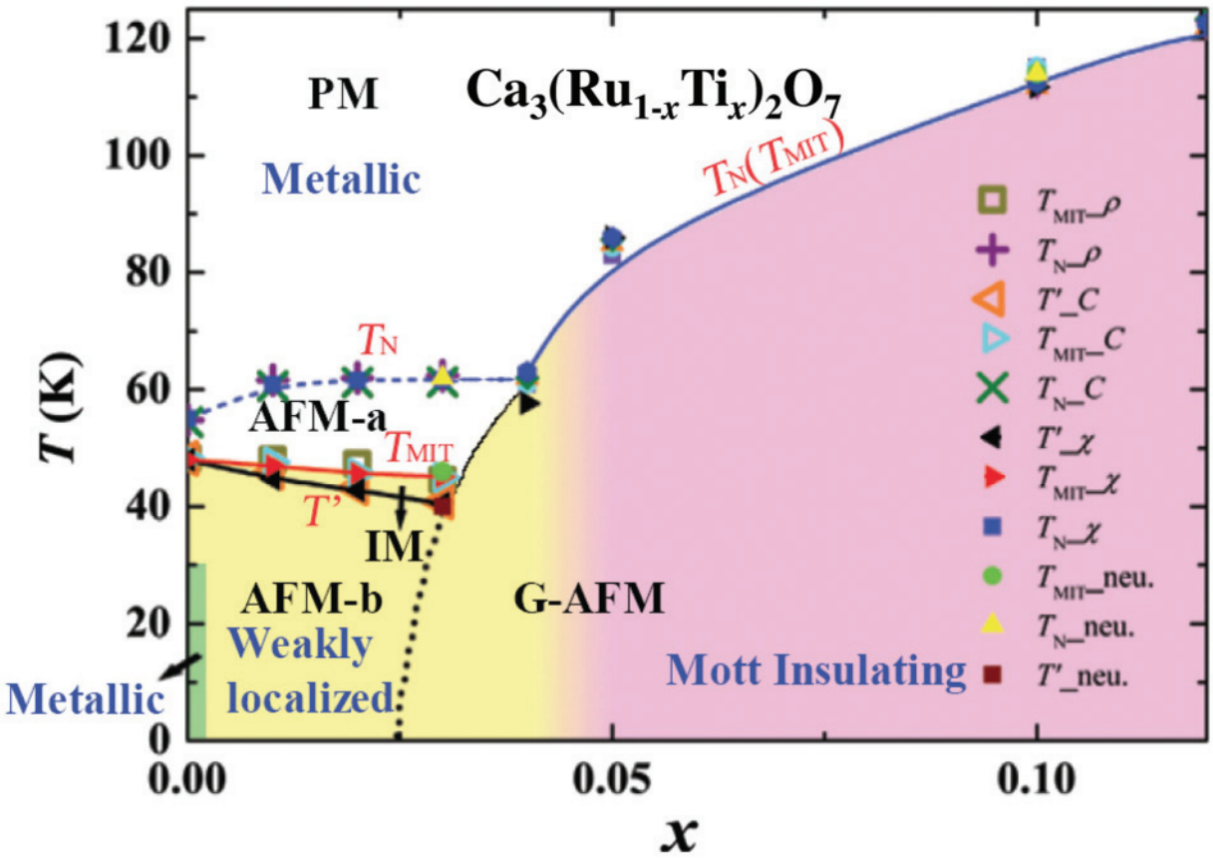

Figure 4.1: Reproduced from [114]. Phase diagram of $Ca_3(Ru_{1-x}Ti_x)_2O_7$ as function of Ti substitution fraction, x.

118]. These scattering centers likely effect band-narrowing in the Ru orbital manifold [114, 117], suggesting a bandwidth-controlled Mott transition. The symmetry preserving ($Bb21m$ space group) orthorhombic structural transition from the high-T metallic ("L") phase with comparatively long c-axis to low-T insulating ("S") "short" phase might be dubbed "coelastic" [119], with an uncommonly large spontaneous strain of +1.1% along b-axis and -0.85% along c-axis in x=3% CTRO [116], almost an order of magnitude enhanced compared to the IMT of pure CRO[120]. At the level of electronic structure, this flattening distortion was implicated in lifting the degeneracy of xy and xz/yz orbitals in the Ru t_{2g} manifold, inducing an orbital polarization essential for stabilizing the Mott insulating phase[121, 122]. In fact, *ab initio* calculations and doping-controlled experimental studies seemingly identify lattice-tuned orbital polarization as the underlying physical parameter controlling TIMT and the Mott gap[122]. Hydrostatic compression [123] as well as high magnetic field[121], both accompanied by anomalous elongation along the c-axis, weaken the Mott state in CTRO and suggest opportunities to tune the IMT by c- or b-axis uniaxial strain. Lastly, this bilayer ruthenate is also remarkable for the inequivalent b-axis displacement of its three formula unit Ca ions [124, 125] that foreseeably impart a polar dipole moment to the Mott insulating phase, rendering hybrid improper ferroelectricity similar to other bilayer perovskites[126, 127]. The microscopic consequences of polar domains for the Mott transition have hitherto gone unexplored.

4.5 Multi-messenger nano-imaging

In this work we directly reveal progression of the insulator-metal transition for the first time in x≥5% polar CTRO using a multi-messenger nano-imaging approach.[104] This method combines application of 10 nanometer-resolved scanning near-field infrared microscopy (nano-IR), which provides a faithful probe of optical properties at deeply sub-wavelength spatial resolutions, with contemporaneous scanning probe sensing modalities like Kelvin probe force microscopy (KPFM), applied here to resolve the work function of domains across the

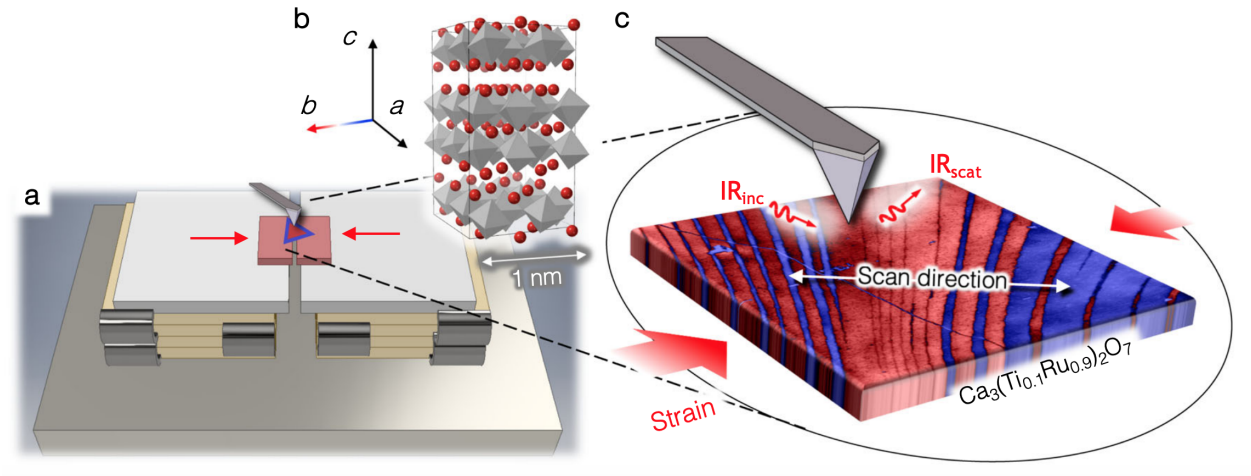

IMT. Our nano-IR probe is amply suited to distinguish insulator and metal domains emerging across the IMT[18] by way of the optical scattering signal (defined and described in Methods), even at the cryogenic temperatures requisite to study CRO [113, 21]. Moreover, leveraging a new nano-resolved protocol denoted scanning nano-susceptibility imaging, we directly reveal the influence of lattice-orbital coupling on the insulator-metal transition. Harnessing this approach to tune and visualize Mott nano-textures close to T_{IMT} enables our direct measurement of an elastic "domain susceptibility" intrinsic to the ordered texture of phase coexistence reported here.

4.6 Experimental techniques

Figure 4.2: Schematic depiction of a 100 micron-scale thin Ca3(Ti0.1Ru0.9)2O7 crystal mounted to a home-built strain stage inside the low-temperature nanoscope. b) Crystal structure of the bilayer ruthenate; strain is applied approximately along the crystallographic b-axis. c) Metal / insulator nano-textures are detected by nano-imaging the crystal surface (ab-plane) at 100 meV probing energy during in situ application of strain.

To enable studying the response of the phase transition to in situ applied strain, individual CTRO single crystals of characteristic dimension 100x50x10 microns (length width depth) were glued with their long dimension across the 50-micron gap between the two shear

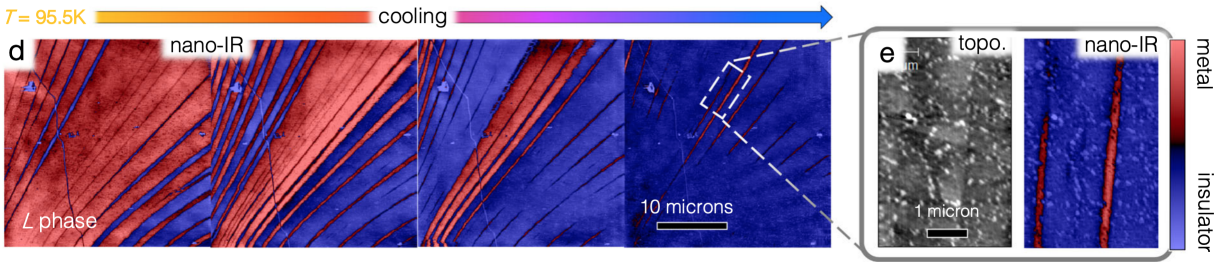

piezoelectric stacks of a home-built uniaxial strain stage (Fig. 4.6). With this "strain stage", relative displacements of ~ ± 1 micron can be achieved between the two sheer stacks at their top surface with a differential bias of ±500V at a temperature of T 100K, thus enabling application of quasi-uniform uniaxial strains exceeding ±2% to samples of suitable dimension (see Chapter 2). For nano-imaging experiments, individual single crystals were cleaved in the [001] plane and pre-mounted with [010] orientation across the gap (Fig. 4.6) to our custom strain stage, integrated with an electrically enabled sample holder, and delivered into the ultra-high vacuum cryoSNOM chamber and sample receiver by manipulator arm. Within the sample receiver, electrical contacts were established kinematically to the piezoelectric actuators and to source/drain electrodes across the crystal. Sample temperatures were registered in situ by a diode sensor mounted to the strain stage.

Figure 4.3: Striped nanotextures emerging while cooling the crystal from the metallic L phase through the Mott transition from T=74.5K to 73.5K without applied external strain (left). Minority phases take the form of acicular domains (right).

4.7 Imaging results

4.7.1 Nano-infrared imaging of thermal IMT

Figure 4.4: Correlative topography, contact potential difference Δ (see text) and nano-IR signal recorded across of a series of L phase domains.

We first consider the insulator-metal transition of 10% Ti-substituted CTRO crystals, with a strongly first order transition temperature T_{IMT} ~95K. Near the transition, nano-

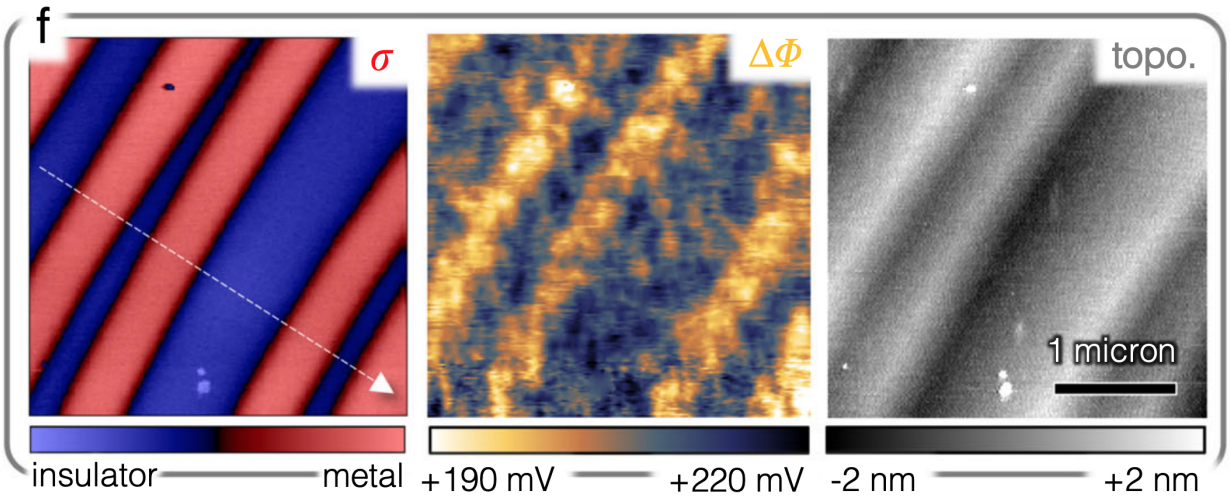

IR imaging of large-area [001] crystal facets reveals an emergent striped texture of metal and insulator domains as shown in Fig. 4.6, where the nano-IR signal is registered in false color (color scale as in Fig. 4.6. Fig. 4.6 presents the distribution of metal and insulator regions recorded by nano-IR imaging in the same field of view while cooling the sample through the transition from T=95.5K to 94.5K, showing nucleation and growth of insulating S phase domains in the form of stripes with a characteristic periodicity of several microns perpendicular to the crystallographic b-axis. At the conclusion of the phase transition, nano-IR reveals extremely narrow metallic L phase domains persisting in an insulating background (Fig. 1e, right panel), whereas the surface topography (left panel) shows linear surface deformation emerging with the larger L phase domain.

Figure 4.5: Correlative line-profile along the arrow in figure 4.7.1 associated with each imaging channel; the surface work function anticorrelates local metallicity, and expansion of L domains buckle the surface topography.

4.7.2 Multi-messenger imaging of the stripe texture

To further interrogate sub-micron features associated with phase coexistence, Fig. 4.7.1 presents a multi-messenger nano-imaging examination of a 3x3 micron striped texture emerging at T=95K. Here we utilize the simultaneous combination of nano-IR imaging, Kelvin

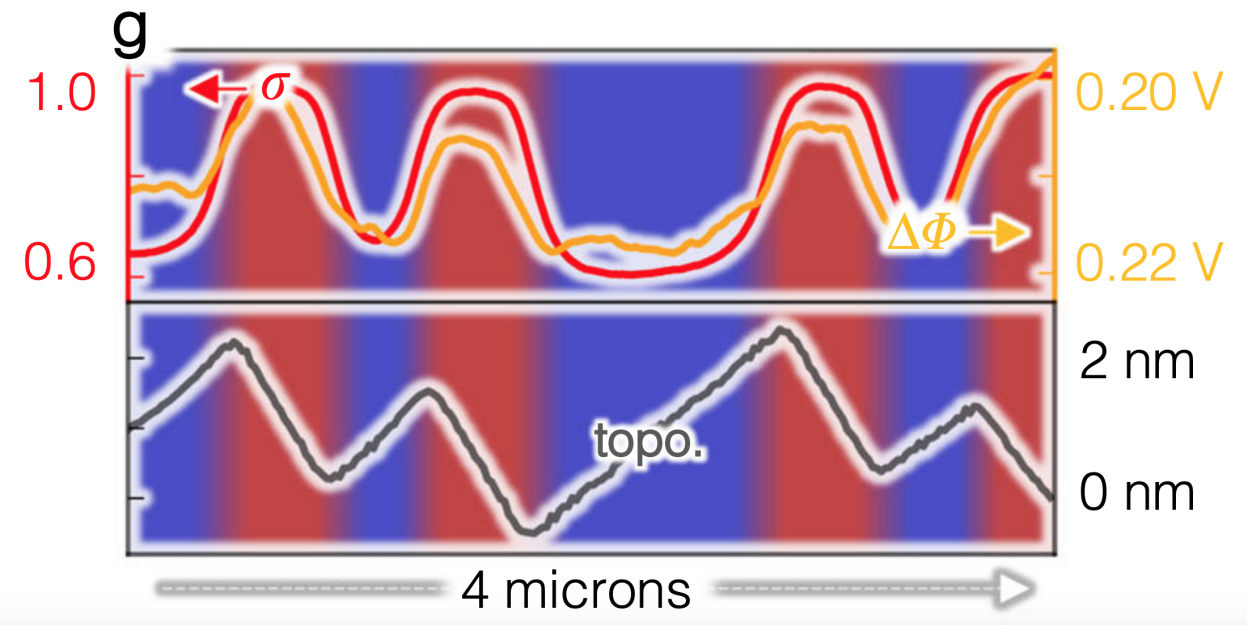

probe microscopy, and atomic force microscopy to respectively correlate local metallicity (left panel), work function (center), and surface topography (right) associated with these coexisting striped domains. Fig 4.7.1 compares the correlative spatial evolution of these properties across the dashed line in the left panel, which over a 4-micron distance intersects several L- and S-phase domains. The nano-IR response (red curve) reveals inter-phase boundaries sharp on the scale of 200 nm. However, the local work function (orange curve), registered by KPFM as the "contact potential difference" $\Delta\Phi_{=}\Phi_{CTRO} - \Phi_{tip}$ between work functions of the sample and the nano-IR probe (Methods), consistently anti-correlates in real-space with local metallicity. We detect an increase in work function $\Delta\Phi_{CTRO} = \Phi_L - \Phi_S$ from the metallic L to the insulating S phase of about 30 mV, consistent in magnitude with opening of the latter's semiconducting gap [123] and similar to the change in work function through the insulator-metal transition of an analogous correlated oxide, VO2 [21].

The central panel of Fig. 1f shows spatial variations in Δ of order 5 mV at characteristic length scales of 100 nm, comparable to the spatial resolution of our KPFM technique, indicating extreme sensitivity to variations presumably in surface oxidation of the crystal facet, cleaved ex-situ under ambient conditions prior to attachment onto our strain stage.

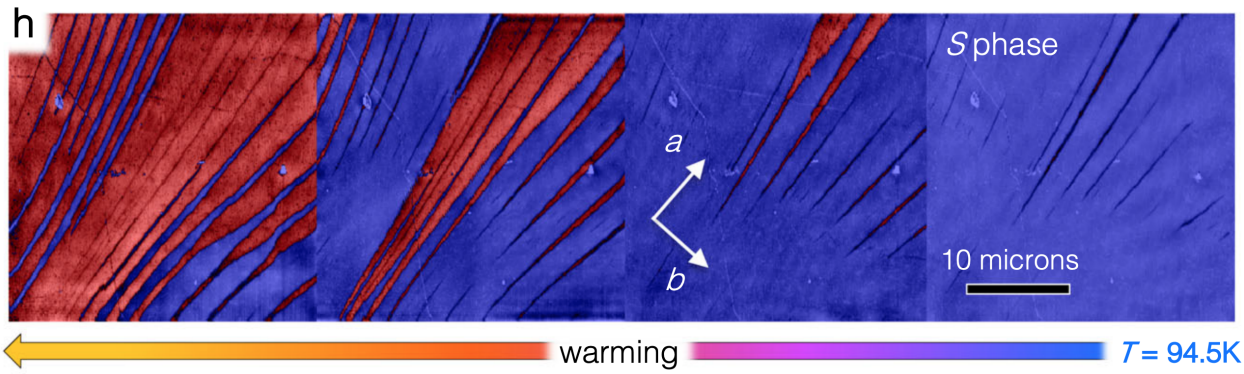

Figure 4.6: Same region as 4.6 imaged while warming from the insulating L phase.

These variations (details we defer to forthcoming work) show no noticeable association with the local surface topography (Fig. 1f, right), which is atomically smooth to the precision of our AFM, with exception of notable buckling in the crystal surface on the scale of several nanometers associated directly with the underlying L and S phase domains; the bottom panel of Fig. 1g highlights this association. While similar to observations in phase-change oxides like VO_2 and V_2O_3 thin films [128, 113], this unique buckling pattern signifies the underlying domain structure of coexisting L and S phases into the volume of this ruthenate single crystal [129]. In particular, we expect the nearly 1% expansion in c-axis lattice constant through the metal-insulator transition32 to dominate buckling of the [001] surface, whereas the accompanying >1% b-axis contraction should influence the preferred orientation of inter-phase domain boundaries.51 As shown schematically in Fig. 1i, detailed considerations of elastic energy minimization (SI) in this case predict inter-phase domains oriented nearly along [011] and [011] directions, and the latter is qualitatively consistent (SI) with the observed "angled" buckling pattern with topographic peaks and troughs aligned along L-S and S-L inter-phase boundaries, respectively (Fig. 1g). Fig. 1h presents the same field of view as Fig. 1d imaged while warming the sample back to 95.5K, where the reverse scenario of nucleation and growth of L phase domains proceeds through the insulator-metal transition. These introductory characterizations reveal that i) nano-IR and KPFM imaging are faithful probes of the low-temperature CTRO insulator-metal transition, ii) striped domain

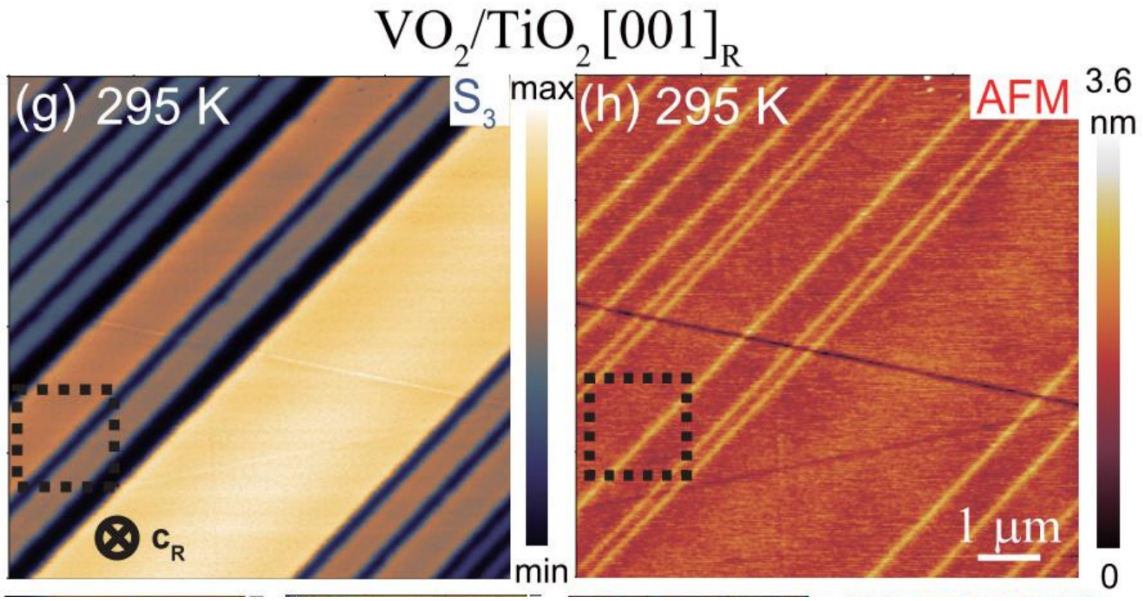

Figure 4.7: Reproduced from [128]) Infra-red scattering amplitude S_3 of 30nm VO_2/TiO_2 $[001]_R$ film. The substrate induces a strain dependent metallicity. Formation of stripe patterns of metallic and insulating domains is observed.

textures are dominated by elastic energetics of incommensurate L and S structural phases, and iii) our nano-imaging probes register a two-dimensional cross section of an underlying three-dimensional domain texture forming spontaneously throughout the crystal volume during the IMT.

These observations uncover the intrinsic potential of long-range strain fields to dictate the spatial texture of insulator-metal phase coexistence, prompting our application of external uniaxial strain to manipulate these phase textures in situ.

4.7.3 Strain susceptibility of the stripe texture

We begin by registering the resistive transition of a single microcrystal mounted to our strain stage at fixed levels of uniaxial strain aligned nearly along the crystallographic b-axis. Fig. 2a presents thermal sweeps of the full resistive transition under application of exemplary tensile (positive) and compressive (negative) b-axis strains, revealing an overall shift of the resistance curve by several degrees K under less than half a percent strain application.

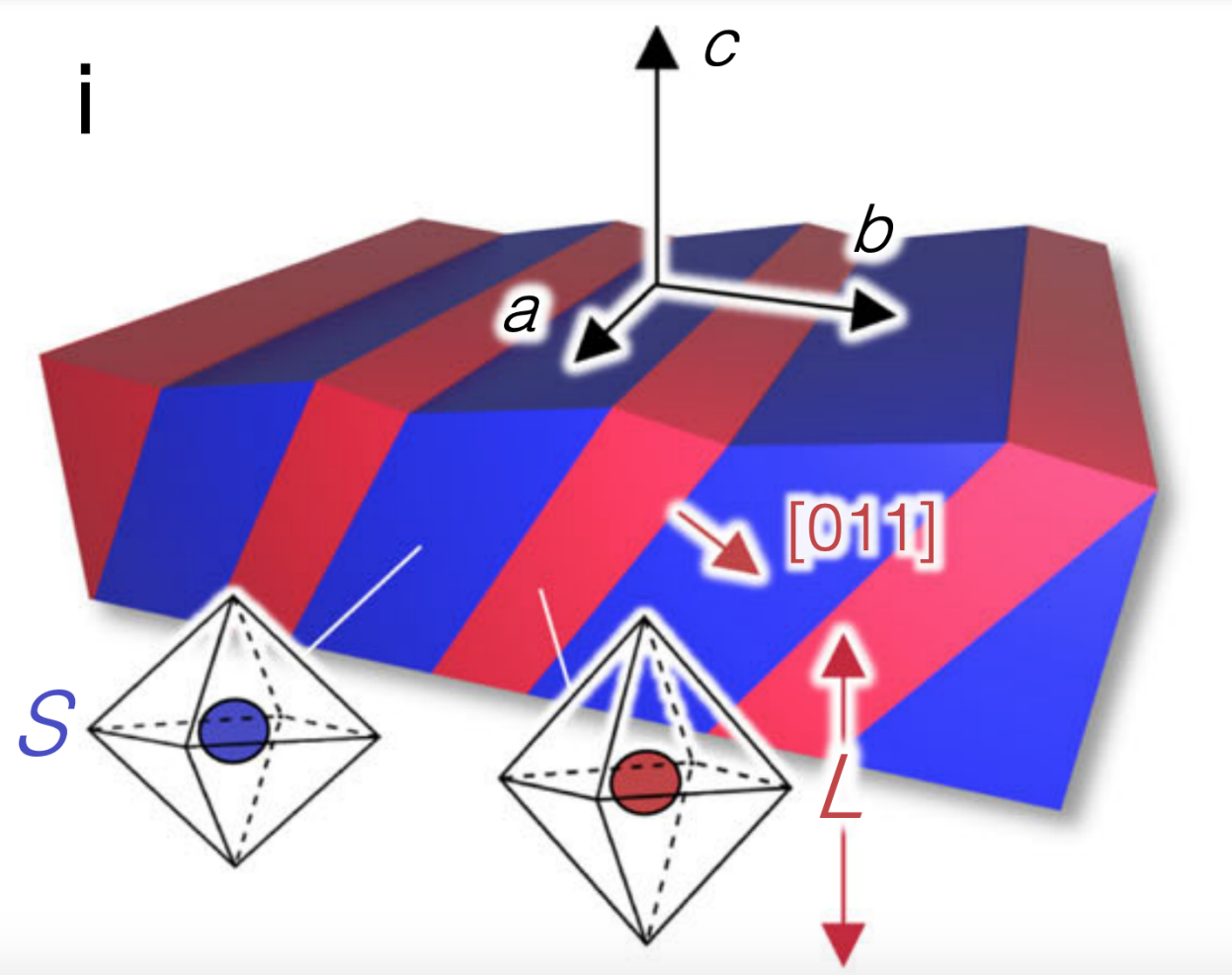

Figure 4.8: Inferred schematic structure of coexisting L and S domains ([011] habit plane) showing associated RuO_6 octahedral deformations.

Defining a "characteristic" transition temperature T_{IMT} by the onset of a sharp upturn in sample resistance (viz. maximum in $R^{-1}\partial R/\partial T$) entering the insulating state, Fig. 1b summarizes elastic susceptibility of the resistive transition. Whereas T_{IMT} is approximately 95K for the unstrained crystal, modest application of 0.5% tensile strain (strain calibration detailed in Chapter 2) shifts the transition temperature by +2.5K, whereas -0.5% compressive strain suppresses the transition by -2.5K, signifying an enormous uniaxial b-axis elastic susceptibility of $\partial T_{IMT}\partial\epsilon = 5 \times 10^2$K (ϵ hereafter denotes the b-axis dilatory component of the 2nd rank strain tensor $\underline{\epsilon}$). Qualitatively, we envision that i) compressive stabilization of the reduced-b axis S phase and ii) tensile stabilization of the enlarged-b axis L phase together form an underlying mechanism for this susceptibility.

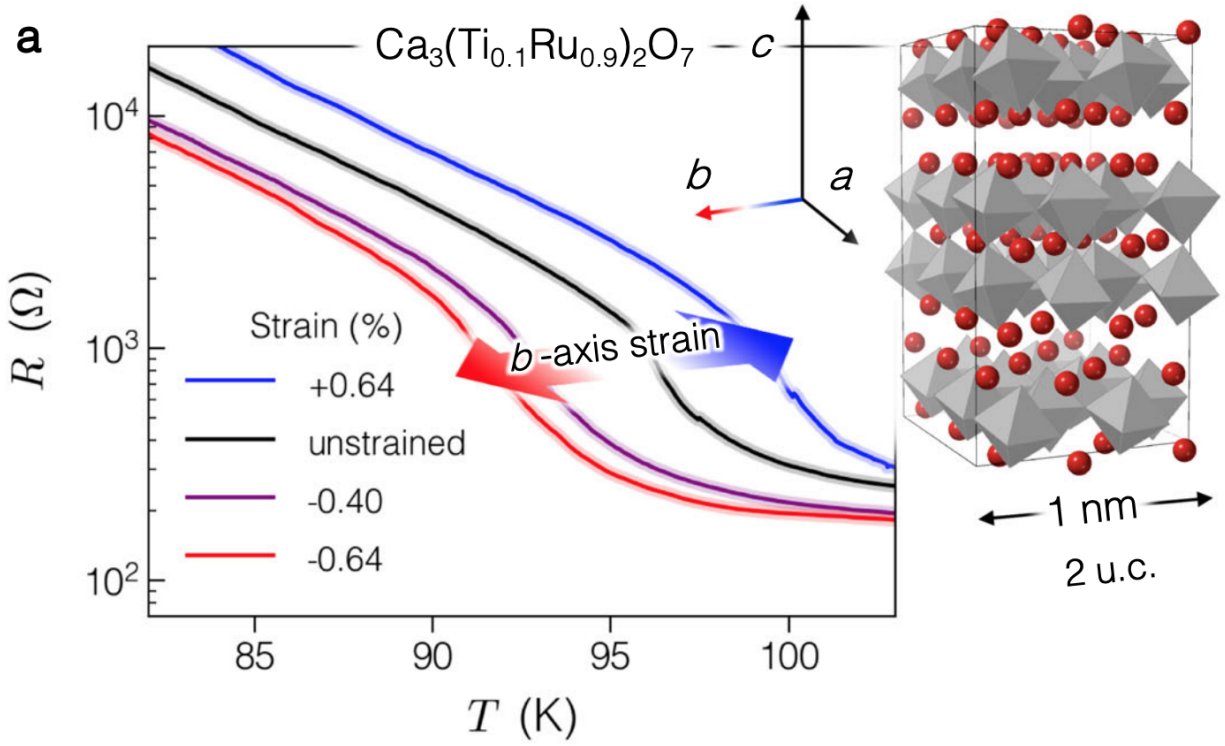

Figure 4.9: Two-probe electrical resistance of the crystal in Fig. 1 across the insulator-metal transition under compressive ($\epsilon < 0$) and tensile ($\epsilon > 0$) b-axis strain conditions; the overall resistive transition shifts in temperature. Crystallographic axes are labeled on eight rendered unit cells of the crystal structure.

4.7.4 Scanning Nano-susceptibility Imaging

To test this hypothesis, we performed in situ nano-IR imaging of the same microcrystal at T=95K under comparable strain conditions. By continuously scanning perpendicular to the insulator-metal stripes (parallel to the b-axis, indicated in Fig. 4.6, monitoring the nano-IR signal , and simultaneously sweeping the level of uniaxial strain delivered to the crystal, we directly resolved the real-space impact on insulator and metal phases. Fig. 4.11 reveals the 1-dimensional lateral distribution (along the horizontal spatial axis) of insulator-metal domains from an initially unstrained configuration (bottom), and continuing first to a 1% compressively strained state where we resolve outward growth of preexisting metallic S phase stripes. Next, application of 1% tensile strain reduces the areal fraction of metal, yielding a majority insulating state where several metallic domains have vanished completely. This protocol of "scanning nano-susceptibility imaging" (SNSImaging) is entirely reversible, as demonstrated by the concluding (top) majority metallic configuration replicated at 1% compressive strain.

Note that this strain application is accompanied by an overall leftward (rightward) shift

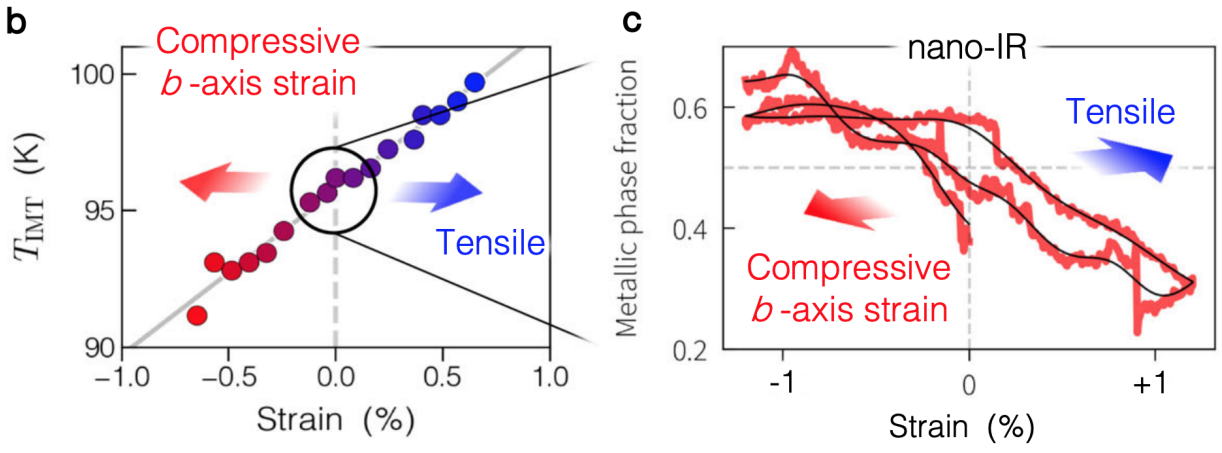

Figure 4.10: Left panel: Insulator-metal transition temperature T_{MIT} (identified by a peak in $R^{-1}dR$ versus applied b-axis strain. Right panel: Areal metallic phase fraction at T=95 K identified by repeatedly nano-imaging along the line identified in Fig. 4.6 versus in situ applied strain; phase fractions can be modulated by 40% under a 2% variation in strain. Small arrows indicate the strain sweep sequence.

of the scanned field of view due to physical motion of the crystal during compressive (tensile) actuation of the strain stage. Since these data are dominated by the growth and reduction of pre-nucleated metallic domains (rather than nucleation of new domains), and since our scan perpendicular to the orientation of these stripes provides a faithful view of their overall size, we can quantify the elastic susceptibility of these phases by recording the metallic phase fraction versus strain after excluding the contribution of metallic domains that enter or leave the field of view. Fig. 4.10 presents the metallic phase fraction f extracted in this fashion versus strain, revealing a roughly linear dimensionless elastic susceptibility $_{elas} = \partial f / \partial \epsilon$ of at

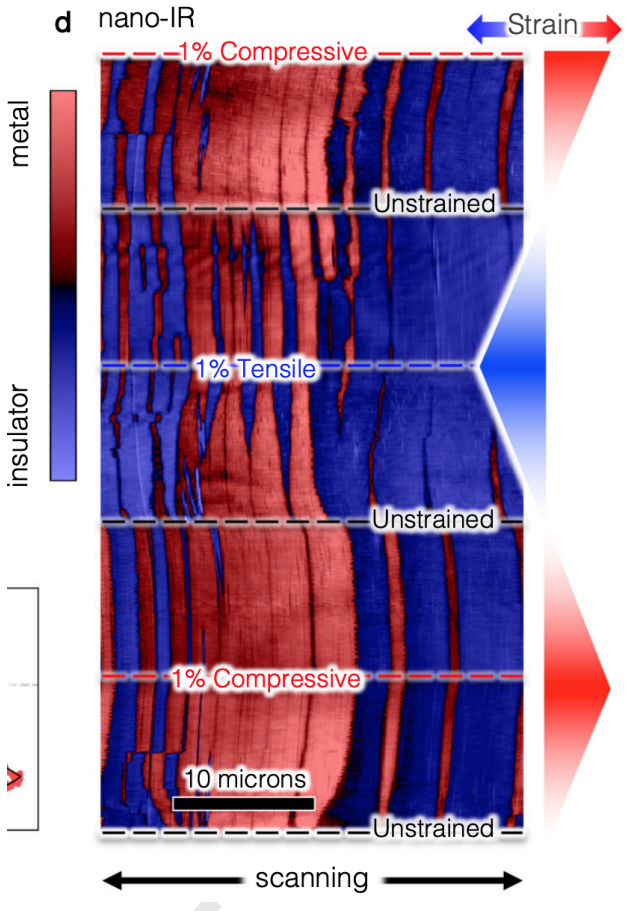

Figure 4.11: Spatially resolved insulator-metal nano-texture along the same scan line quantified in the right panel of 4.10 versus dynamically tuned strain; beginning from an unstrained state (bottom) metallic domains enlarge under ϵ =-1% compressive strain, then diminish under ϵ =+1% tensile strain, and can be reversibly restored under renewed compressive strain.

least 15, suggesting the possibility to completely modulate an isothermal Mott transition in CTRO at a b-axis strain of 15-1≈7%. While this presumably exceeds the damage threshold for our 10 microns-thick single crystals (and the range of the strain stage used in this study), it is consistent with the typical strains demonstrated to modulate the Mott transition in thin films of the related ruthenate Ca_2RuO_4 [100, 101, 130] and is foreseeably accessible without damage in thin perovskite membranes [131]. Given the apparent orientation of stripe domains in this crystal (viz. Fig. 1d) and evident misalignment of the b-axis by as much as 30o relative to our applied strain, these observations demonstrate a robust strain susceptibility. This owes perhaps to vanishing strain susceptibility along the crystal a-axis, which we might anticipate from the reported constancy of the a-axis across the insulator-metal transition for $Ca_3Ru_2O_7$. crystals with substitution levels of 3d metals similar to our own [122].

Notably, we associate the minimal strain hysteresis presented in Fig. 4.10 solely with the memory effect of piezoelectric actuators used on our stage, suggesting surprisingly prompt responsivity of the striped insulator-metal microtexture to applied strain. To interrogate this pliancy in greater detail, we conduct SNSImaging on another crystal presenting a more uniform quasi-1-dimensional "domain lattice" texture at several fixed temperatures through the Mott transition. The upper panel of Fig. 4.12 presents thermal SNSImaging recorded parallel to the crystal b-axis while linearly ramping the sample temperature from 80K to 95K under zero applied strain, revealing initial nucleation of S-phase stripes that settle into a quasi-1-dimensional lattice texture with uniform 2 μm periodicity, followed by a relatively abrupt merger of metallic domains into a uniform state at $T \approx$93K.

We next cycle the sample temperature, and warm again to fixed temperatures indicated in upper panel of Fig. 4.12 by colored arrows whereupon we perform strain-modulated SNSImaging. These temperatures are chosen to stabilize distinct initial configurations of the domain lattice to register χ_{elas} at (unstrained) metallic phase fractions of 10, 30, 60, and 90% associated with the panels in Fig. **??**, where colored dots correspond to temperatures

identified by the colored arrows. At the beginning of the IMT, the lower right hand panel of Fig. 4.13 records SNSImaging from an initially +1% tensile strained configuration with only a few pre-nucleated metallic domains, but after strain removal followed by application of -1% compressive strain we observe nucleation and growth of 4-5 additional metallic domains that position spontaneously to establish the characteristic lattice periodicity. This response is reversible across the subsequent strain sweeps indicated by adjacent blue (tensile) and red (compressive) colored shading.

This regime of strain-modulated phase coexistence is plainly dominated by induced nu-

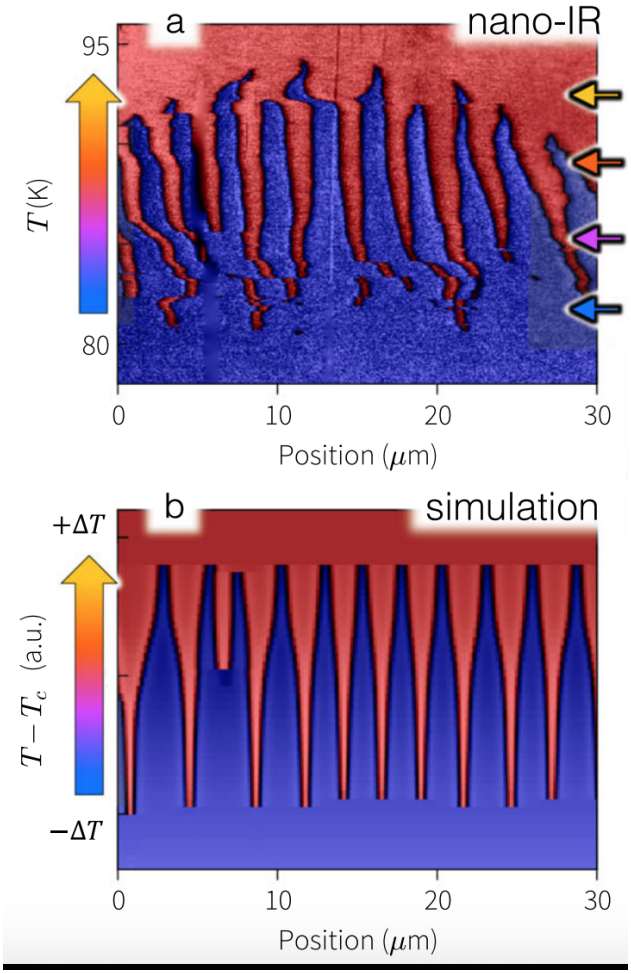

Figure 4.12: Upper panel: Repeated nano-imaging along a fixed-line parallel to the b-axis of a 300 micron-long rectangular crystal while linearly warming the sample temperature resolves thermal evolution of domain textures. Lower panel: A phasefield simulation of a strain-coupled transition (see text) replicates the observed domain evolution.

cleation, whereas the upper right hand panel of Fig. 4.13 presents a quite different response at 30% metallic fraction. Here preexisting metallic domains undergo a complex "dance" of mergers (splitting) under compressive (tensile) strain as a means to grow (shrink) the metallic phase fraction; these events are accompanied by a positional shift of adjacent stripes by a single lattice spacing seemingly to maintain integrity of the domain lattice and prevent dislocations. Meanwhile, at higher initial metallic phase fraction (60%, Fig. 4.6), the domain lattice becomes notably "stiff" and comparatively insensitive to our application of external strain, neither shifting nor appreciably growing existing domains. Lastly, the lower left hand panel of Fig. 4.13 presents the domain susceptibility from a dominantly metal-

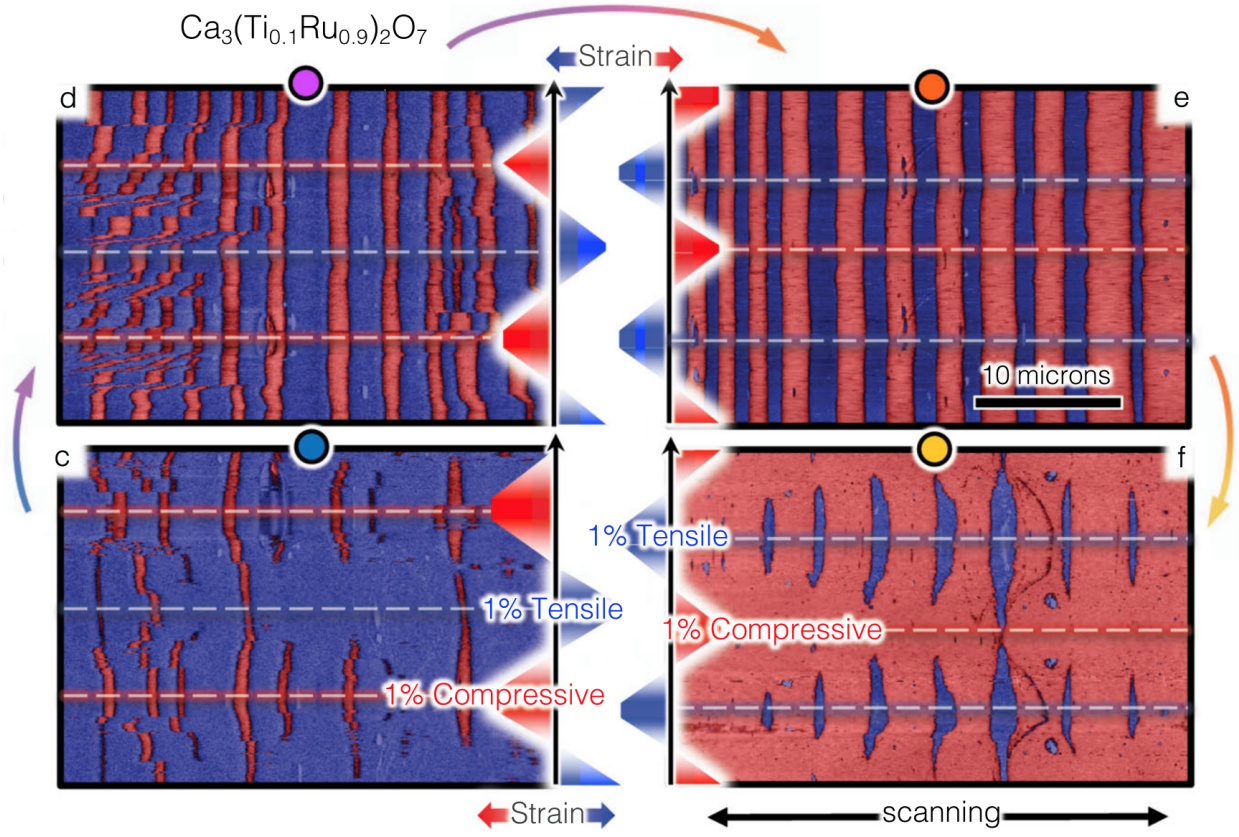

Figure 4.13: Repeated nanoimaging along the same line as 4.12 but at fixed temperatures, identified by colored circles associated with arrows in 4.12, and under programmable strain-sweeps. Lower left panel: at low temperature compressive strain nucleates metallic stripes; Lower right panel: at high temperature tensile strain nucleates insulating stripes; Upper left and right panels: intermediate temperatures alternatively reveal rigidity or complex rearrangement of domain textures.

lic configuration (in the identical field of view) near the conclusion of the IMT, where we find comparatively large elastic response capable of both nucleating and growing insulating domains to an areal fraction exceeding 20%.

4.8 Nano-resolved elastic domain susceptibility

Our SNSImaging results systematically demonstrate a detailed non-uniformity in elastic susceptibility of the domain lattice versus temperature, as summarized in Fig. 4.14. Here we superimpose the unstrained temperature-modulated metallic phase fraction $f(T)$ (red curve, extracted from the same sample region in Fig. 3a) with its associated thermal susceptibility

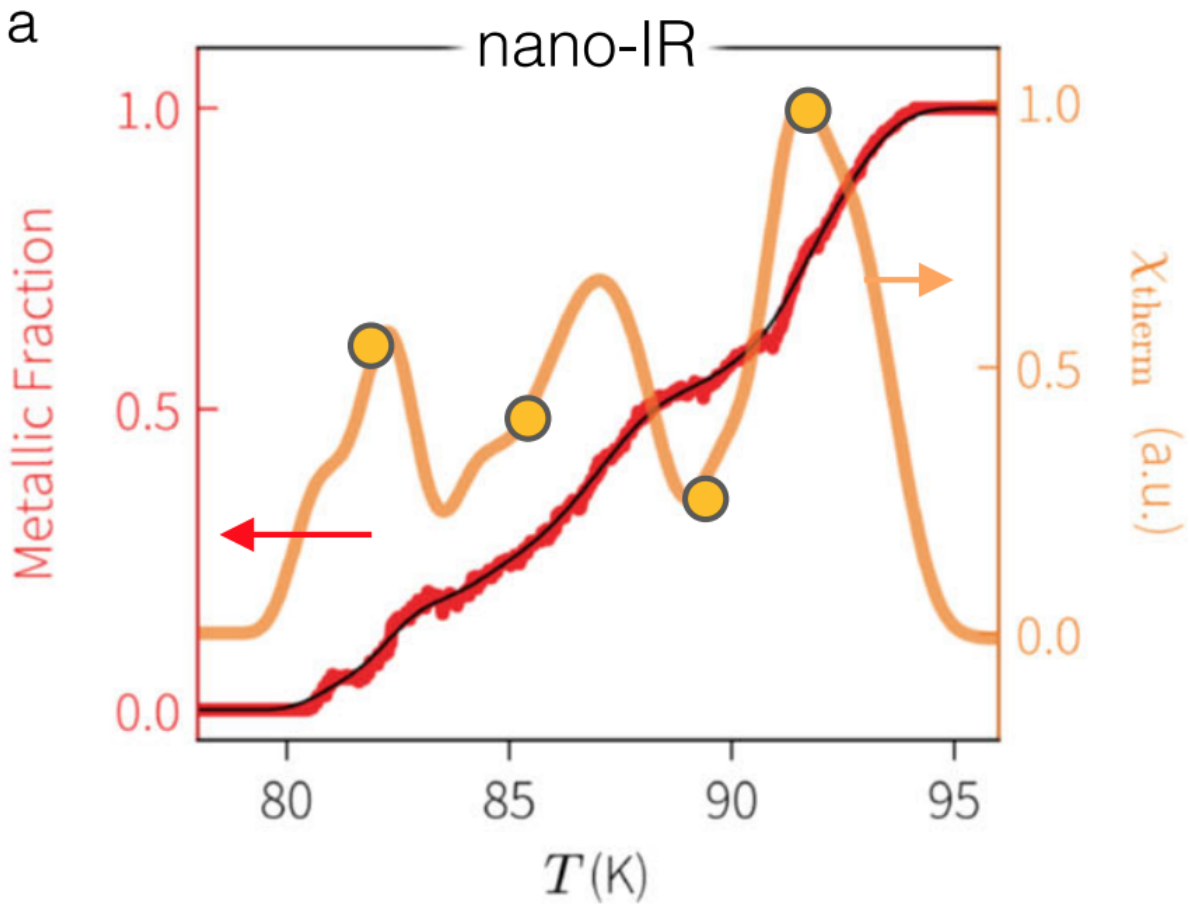

Figure 4.14: T-dependent metallic fraction f from Fig. 4.12 together with thermal susceptibility $\chi_{therm} = df$ (orange); circular points quantify the elastic susceptibility $\chi_{elas} = df\dot{\epsilon}$ identified at similar temperatures from Fig. 4.13.

(viz. $\chi_{th} = \frac{\partial f}{\partial T}$, orange curve, smoothed); we scale the latter to its maximum value. Instead of a constant ramp or sigmoidal progression, $f(T)$ presents a series of three "jumps" separated by valleys of comparatively reduced susceptibility; this behavior manifests as three peaks in therm at $f \approx$15, 40, and 85%.

Such three-fold progression in $f(T)$ was reproducibly verified by SNSImaging at two other sample regions also presenting a near-uniform domain lattice (not shown). Moreover, when we add distinct data points (orange markers) reflecting the variable χ_{el} extracted from data in Figs.4.6 and 4.7.1 1c-f ($\chi_{el} = \frac{\Delta f}{\Delta \epsilon}$ with constant $\Delta\epsilon$=2%; scaled again to highest χ_{el}), we find intriguing qualitative agreement with these systematic variations in χ_{th}. We suppose these non-monotonic trends in susceptibility are nontrivially tied to the elastic energy "landscape" which also dictates the quasi-equilibrium configuration of the domain micro-texture.

4.9 A Landau theory of strain-coupled IMT

We employ a simplified Landau theory of the strain-coupled IMT to reveal essential physics underlying these energetics. Denoting by ψ the amplitude of the coelastic distortion

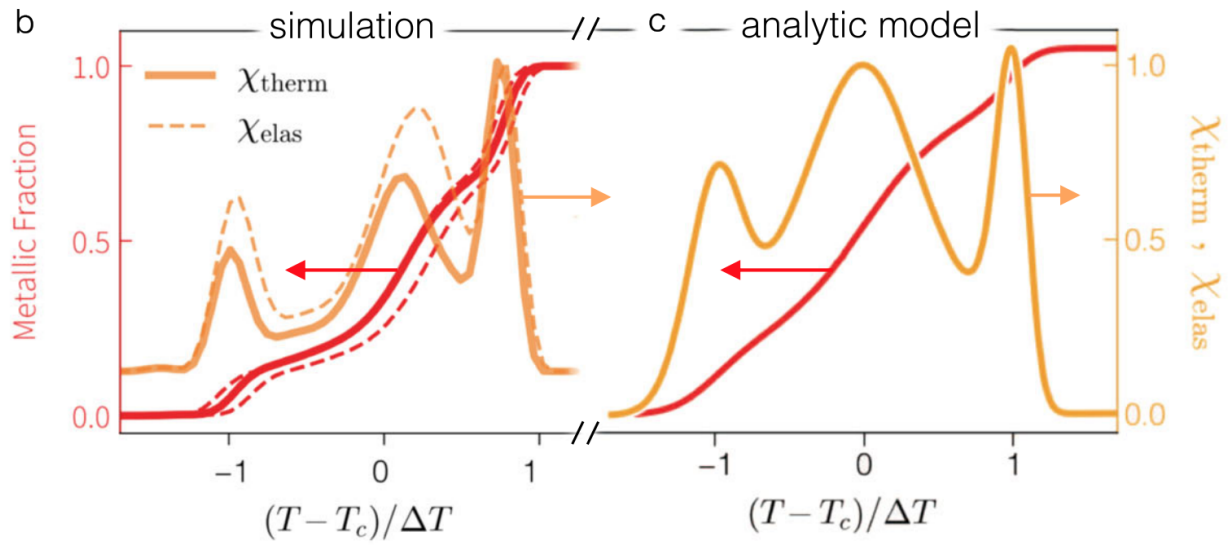

Figure 4.15: Phasefield simulations (left) and a semi-analytic model (right) of domain evolution both predict the characteristic temperature dependence of χ_{therm} and χ_{elas} .

describing the insulating S-phase ($\psi > 0$, meanwhile denoting the L-phase by $\psi = 0$) we can approximate the Landau free energy density F of this first-order insulator-metal transition to quartic order in by:

$$F \approx \frac{1}{2}\kappa|\nabla\psi|^2 + a(T - T^0_{IMT})\psi^2 - \beta\psi^3 + \gamma\psi^4 - \delta\epsilon K(\epsilon_{ext} + \epsilon_{int})\psi \tag{4.1}$$

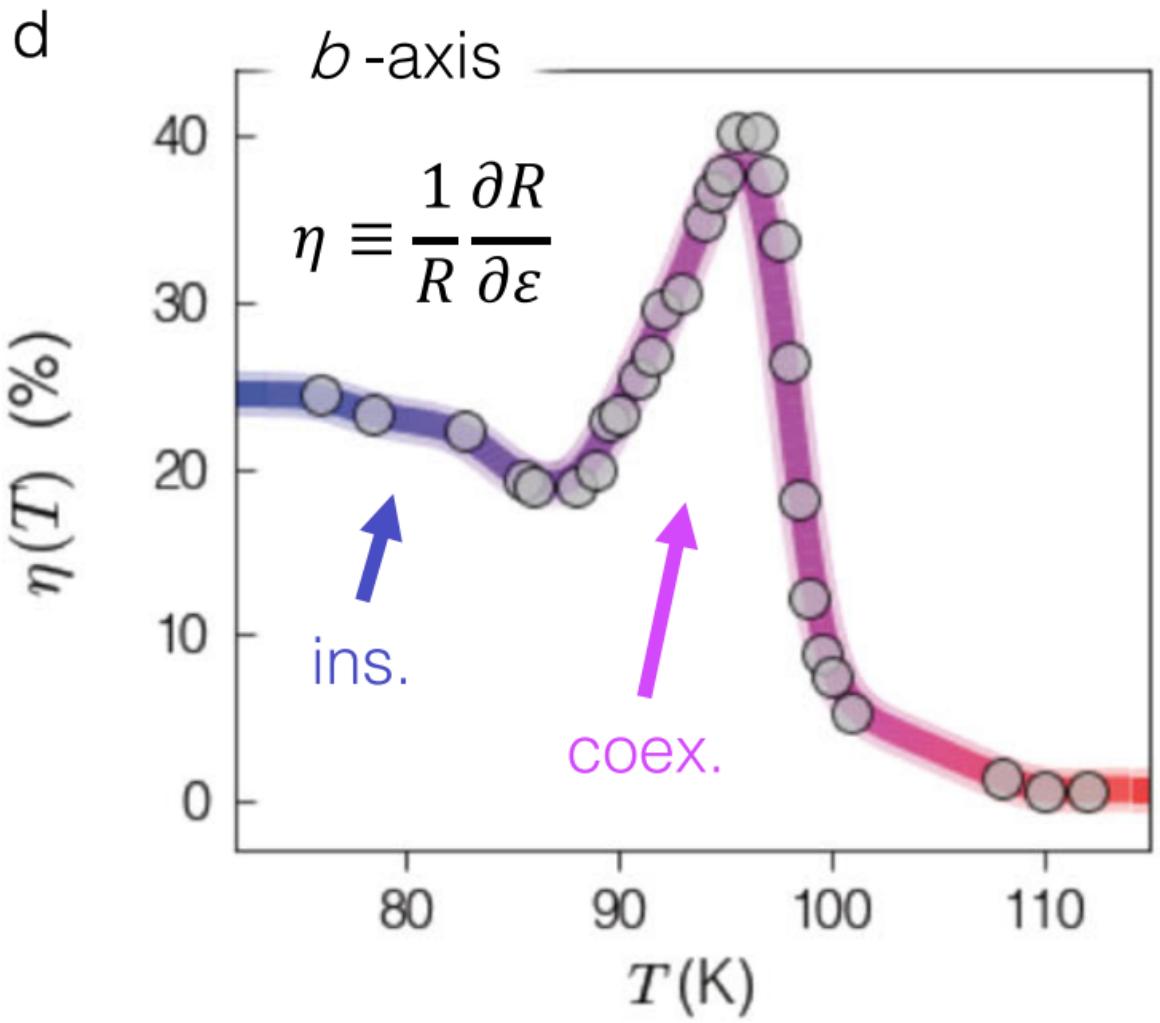

Figure 4.16: An anomalous peak in elastosusceptibility η emerges in the phase coexistence regime of the thermal transition; gray markers indicate experimental data whereas the colored curve is a guide to the eye; ins. and coex. respectively indicate insulating and phase coexistent temperature regimes.

Here κ denotes a stiffness energy per unit area of insulator-metal "domain boundaries", T^0_{IMT} denotes the "unstrained" IMT temperature, and quantities α, β, and γ are energetic constants. Meanwhile, $\delta\epsilon$ is the b-axis dilatory component of the 2nd rank spontaneous strain tensor ($\delta\epsilon$, nonzero only for c- and b-axis components), K is a b-axis elastic stiffness constant of the crystal, and we have split the b-axis uniaxial strain $\epsilon = \epsilon_{ext} + \epsilon_{int}$ into a spatially homogeneous external part ϵ_{ext} (viz. applied by our strain stage) and an internal inhomogeneous part ϵ_{int} arising from accommodation strain between coexistent S- and L-domains; the latter is determined self consistently from the real-space domain distribution of ψ (see SI). By properly encapsulating the essential competition of domain wall and elastic accommodation energies, similar Landau models have shown success in describing nano-imaging results of periodic domain textures in a variety of strain-coupled first-order transitions of complex ox-

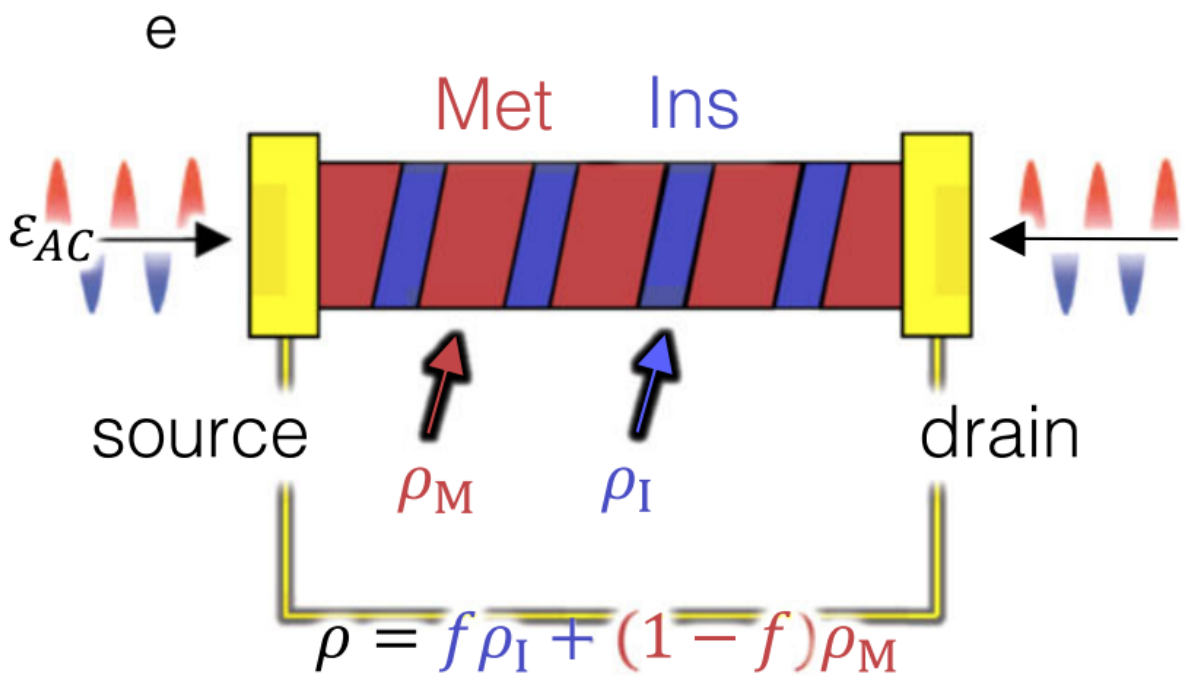

Figure 4.17: A simple circuit model allows to predict η based on the elastic susceptibility inferred from 4.14 for the same insulator-metal mixture observed by nano-IR imaging (see text).

ide thin films [104, 18], as well as single crystals [113], including the related Ca_2RuO_4 [129]. In particular, the interplay of κ and α determines the width l_{DW} of domains walls, less than 100 nm according to our observations (Fig. 4.7.1), whereas the microns-scale periodicity of insulator-metal stripes follows essentially from K and κ.

Accordingly, we first used Eq. 4.1 to describe a surficial "slab" of our crystal undergoing the IMT without external strain ($\epsilon_{ext} = 0$), and in a periodic area of the crystal ab-plane we numerically minimized the integrated free energy to obtain real-space evolution of versus temperature (free parameters chosen only to establish the domain lattice periodicity; see the Supplement for details). Fig. 4.12 presents in false color (identifying insulator and metal) across a line parallel to the simulation b-axis, demonstrating nucleation, growth, and evolution of the obtained quasi-1-dimensional domain lattice across the IMT; here T_c denotes the temperature at which L and S become equal-energy phases and the range spans their metastability. The left panel of Fig. 4.15 presents the computed temperature-dependent metallic phase fraction (red) and simulated thermal susceptibility (orange) for comparison against our measurements in Fig. 4.14, showing a remarkable reproduction of the observed three-fold thermal susceptibility. Although quadratic coupling of to T is technically distinct from its linear coupling to ext as predicted by this coelastic theory, we nevertheless regard ϵ_{ext} as a "forcing" term capable of modulating the temperature T_{IMT} below which the L-phase destabilizes, in accord with Fig. 4.9. Therefore, repeating the same simulation with ϵ_{ext} =+1% and -1% further suppresses or stabilizes the metallic phase according to expectation, rendering new phase fractions $f^+(T)$ and $f^-(T)$ (lower and upper dashed red curves in left panel of Fig. 4b). Their difference provides a measure $\chi_{el} \propto (f^- - f^+)/\Delta\epsilon$ of the elastic domain susceptibility (dashed orange curve), also bearing an uncanny resemblance to the three-fold structure of χ_{th}. We can rationalize the resemblance of χ_{el}, χ_{th} under examination of Eq. 4.1, where the effect of $\epsilon_{ext} < 0$ (>0) is to energetically (dis)favor the metallic phase. A mean-field treatment quantifies the associated shift transition temperature as $T_{IMT} = T^0_{IMT}\pm$, with $\sim K_{ext}/\psi$ and ψ our order parameter's areal average.

Though our numerical results affirm that Eq. 4.1 accounts for the physics underlying unexpected structures observed in these susceptibilities, further explanation demands an analytic treatment of the elastic energy landscape. Recognizing the unique quasi-1-dimensional behavior of phase separation here reported in this crystal, we employ a variational minimization to a simplified 1-dimensional form of Eq. 4.1 to explore the analytically deduced T-dependent phase fraction and thermal susceptibility presented in Fig. 4.15. In this model, susceptibility peaks near $f \approx 0$, 1 associate first with the energy barrier of forming L- or S-phase stripes with a minimum size exceeding l_{DW}, followed abruptly by energetically favored formation of a coherent -periodic stripe lattice. A spatially inhomogeneous energy landscape (viz. T^0_{IMT}) suffices to broaden χ_{el}, χ_{th} associated with this abrupt transition. On the other hand, the central susceptibility peak originates from a strong predisposition of the domain lattice towards $f \sim 1/2$, where strain fields of mismatching but energetically equal surficial L- and S-phase domains can be best accommodated by the bulk of the crystal without fracture. The central susceptibility peak affords therefore a "sensor" for the $f \sim 1/2$ condition of equal-energy phases forming a symmetric stripe lattice. Moreover, we propose the detailed shape of this peak in Figs. 4a-b could provide experimental access to the T-dependent electronic energy difference EL,S(T) between competing metastable phases. In particular, the thermal symmetry of this peak in Fig. 4.14 suggests an underlying linear $\psi - T$ coupling in common with the simple model treated in Fig. 4.15(right panel) and also theoretically motivated for the related Mott insulator $Ca2RuO4$ [101]. This feature differs noticeably from the asymmetric peak in Fig. 4.15 (left panel) following from the "conventional" double-well energy (Eq. 4.1) assumed by many first-order Landau theories. However, we note the experimentally inferred (Fig. 1) but indirectly resolved three-dimensional structure of domains comprising the lattice texture may also play a detailed role.

4.9.1 Mathematical treatment of the Landau theory of strain-coupled IMT

In the sections above we treat the problem of phase evolution in a strain-coupled insulator-metal transition using a quasi-one-dimensional variational model that provides an analytic understanding of thermal and elastic domain susceptibilities in CTRO. In this treatment, we consider a surficial layer of coexisting insulator and metal domains of depth d with translational invariance along the crystal [100] axis, and denote by x the position coordinate parallel to [010].

For simplicity we substitute the Landau free energy density articulated in Eq. 1 4.1 by the following F_{var} per unit volume in the thickness d:

$$F_{var}(\psi) = \frac{1}{2}\kappa|\nabla\psi|^2 + F_0\left(g(T)\psi - \frac{1}{2}\psi^2 + \frac{1}{2}\psi^4\right) - \delta\epsilon\ K(\epsilon_{ext} + \epsilon_{int})\psi \tag{4.2}$$

with $g(T) \propto (T - T_c)/\Delta T$ a surrogate measure of temperature, and other definitions given above. The first two terms describe the electronic energy density $F_{elec}(\psi)$ and the last is the elastic energy density $F_{elas}(\psi)$. Given the linear coupling of T and ψ in this treatment, the elastic domain susceptibility χ_{el} is manifestly proportional to the thermal one χ_{th}. Meanwhile, we determined χ_{th} as presented in Fig. 4.15 from the temperature-dependent metallic phase fraction $f(T)$ estimated by a variational form for $\psi(x)$ through which we minimize Þ through which we minimize Eq. 4.2:

$$\begin{aligned} \psi(x) &= \psi_M + \frac{1}{2}\Delta_{I,M}\sum_n \phi(x - n\lambda) \ \text{ with} \\ \phi(x) &= \tanh((x - f\lambda)/l_{dw}) - \tanh(x/l_{dw}) \end{aligned} \tag{4.3}$$

Guided by our nano-imaging results, this form describes a onedimensional lattice of piecewise insulator and metal ($\psi = \psi_{I,M}$) domains separated by domain walls of size l_{dw} and with overall periodicity λ; the metallic phase fraction f is manifestly represented. Including the energy of pairwise domain walls, the electronic energy density $F_{el,\lambda}$ per unit period of

this lattice is approximately:

$$F_{elec,\lambda} \approx \frac{\kappa}{2l_{dw}}\nabla\psi_{I,M}^2 + \lambda\left[(1-f)F_{elec}(\psi_i) + fF_{elec}(\psi_M) + l_{dw}/\lambda\Delta F\right] \tag{4.4}$$

where ΔF denotes height of the electronic energy barrier between insulator and metal phases pursuant to Eq. 4.2, and $l_{dw} \approx \frac{1}{2}\psi_{I,M}\sqrt{\kappa/\Delta F}$ can be asserted from the Landau theory of soliton domain walls[132]. Lastly, setting $\epsilon_{ext} = 0$ for the equilibrium configuration, the elastic energy density per unit volume can be expressed as

$$F_{elas}(\lambda) = -d\frac{\delta a^2}{2}\int_{-\infty}^{\infty} dx\partial_x\psi(x)G_{xx}(x-x')\partial_{'}\psi(x') \tag{4.5}$$

where $\delta\sigma \equiv K\delta\epsilon$ is the b-axis dilatory component of spontaneous stress associated with the insulator-metal transition, and G_{xx} is an elastic Green's function which for $\lambda > d$ we approximate [104, 129] by:

$$G_{\vec{r}} \approx \frac{1+\nu}{\pi E}\left(\frac{1-\nu}{r} + \nu\frac{x^2}{r^3}\right) \text{ with} r = \sqrt{x^2+y^2} \tag{4.6}$$

Here $\nu \approx 0.3$ and E are Poisson's ratio and Young's modulus for CTRO, respectively, which we approximate using values reoprted for the analogous ruthenate Sr_2RuO_4 [133]. Equation 4.5 was evaluated by semi-analytic methods fo our variational form $\phi(x)$. Taken together equations 4.5, 4.4, 4.6 are sufficient to numerically determine the temperature-dependent metallic phase fraction $f(T, \lambda/d)$ that minimizes equation 4.2, from which we deduce χ_{th} predicted in Fig 4.15.

4.10 Bulk elastosusceptibility of CTRO

Our findings by scanning nano-susceptibility imaging demonstrate that, while external strain can deterministically modulate the macroscopic Mott transition in this prototypic 4d-metal oxide, implicit accommodation strain of coexisting phases plays an equally important

role for governing both i) their real-space texture and ii) the elastic response of the resulting domain lattice – a property we denote "domain susceptibility." In fact, even the macroscopic susceptibility of this Mott insulator to uniaxial strain shows hallmarks of these phenomena.

Fig. 4.16 presents bulk elastoresistance measurements along the b-axis of a CTRO crystal similar to that explored in Figs. **??** and 4.14 ; here the elastoresistance $\eta = R^{-1}/\partial\epsilon$ records relative changes in crystal resistance under uniaxial strain, a metric previously applied to measure "divergent" nematic susceptibilities across continuous phase transitions[5]. In that context, an observed peak in at $T \approx 95$K through our first-order transition may come as a surprise until reconciled with our SNSImaging results.

Envisioning our phase-coexistent crystal as a quasi-one-dimensional network of metal and insulator domains (Fig. 4d) with respective resistivities ρ_M, ρ_I, the overall b-axis resistivity $\rho = f\rho_I - (1-f)\rho_M$ will show a response ρ_{AC} to an oscillating uniaxial strain ϵ_{AC} related to η by

$$\rho\eta = \frac{\rho_{AC}}{\epsilon_{AC}} \propto \chi_{elas}(\rho_I - \rho_M) + f\delta_\epsilon\rho_I + (1-f)\delta_\epsilon\rho_M \tag{4.7}$$

In case when $\rho_I \gg$ we may approximate η by

$$\eta \approx \eta_{coex} + f\eta_l + (1-f)\eta_M \tag{4.8}$$

with elastoresistances for the end-phase defined by

$$\eta_{I,M} \equiv \frac{\partial\rho_{I,M}}{\partial\epsilon} \tag{4.9}$$

Crucially, this framework predicts an emergent positive elastoresistence coex associated solely with the onset of phase coexistence and its consequent elastic domain susceptibility given by $\eta_{coex} \equiv \chi_{elas}/f$. To generate a simple qualitative model for the data recorded in Fig. 4.16, we apply our inferences for $f(T)$ and χ_{elas} from Fig. 4.14 4a, together with $\eta_{I,M}$ discernible from the end-phase values of η, resulting in the characteristic line-shape shown

in Fig. 4.17. This model predicts an obvious asymmetric peak in elastoresistance upon formation of the stripe domain lattice below T=95 K, in remarkable accord with our measurements of a similar crystal in Fig. 4.16. The agreement only falters in the thermal width of the elastoresistance peak; however, this is easily reconciled by considering that our nano-imaging results in Fig. 4.12 resolve only a narrow portion of the crystal, whereas T_{IMT} may vary throughout the crystal by 5 K or more, easily accounting for the comparative thermal breadth of the elastoresistive response. Therefore, these findings demonstrate elastoresistance as a useful macroscopic reporter of phase coexistence across first-order transitions in which the constituent electronic phases are coupled to strain, as in the Mott insulator $Ca_3(Ru_{1-x}Ti_x)_2O_7$.

Moreover, we interpret the absence of any detectible peak in a-axis elastoresistance measured across this insulator-metal transition with the vanishing elastic susceptibility of the stripe domain lattice parallel to the underlying L- and S-phase domains (see Chapter 4 for a detailed discussion). We, therefore, envision orientation-resolved elastoresistance as a promising probe of domain morphologies amidst phase coexistence in systems (and internal volumes) not otherwise directly addressable by nanoprobes like SNSImaging. These correlative techniques thus provide useful complementarity.

4.11 Conclusion

We have demonstrated that the Mott insulator-transition in single crystals of CTRO provides an uncommonly pristine platform to resolve the intrinsic response of self-organized domain textures to external stimuli like strain and temperature. Complemented by bulk uniaxial elastoresistance measurements, our low-temperature scanning nano-susceptibility imaging provides real-space access to strain-tuned domain textures evolving across the insulatormetal transition of this Mott crystal. Our nano-scale elastic probe should prove versatile for tracking phase-change susceptibilities with unprecedented spatial resolution in other correlated 4d and 5d transition metal oxides, and in correlated electron solids more broadly.

For instance, the yet-mysterious electrical switching characteristics common to both Sr_2IrO_4 and Ca_2RuO_4 are reportedly tied to bias-controlled octahedral tilts [134, 135], and nanoIR imaging under simultaneous and correlative control of applied bias and uniaxial strain can evaluate this connection in real-space.

In addition, owing to stronger spin-orbit coupling in 5d transition metal oxides compared with their 4d cousins, the resulting smaller Mott gaps in systems like $Sr_3Ir_2O_7$ show exotic insulating and metallic phases strongly tunable through pressure [136] with, we infer, remarkable real-space implications to resolve under applied uniaxial strain. However, we note that our strain-modulated technique is presently reliable only for samples of flat aspect ratio with uniform crystallinity and identifiable crystal orientation, somewhat constraining the eligibility of material systems for study. On the other hand, the high spatial resolution of infrared nano-imaging could foreseeably enable simultaneously straining and imaging uniform crystals as small as a few microns. In fact, suitable modifications to our strain device together with sample micro-manipulation could afford strain-modulated imaging of selected few-microns slices of single crystals, as isolated e.g. by focused ion beam milling.

Returning attention to our bilayer ruthenate, unexplored dimensions of the insulator-metal transition should be pursued by strain-modulated nano-imaging. Although we carried out these strain-modulated SNSImaging investigations on un-twinned CTRO crystals, the IMT in this system is also uncommon for its coupling to four-fold symmetry-breaking orthorhombic distortion. Owing to the bilayer unit cell, this ferroelastic distortion entails a polar moment oriented along the orthorhombic b-axis, rendering a hybrid-improper ferroelectric Mott insulator or high temperature "polar metal" [125, 126, 137]. Its real-space implications for the IMT have hitherto gone completely unaddressed. We envision strain-modulated nano-imaging of insulator-metal domains near ferroelastic boundaries of twinned crystals, and whose manipulation might enable on-demand local re-orientation of striped domains, thus affording multi-functional control over this Mott nanotexture.

Chapter 5: Probing anisotropy across the thermal IMT in $Ca_3(Ru_{1-x}Ti_x)_2O_7$

5.1 Resistive anisotropy

The first order character of the transition manifests itself in the appearance of phase coexistence through the transition. The spatial patterns of phase coexistence that arise in $Ca_3(Ru_{0.9}Ti_{0.1})_2O_7$ samples have been studied with multi-messenger low-temperature infra-red and Kelvin probe nanoimaging [138] and microwave impedance spectroscopy [139]. Existence of unidirectional stripe domain patterns was revealed and the pattern was argued to be a consequence of coupling between the IMT order parameter and strain. Furthermore, the stripe patterns in question are believed to be associated with a specific (b-axis) crystal axis direction based on an energetics argument first stated in [129]. Consequently, one might expect transport properties of $Ca_3(Ru_{0.9}Ti_{0.1})O_7$ to exhibit an angle dependence depending on the direction of current flow within the ab plane of the crystal and indeed this is found experimentally (Figure 5.1).

In the simplest model of the electrical response of a $Ca_3(Ru_{0.9}Ti_{0.1})O_7$ sample undergoing an IMT we consider the sample to be a network of stripe resistors. Each strip takes on a high (insulating) or low (metallic) resistance value. The fraction of insulating stripes maps onto the phase fraction in the sample and varies continuously between 0 (a fully metallic sample) and 1 (a fully insulating sample). Within this model the $R_{bb}(R_{aa})$ component of the resistivity tensor is given by the series (parallel) resistance of the stripe resistor network of stripes of such elements where by series (parallel) resistance we mean the longitudinal resistance of the network with current oriented perpendicular (parallel) to the orientation of the stripes. If we let R^i_{aa} (R^m_{aa}) be the resistances of a fully insulating (metallic) sample on

the cusp of undergoing the phase transition and f be the metallic phase fraction then the longitudinal resistances at a given phase fraction f, $R_{bb}(f)$ and $R_{aa}(f)$ are given by

$$R_{bb}(f) = fR^m_{bb} + (1-f)R^i_{bb} \tag{5.1}$$

$$R_{aa}(f) = \left[\frac{f}{R^m_{aa}} + \frac{(1-f)}{R^i_{aa}}\right]^{-1} \tag{5.2}$$

We notice that the phase fraction f is in one-to-one correspondence with R_{bb} and therefore its temperature dependence can be extracted from R_{bb}. A test of the veracity of this model is whether the temperature dependence of R_{aa} resulting from the phase fraction derived from R_{bb} and our formula matches the experimental R_{aa} curve. Upon inspection of figure **??** we see that there is a broad match. In particular, the R_{aa} curve is substantially steeper on the insulating side and flatter on the metallic side in concurrence with experiment. A precise match is not to be expected as the shape of the transition curve is liable to be affected by a gamut of sample-specific factors including the variation in local disorder within a crystal. We nonetheless suggest that this simple model accounts for the reentrant transport anisotropy in the temperature range of the IMT in this material.

5.2 Elastosusceptibility of Ca3Ru2O7

5.2.1 Overview

Following [5] we define the elastosusceptibility as as the susceptibility of fractional resistance $\eta = R/R_0$ with respect to strain, ϵ:

$$\chi = \frac{1}{\rho}\frac{d\rho}{d\epsilon} \tag{5.3}$$

While this a tensorial quantity with respect to the orientations of strain, current and voltage, in this work we restrict ourselves to situations where these three quantities are locked together

in parallel, i.e. the purely longitudinal components. In general, the elastosusceptiblity is a quantity of particular interest when it can be connected to the order parameter of a phase transition. In the aforesaid cases one may use the elastosusceptiblity to track the evolution of the order parameter across phase boundaries and the goal of this section is to accomplish this in the case of

A novel aspect of the elastosusceptibility measurement in $Ca_3(Ru_{0.9}Ti_{0.1})O_7$ is that the quantity accessed by experiment is an average susceptibility of a spatially ordered phase

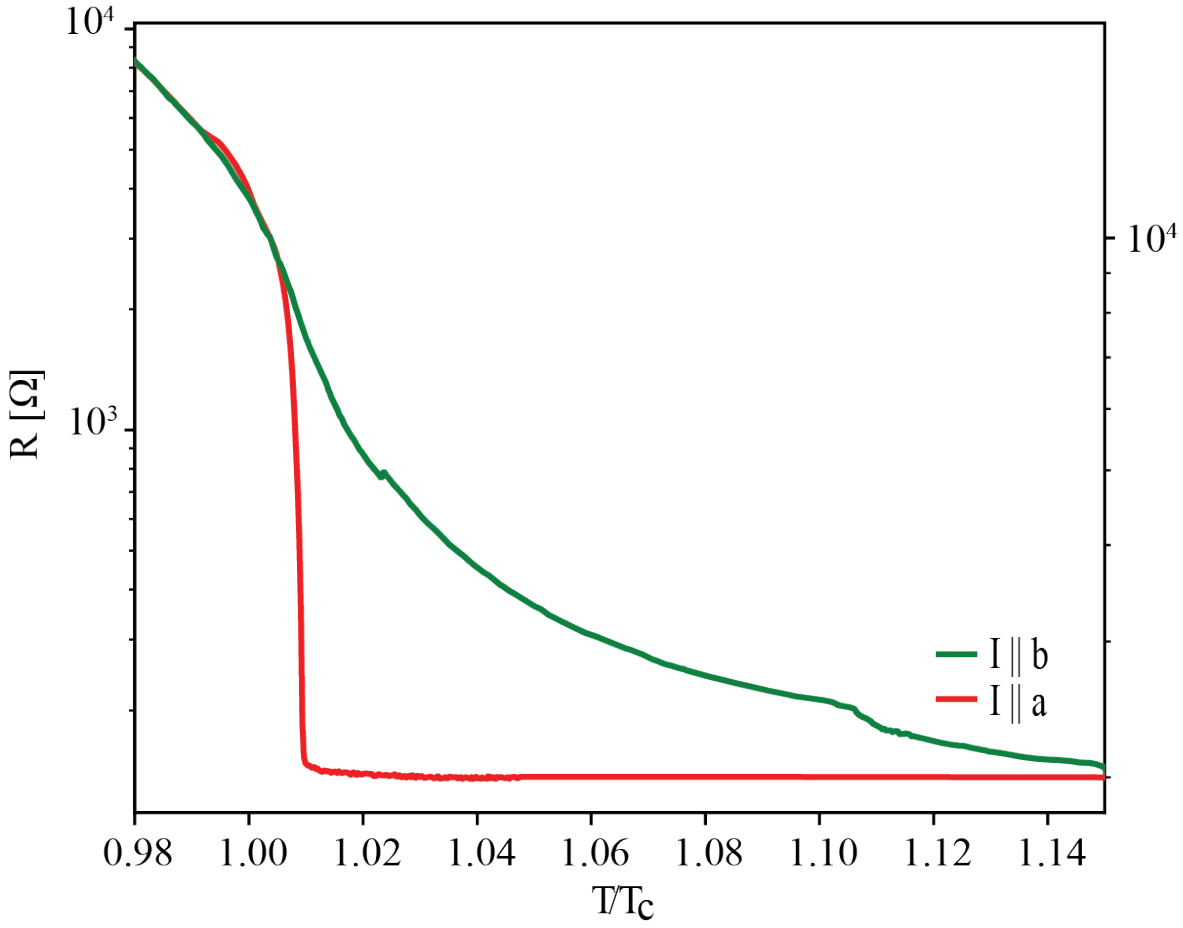

Figure 5.1: Experimental measurement of R_{aa} and R_{bb} of $Ca_3(Ru_{0.9}Ti_{0.1})O_7$ as function of temperature in units of the transition temperature T_c. For current oriented along the b-axis, the striped phase texture is parallel to the current flow and consequently the resistance tracks the overall phase fraction weighed by the resistances of the insulating and metallic phases. For current oriented along the a-axis, the stripe phase texture is perpendicular to the current flow resulting in a more complicated relationship between phase fraction f and resistance.

mixture. To wit, the longitudinal elastosusceptibilities are:

$$\chi_b = \frac{1}{R_{bb}} \left[f \frac{\partial R^i_{bb}}{\partial \epsilon_b} + (1-f) \frac{\partial R^m_{bb}}{\partial \epsilon_b} + (R^i_{bb} - R^m_{bb}) \frac{\partial f}{\partial \epsilon_b} \right]$$

$$\chi_a = R_{aa} \left[\frac{f}{{R^i_{aa}}^2} \frac{\partial R^i_{aa}}{\partial \epsilon_a} + \frac{(1-f)}{{R^m_{aa}}^2} \frac{\partial R^m_{bb}}{\partial \epsilon_b} + (\frac{1}{R^i_{bb}} - \frac{1}{R^m_{bb}}) \frac{\partial f}{\partial \epsilon_b} \right]$$

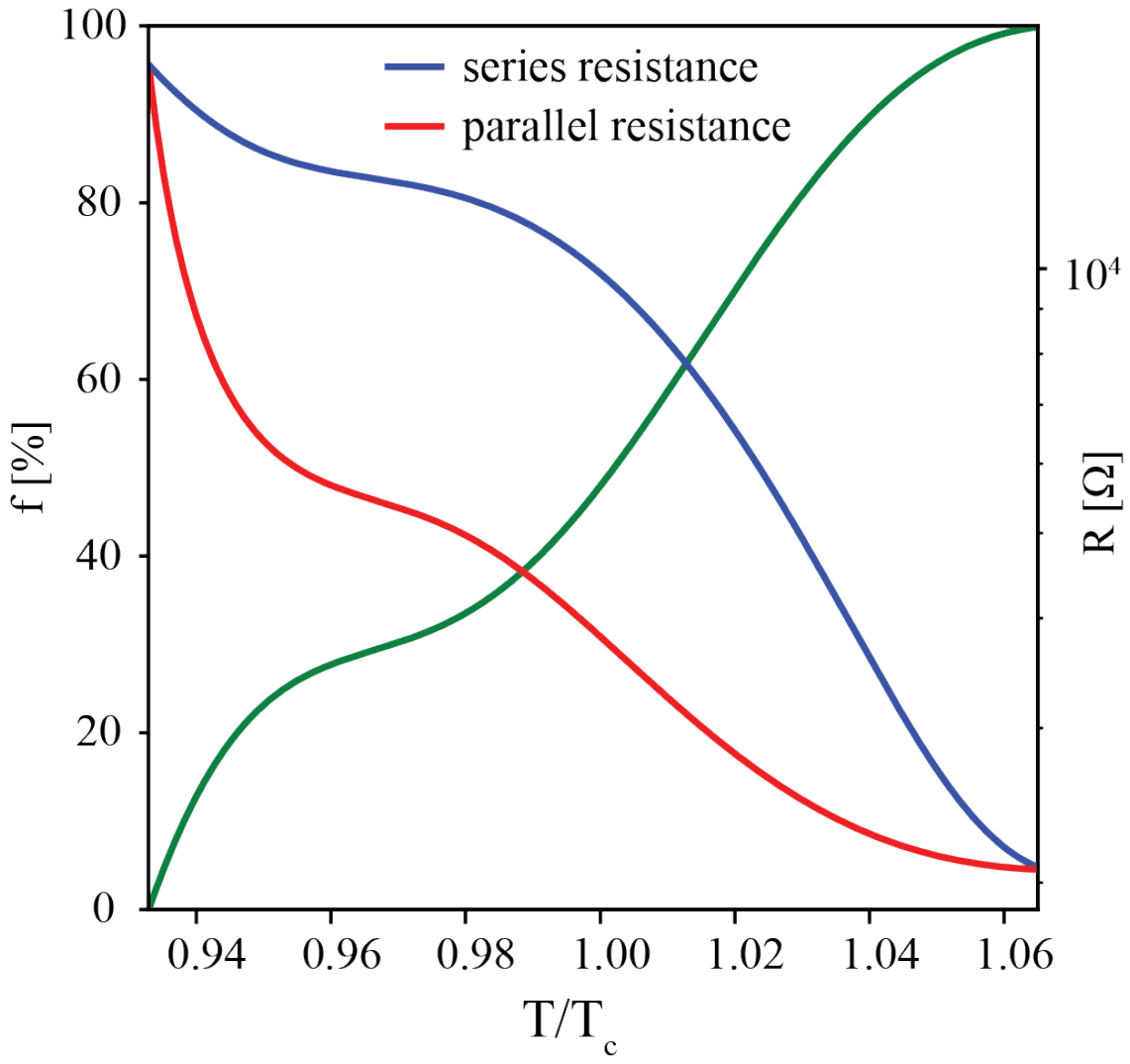

Figure 5.2: The green curve shows the temperature dependence of the metallic phase fraction f obtained through a temperature-dependent near-field scanning nanoimaging experiment. The blue line shows the theoretical temperature dependence of the series, b-axis (a-axis), resistance computed from a series (parallel) resistor network model.

To model these quantities we need to get a handle on three susceptibilities: the homogeneous phase susceptibility in the insulating ($R^i_{bb}{}^{-1}\partial R^i_{bb}/\partial\epsilon_b$) and metallic ($R^m_{bb}{}^{-1}\partial R^m_{bb}/\partial\epsilon_b$) phases, and the strain susceptibility of the composition of the phase mixture ($\partial f/\partial\epsilon_b$).

5.2.2 Experimental Results

Before launching into the theoretical analysis let us study the experimental results presented in panels a and b of figure 2. Panel 2a (2b) presents elastosusceptibility data with strain, current and voltage directed along the b and a crystallographic axes. In the upper right corner are cartoon pictures of the measurement geometry used to obtain the results in the figure. The main panel of 2a displays the response of resistance to small ($< 0.1\%$) strains for strain/current/voltage oriented along the b-axis. The reader should note the linearity establishing the validity of a theoretical analysis that uses a linear response approach as we do below. As a matter of curiosity, reader should also note the absolute magnitude of the susceptibility is numerically comparable in magnitude with the strongest such response we are aware of in [5]: this is a large effect. The inset in the lower left corner of the panel shows the temperature dependence of the susceptiblity across the thermal insulator-to-metal transition. Panel 2b shows the temperature dependence of the susceptiblity for strain/current/voltage oriented along the a-axis, with a cartoon picture of the measurement geometry presented in the upper right hand corner.

We would like to explain the following observations which follow form these data. Firstly, there is clear difference in magnitude of the elastosusceptibility between homogeneous phase susceptibility in the insulating and metallic phases for both orientations of strain/current/voltage. Secondly, there is an anisotropy in those values between the a and b axes and we want to understand the origin of that. Thirdly, the reader should note that the absolute sign of the strain response is opposite between the a and b axes. Concretely, this means that if one takes a sample in the insulating phase uniaxial compression along the b axis increases the resistance whereas uniaxial compression along the a axis reduces the resistance. Finally, for

strain/current/voltage oriented along b principal axis there is a relatively broad peak in the susceptibility associated with the phase coexistence sector of the phase diagram but no such peak is observed for strain/current/voltage oriented along the a principal axis. The origin of that peak was explained in McLeod et al. and here we would like to understand the origin of the anisotropy in the elastosusceptibility response within the transition sector of the phase diagram.

5.2.3 Phenomenological models

We begin by discussing the elastosusceptibility of the homogeneous phases. In the insulating phase the resistivity is due to thermally activated carriers and its temperature dependence follows an Arrhenius law:

$$\rho = A \exp \frac{\Delta}{T} \tag{5.4}$$

ergo the elastoresistivity at a fixed temperature T is given by

$$\frac{1}{\rho}\frac{d\rho}{d\epsilon} = -\frac{1}{T}\frac{d\Delta}{d\epsilon} \tag{5.5}$$

To proceed further we introduce the order parameter for the transition as established in [101], the orbital disproportionation $\eta = \eta_{xy} - \frac{1}{2}(\eta_{yz} + \eta_{xz})$. We assume on phenomenological grounds that the band gap is proportional to the order parameter such that

$$\frac{1}{\rho}\frac{d\rho}{d\epsilon} = \frac{\Delta_0}{T}\frac{\partial\eta}{\partial\epsilon} \tag{5.6}$$

where $\Delta_0 = \frac{\partial\Delta}{\partial\eta}$. Since in the insulating phase $\eta \sim 1$, Δ_0 is on the order of the energy gap which is much bigger (circa 100meV) than the transition temperature ($\sim$ 10meV).

In the homogeneous metallic phase we may assume that the conductivity is proportional to the density of states at the Fermi level, $N(E_f)$, which implies that the resistivity $\rho \sim \frac{1}{N(E_f)}$.

Linearizing with respect to the order parameter we have

$$\frac{1}{N(E_f)} = \frac{1}{N_0} - \frac{1}{N_0^2}\frac{N(E_f)}{\partial\eta}\delta\eta \tag{5.7}$$

and correspondingly the elastosusceptibility in the metallic phase is

$$\frac{1}{\rho}\frac{d\rho}{d\epsilon} = \frac{1}{N_0}\frac{\partial N_0}{\partial\eta}\frac{\partial\eta}{\partial\epsilon} \tag{5.8}$$

We see that in both the insulating and the metallic phase the elastosusceptibility is proportional to the susceptibility of the order parameter $\partial\eta/\partial\epsilon$. We will discuss how to estimate that quantity momentarily but we point out now that the mathematical source of the difference between the susceptibility is that $\frac{\Delta_0}{T} \gg \frac{\partial N_0}{N_0\partial\eta}$.

5.2.4 Microscopic models

[140] have studied in detail the effect of titanium doping on the electronic structure of Ca3Ru2O7. Here we follow the treatment in [141] to extend this approach to model elastosusceptibility in the temperature range that corresponds to the IMT in $Ca_3(Ru_{0.9}Ti_{0.1})_2O_7$.

To model the elastosuceptiblity we will employ a generalization of the free energy formalism developed in [101]. The total free energy of the system is:

$$\begin{aligned} F_{tot} = F_{ele}(\eta) + \eta(\Delta - kt) + F_{GAFM}(m^2) + \\ \eta\mathcal{F}\cdot\delta\vec{Q} - \lambda_m m^2\eta + F_{ela}(\delta\vec{Q}) \end{aligned} \tag{5.9}$$

where F_{ele} is the electronic component, F_{ela} is the elastic component which depends on the phonon order parameter $\delta\vec{Q}$, F_{GAFM} is the energy associated with magnetic ordering which depends on the magnetic order parameter, the staggered magnetization $m = \sum_{\vec{R}_i} m_i^{i\vec{k}\cdot\vec{R}_i}$ where R_i is the site coordinate of the ith Ru atom and $\vec{k} = (\pi,\pi,\pi)$, $\Delta = (\epsilon_{yz} + \epsilon_{xz})/2 - \epsilon_{xz}$ is the orbital split and t is the orbital dimerization strength. DFT+U and DMFT calculations show

that the electronic order parameter η is close to 0 in the metallic phase, hence a single-well approximation is appropriate for the electronic part of the free energy:

$$F_{ele}(\eta) = \frac{1}{2}\chi^{-1}\eta^2 \tag{5.10}$$

where χ_η is the electronic susceptibility of the order parameter. To susceptibility χ and electronic magnetic coupling will be estimated from a multiple linear regression fitting of the order parameter change $\delta\eta$ against the relevant variables Δ, t and m^2. The form of the model is

$$\delta\eta = \chi(\delta\Delta - k\delta t + \lambda(m^2)) \tag{5.11}$$

Concretely we begin with the 40K experimental structure [114] and construct three groups of linearly independent structures through three sets of transformations: c-axis extension, epitaxial (ab plane) strain and volumetric distortions. For each structure we conduct DFT+U calculations with multiple U values from 0.1eV to 3.0eV and initial magnetic structure set to be the GAFM phase; we then fit the converged structure with MLFW via the wannier90 package to compute the orbitally-resolved occupancy, the orbital splitting, the hopping strength and the magnetization per octahedron. Finally we fit the multiple linear regression model for $\delta\eta$. We use regression coefficients to determine the coupling strengths k, λ_m and the susceptibility χ. Upon performing the fits we find that magnetisation for a fixed U forms a plane in the $\Delta - t$ parameter space with linear-in-δU separation along the U parameter axis, thus validating the linear model assumption. The linear model we obtain in this fashion is

$$\begin{aligned} \delta\eta &= 5.66(\delta\Delta) - 3.10(\delta t) + 0.20(\delta m^2) \\ \delta m^2 &= 10.73(\delta\Delta) - 15.1(\delta t) + 0.68(\delta U) \end{aligned} \tag{5.12}$$

Returning to the strain susceptibility of the order parameter, we find that there is an addi-

tional source term due to strain susceptiblity of the magnetisation:

$$\frac{\partial \eta}{\partial \epsilon} = \frac{\partial \eta}{\partial \Delta}\frac{\partial \Delta}{\partial \epsilon} + \frac{\partial \eta}{\partial t}\frac{\partial t}{\partial \epsilon} \tag{5.13}$$

Since the solutions for the insulating and metallic phases lie close to each other in parameter space we assume that the strain susceptibility of the orbital splitting and the dimerization strength on external strain are the same in the both phases. In the paramagnetic phase we have:

$$\frac{\partial \eta}{\partial \Delta} = \chi_M = 5.66; \quad \frac{\partial \eta}{\partial t} = -3.10 \tag{5.14}$$

whereas in the magnetic phase

$$\frac{\eta}{\Delta} = \chi_M + \lambda_m \chi_M \frac{\partial m^2}{\partial \Delta} = 5.66 + 2.15 = 7.81 \tag{5.15}$$

$$\frac{\partial \eta}{\partial t} = -\chi * k + \lambda_m \chi_M \frac{\partial m^2}{\partial t} = -6.12 \tag{5.16}$$

Figure 5.13 in [141] shows the response of the orbital splitting and dimerization strength to uniaxial strain. A salient feature of these calculations is the drastic difference between the effect of uniaxial strain along the a and b crystallographic axes. To obtain these numerical data we employed the same procedure as earlier in this section. We use DFT+U relaxation methods as before, but this time with a or b unit cell coordinate fixed and the remaining coordinates relaxed; followed by static DFT+MLWF calculations to determine the orbital splitting and dimerization strength. We see from the left hand panel of figure 5.13 in [141] both that the b axis has a much stronger influence on the orbital splitting and also that its influence is opposite in sign to that of a-axis strain. We see from the right hand panel of that figure that the dimerization strength is enhanced with the same gradient by strain along either a or b directions. The physical reason for this is that both a and b tensile (compressive) strain induce a contraction (extension) of the c axis which in turn enhances

(reduces) the hopping integral along the vertical direction. Performing linear regression on these numerical data we find

$$\frac{\partial \eta}{\partial \epsilon_a} \approx -0.15eV, \quad \frac{\partial \Delta}{\partial \epsilon_b} \approx -0.9905eV, \tag{5.17}$$

and

$$\frac{\partial t}{\partial \epsilon_a} \approx \frac{\partial t}{\partial \epsilon_b} \approx 0.1eV \tag{5.18}$$

Using equation (5.13) we find

$$\begin{aligned} \left.\frac{\partial \eta}{\partial \epsilon_a}\right|_M &= 5.66 * (-0.15) - 3.1 * 0.1 = -1.16 \\ \left.\frac{\partial \eta}{\partial \epsilon_a}\right|_I &= 7.81 * (-0.15) - 6.12 * 0.1 = -1.78 \end{aligned} \tag{5.19}$$

$$\begin{aligned} \left.\frac{\partial \eta}{\partial \epsilon_b}\right|_M &= 5.66 * 0.99 - 3.1 * 0.1 = 5.29 \\ \left.\frac{\partial \eta}{\partial \epsilon_b}\right|_I &= 7.81 * 0.99 - 6.12 * 0.1 = 7.12 \end{aligned} \tag{5.20}$$

5.2.5 Comparison of models and experiments

One key prediction of the theoretical model presented here concerns the signs of elastosusceptiblity responses: they are opposite for the a and b directions. This is indeed borne out in the measurements were obtained (viz. Fig. 5.4 and 5.3). Unfortunately the presence of the prefactors in the expressions for the susceptibility means that we cannot make a quantitative comparison between the susceptiblity values and the theoretical model. Modelling those dependencies to allow for a quantiative comparison is an interesting direction for future work. Another avenue for future studies is to measure the full temperature dependence of the elastosusceptibility in these materials, from the very low temperatures where we predict that a T^{-1} temperature dependence should be observed, to the paramagnetic metallic phase at high temperatures where, presumably, other mechanisms are at play.

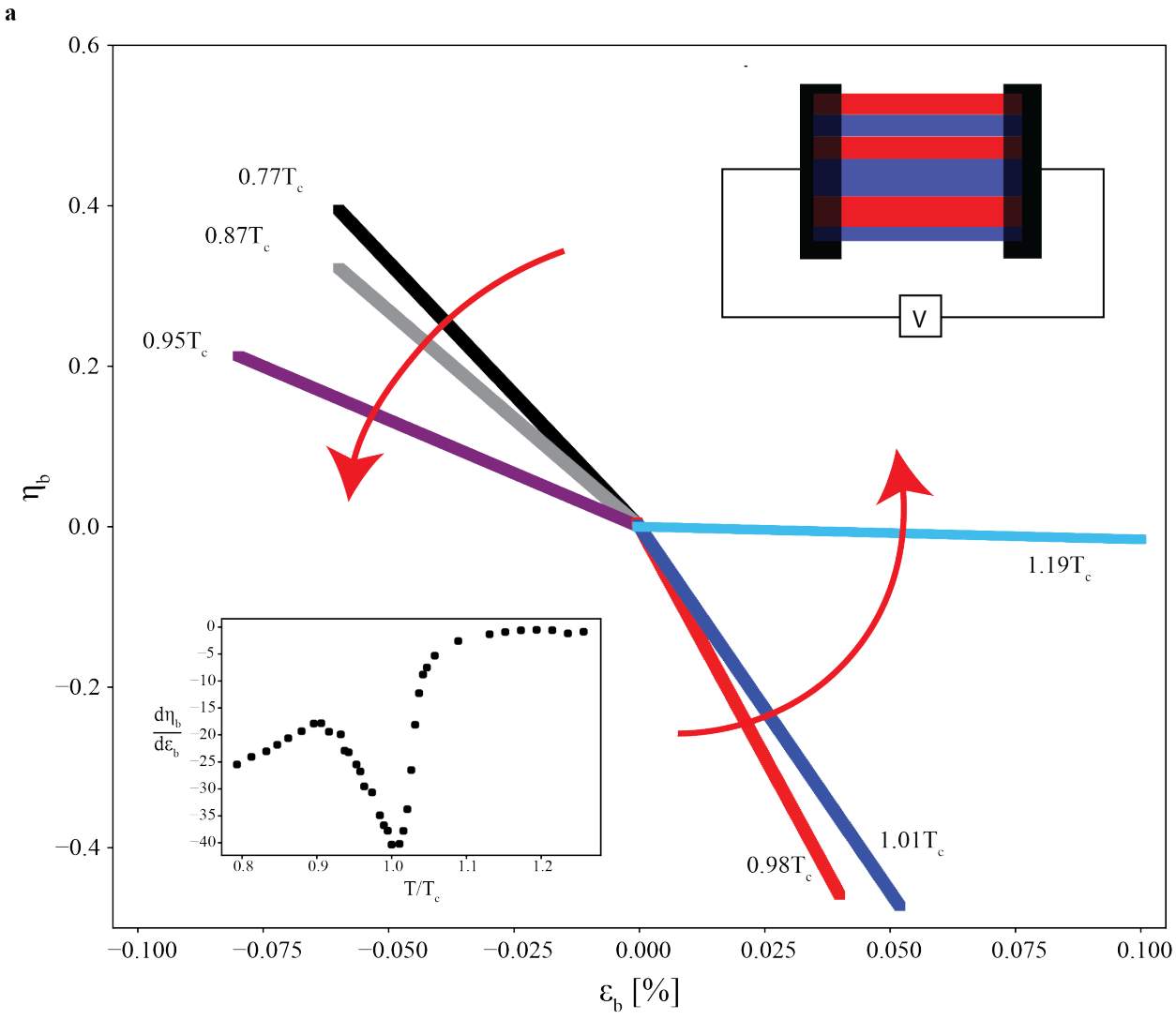

Figure 5.3: (a) Strain dependence of resistance R_{bb} on b-axis strain at fixed temperatures for 77%, 87%, 95%, 98%, 101%, 119%. The upper right hand inset shows the measurement geometry with current and strain oriented along the b-axis, parallel to the stripe orientation. The lower left hand inset is a plot of the linear slope of the dependence of R_{bb} on b-axis strain. We notice a decade-fold difference between the susceptibility in the homogeneous metal and homogeneous insulator. We also notice a large peak in the susceptibility around T_c whose origin was explained in [138].

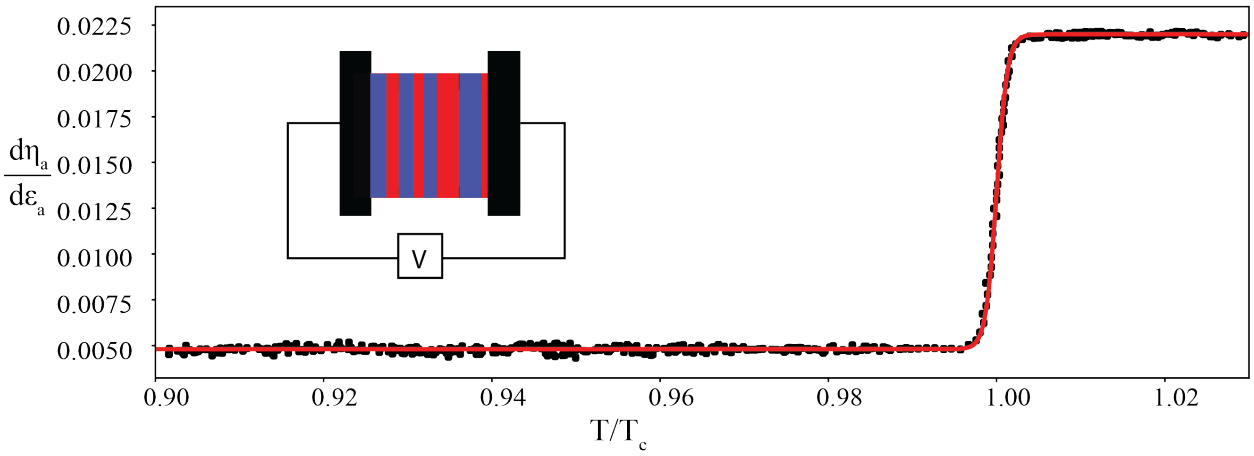

Figure 5.4: (a) Strain dependence of resistance R_{bb} on b-axis strain at fixed temperatures for 77%, 87%, 95%, 98%, 101%, 119%. The upper right hand inset shows the measurement geometry with current and strain oriented along the b-axis, parallel to the stripe orientation. The lower left hand inset is a plot of the linear slope of the dependence of R_{bb} on b-axis strain. We notice a decade-fold difference between the susceptibility in the homogeneous metal and homogeneous insulator. We also notice a large peak in the susceptibility around T_c whose origin was explained in [138].

Chapter 6: Electric-field driven metallization of $Ca_3(Ru_{1-x}Ti_x)_2O_7$

6.1 Introduction

One of the long standing goals of the field of quantum matter is to develop devices based on quantum phenomena that help to solve problems such as energy efficiency. A prime target for such studies has been the Mott transition [92]. An obvious tuning parameter in this context is hydrostatic pressure whose application often drives systems through the full gamut of many body phenomena. A drawback of using pressure, however, is the significant level of sophistication demanded by the technique. Electric field is an appealing alternative. Its ease of application constitutes its primary advantage, especially for electronics. Furthermore, an electric field controls the electronic state directly as opposed to pressure or strain which control the state indirectly via a deformation of the crystalline unit cell dimensions.

6.2 Examples of electric field-driven phenomena

6.2.1 Electrostatic field doping

Electrostatic field doping [142, 143] is an electric field control technique whereby one uses an extremely large electric field to control the density of electronic carriers on the surface of an insulator or a semiconductor. A spectacular illustration of this effect can be found in the band insulator SrTiO3 where an electric field of 20 kV/m was discovered to induce superconductivity within a surface layer of a sample[143].

More broadly, examples of applications of this technique, referred to as "gating", abound within the field of two-dimensional materials for which Columbia has been a central hub. Researchers here and elsewhere have discovered a myriad of examples of gate-controllable

phenomena, including superconductivity [144, 145], magnetism [146, 147], insulation [148, 149, 150] and charge order [151, 85, 152].

6.2.2 Electric field-driven "switching"

Another set of electric field driven phenomena are Mott transitions triggered by the application of electric field, termed "switching". Transition metal oxides have received significant attention as a potential platform to realize this idea in the practical context of electronic devices such as RAM [153, 154]. Major roadblocks to this line of research are the low temperatures that are often necessary for switching to occur and the magnitude of fields involved (typically 1-100kV/m). An instance of room temperature switching has been observed in VO_2 films [155] but the fields involved are still large. The impetus for the work described in this thesis was the discovery of a room temperature switching phenomenon in the monolayer Ruddlesen-Popper calcium ruthenate Ca_2RuO_4.

6.3 Field-driven switching in Ca_2RuO_4

The discovery of field-driven switching in Ca_2RuO_4 generated a tremendous amount of interest. While, as described above, the existence of a switching phenomenon in a Mott insulator is not in itself a surprise, the mangitude of the field needed to trigger it in Ca_2RuO_4 generated a lot of excitement, both from the perspective of practical applications and because the mysterious mechanism of the transition was an exciting fundmanetal problem for scientists to tacle.

One expects a Zener breakdown phenomenon in a gapped material at electric fields such that the voltage dropped over a lengthscale on the order of the size of a crystalline unit cell is on the order of the energy gap [156]. The estimate for that field performed in [135] goes as follows: the thermal activation gap obtained from an Arrhenius fit to the resistivity of Ca_2RuO_4 is $\approx 0.2eV$ the gap energy in CRO is $0.2eV$ determined from the activation energy based on the temperature (T) dependence of resistivity [157]. Using the in-plane

lattice spacing of $a = 5.45$ and an estimate of the bandwidth based on the related compound Sr_2RuO_4 $E_F \sim 0.2eV$, one obtains $E_{th} \sim 4$MV/cm. Experimentally, however, $E_{th} \sim 40V/cm$ is found - smaller by a few decades.

6.3.1 Voltage versus current switching

There exist two ways to trigger electric field induced switching in Ca_2RuO_4: applying a voltage (6.1) and applying a current (6.2). In principle those are equivalent experiments: in both cases one applies an electric field to the sample. However, in the case of Ca_2RuO_4 voltage switching, as illustrated in the figure from [135], induces a sudden, effectively instanteneous switch from one phase to another. On the other hand, the application of current (meaning that one uses a current source to provide the voltage whose impedance far exceeds that of the sample) induces a gradual phase change which includes a region of phase coexistence. We note that both methods exhibit hysteresis with respect to the applied stimulus establishing the first order nature of the field-driven IMT.

6.3.2 Phase texture across the field-driven IMT

An important contribution to the literature on the switching phenomenon in Ca_2RuO_4 is [129]. Utilizing the fact that the current driven transition induces a region of phase coexistence the authors performed optical and near-field nanoimaging of the sample as it undergoes the transition. It turns out that the difference in optical contrast between the two phases makes it possible to see the phase composition of the sample with a naked eye (and the magnification provided by an optical microscope) and the amazing imaging results they obtained are reproduced in 6.2. Zhang et al. found that in the case of Ca_2RuO_4 the phase transition proceed through nucleation, as the metallic phase is

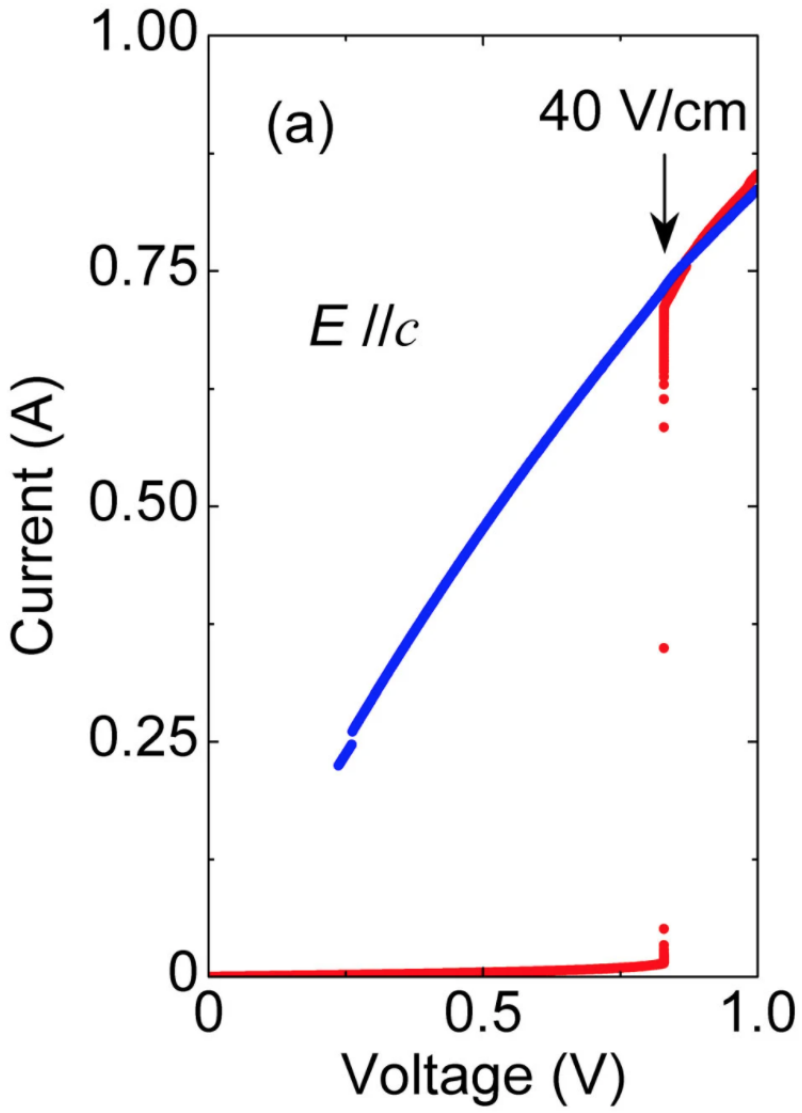

Figure 6.1: Reproduced from [135]. Voltage-controlled IMT in Ca_2RuO_4. The experiment is performed by increasing the voltage from zero (red line) until a sharp rise in current at a threshold voltage that indicates a voltage driven insulator-metal transition. Returning from the metallic phase, reducing the voltage from a high value (1.0V in this case) toward zero, one observes that the switching voltage is different (lower) than when the voltage is increased. This hysteresis is a consequence of the strongly first order nature of this IMT. There is no trace between $\sim$ 0.25V and zero because Ca_2RuO_4 single crystals often break when transitioning from metal to insulator due to the huge (10%) volume deformation which that transition entails.

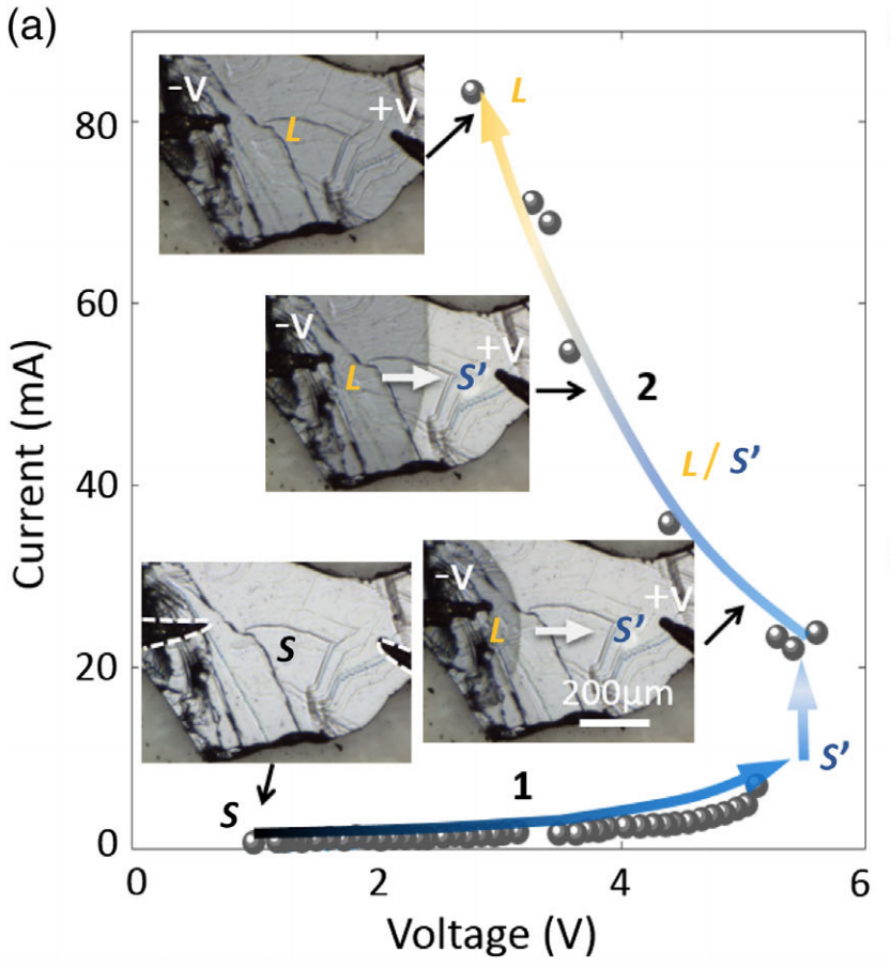

Figure 6.2: Reproduced from [129]. The contents of this figure is two fold. Firstly, it shows the current-voltage characteristic of the field-driven IMT in Ca_2RuO_4 when current is controlled and, secondly, it contains optical images of the sample at different stages of the transition revealing the patterns of phase coexistence which occur. We see that as the current is increased the voltage increases until it peaks and the voltage begins to decrease with increasing current. This phenomenon of negative differential resistance is attributed to phase coexistence as regions of the sample are converted from high-resistance (insulating) to low-resistance (metallic). We see from the optical images that the metallic phase (dark) nucleates from one electrode and the phase front propagates through the sample until the entire crystal has been converted.

6.4 Field-driven switching in $Ca_3(Ru_{1-x}Ti_x)_2O_7$

6.4.1 Similarity between Ca_2RuO_4 and $Ca_3(Ru_{1-x}Ti_x)_2O_7$

The relationship between Ca_2RuO_4 and $Ca_3(Ru_{1-x}Ti_x)_2O_7$ is a close one [141]. The two compounds are member of the Ruddlesden-Popper series $Ca_{n+1}RunO_{3n+1}$ with struc-

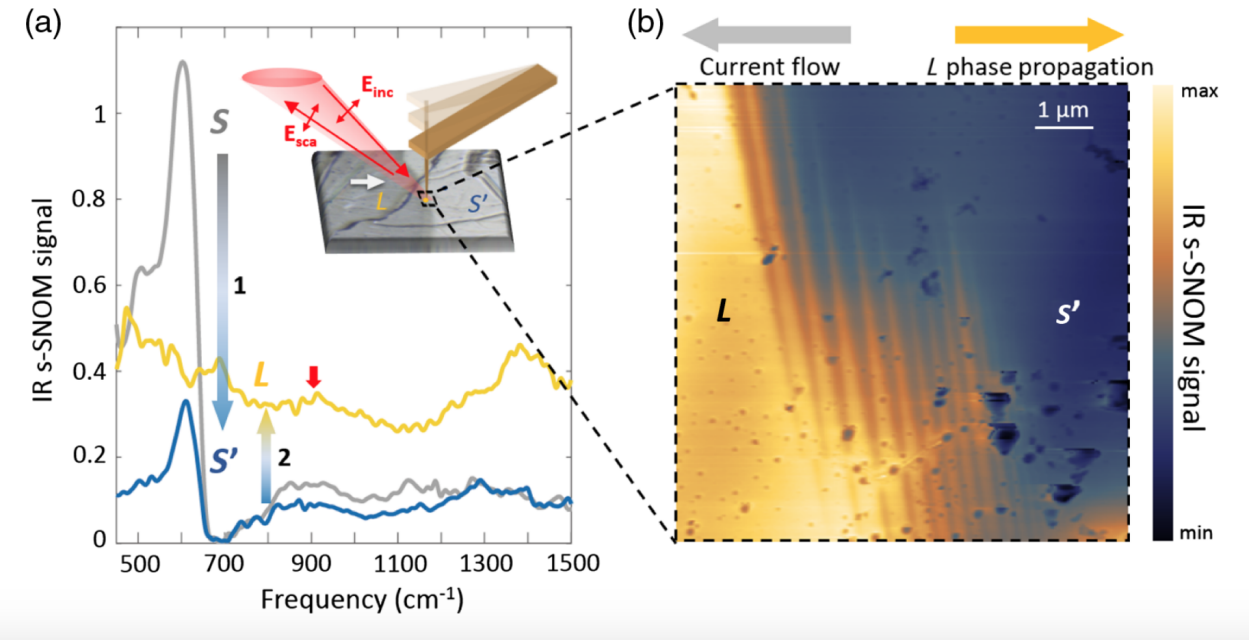

Figure 6.3: Reproduced from [129]. Two crucial findings of [129] were the discovery of microstripe patterns of phase coexistence at the phase front where the insulating and metallic phases coexist. [129] explained this result in terms of a model of strain mismatch at the phase boundary. A second important finding was the discovery, through a spectroscopic measurement whose results are shown in the left panel, of an intermediate phase between the equilibrium insulating phase and the metallic phase found when high electric fields are applied. The role and origin of that intermediate phase remains under debate.

ture which interpolate between the monolayer Ca_2RuO_4 and $n \rightarrow \infty$ limits according to their chemical formula. Focusing on $Ca_3Ru_2O_7$, the bilayer compound, it possesses a larger bandwidth than the monolayer due to dimerization between the upper and lower Ru-O layers, and it evinces a weaker correlation effect than the monolayer material [141]. As described in detail in Chapter 4 and in [101] one significant difference between Ca_2RuO_4 and $Ca_3(Ru_{1-x}Ti_x)_2O_7$ is the presence of a magnetic transition in the latter which couples to the metal-insulator transition. While to the best of our knowledge observations of stripes across the temperature-driven transition have not been observed in Ca_2RuO_4, preliminary data to that effect have been presented at the American Physical Society conference, reinforcing the analogy between the two compounds [158].

6.4.2 Current-voltage characteristics of field-driven switching

[159] reported the discovery of a field-driven transition in $Ca_3(Ru_{1-x}Ti_x)_2O_7$ for the doping level of $x = 0.1$, identical to the one we use in our studies. Figure 6.4 shows Zou et al.'s results for the threshold critical field with voltage and current applied and measured along the c axis. We note that these values are not scaled with the sample dimensions (nor should they be, since the two-probe measurement being performed is not a purely material-dependent measurement due to the contributions of electrical contacts) such that the raw values cannot be compared between samples. Scaling the vertical axis in the figure by the thickness of the sample we find that the range 50-200V corresponds to 0.3-1.3MV/m electric field. Figure 6.5 shows our measurements of the critical fields with the current applied within the ab-plane. We find that the order of magnitude of the threshold fields is around 2x less with the current oriented within the ab-plane than when it is parallel to the c-axis for reasons which, to the best of our knowledge, have not been clarified within the literature.

6.4.3 In-plane critical field results

Our first result on the field-driven phenomenon in $Ca_3(Ru_{0.9}Ti_{0.1})_2O_7$ is a measurement of the thermal dependence of the threshold electric field and currents for current and voltage oriented within the ab crystal plane, shown in Figure 6.5. Salient features of this result are as follows. Firstly, the magnitude of the threshold field which we measure for current oriented along the in-plane direction is less than half an order of magnitude less than the field reported by [159] for the same temperature range with the field aligned along the c-axis. Concretely [159] observe a threshold field of $\sim$ 30V across a sample of thickness 0.15mm, corresponding to 200kV/m in the c-axis case, as compared to 70kV/m observed by us for the ab-plane case.

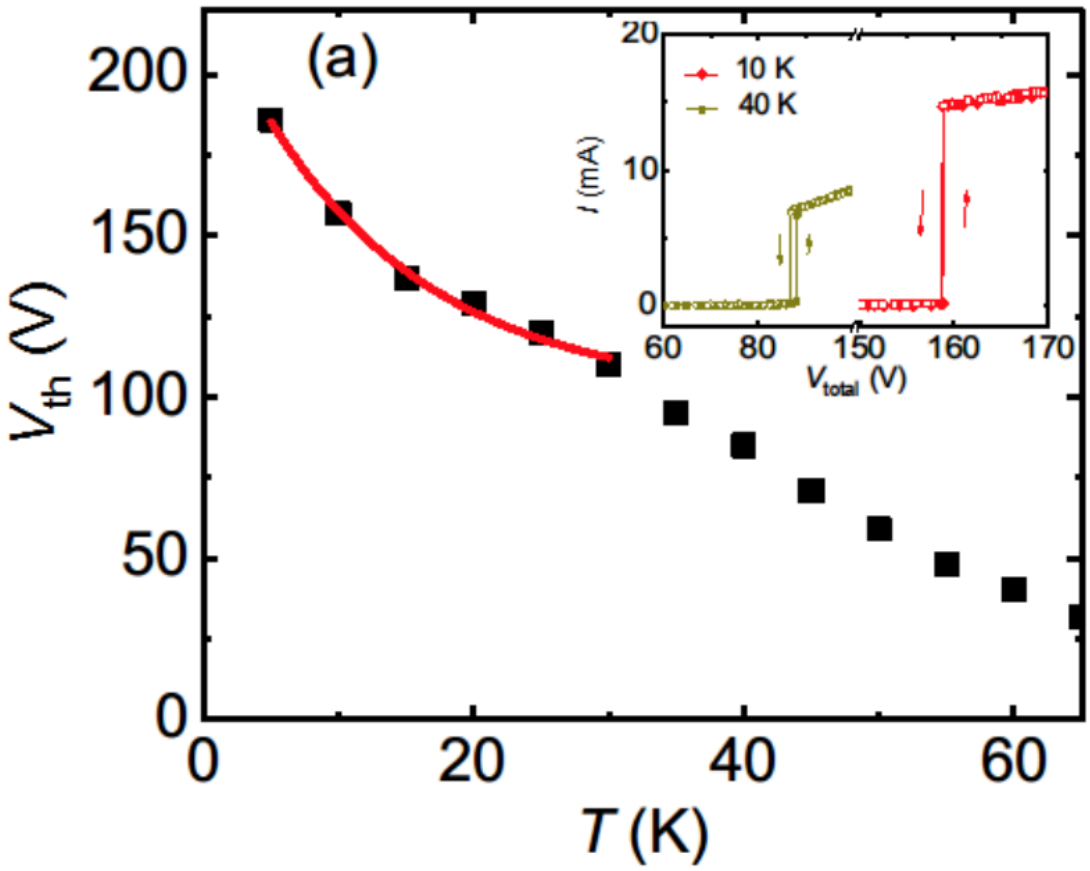

Figure 6.4: Reproduced from [159]. The figure shows the critical voltage as function of temperature for a CTRO sample with current and voltage applied along the c-axis. The authors cite the thickness of their sample (the dimension along the field direction) to be 0.15mm such that the vertical axis corresponds to 0.3-1.3MV/m. When we compare these values to our in-plane field measurements in 6.5 we find that the threshold fields are roughly 10x larger for electric fields applied along the c-axis than when the field is applied within the ab-plane.

6.5 Nanoimaging of the field-driven IMT in CRTO

In the case of Ca_2RuO_4, [129] found that it is possible to glimpse the global picture of phase coexistence within a sample undergoing the IMT with the naked eye (albeit likely helped by the magnification of an optical microscope). This was explained as being a consequence of the difference between the optical constants between the insulating and metallic phases. Optical imaging of a $Ca_3(Ru_{0.9}Ti_{0.1})_2O_7$ undergoing a field-driven IMT offer the ability to observe the phase coexistence in the sample. While it is not possible in the images

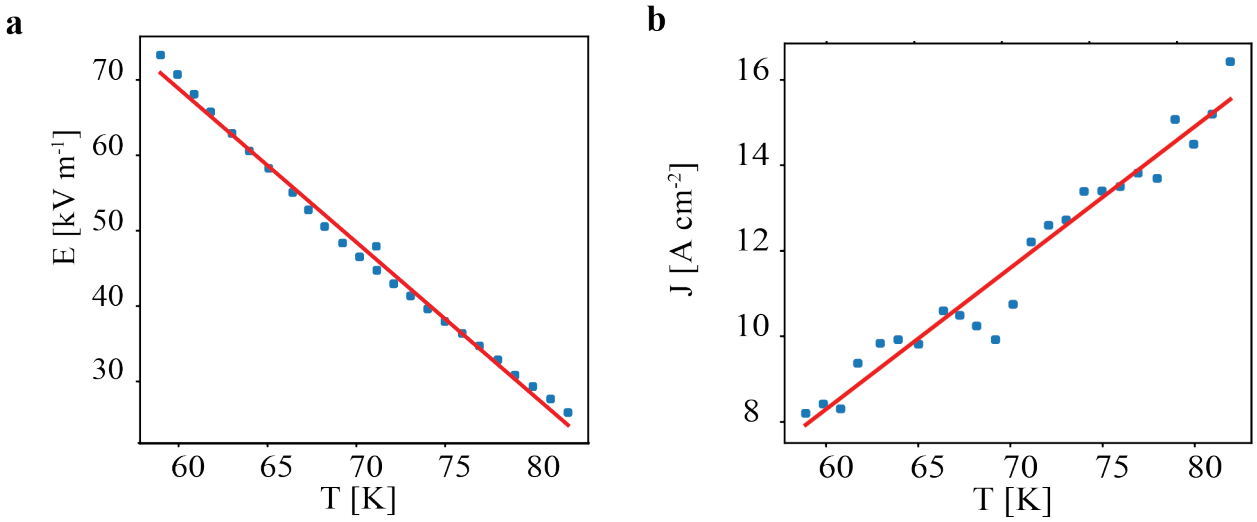

Figure 6.5: Critical electric field and critical current for switching with current applied within the *ab*-plane. The data was obtained from the location of the first turning point in the current-voltage curve produced by applying a variable current bias to the sample at different, fixed temperatures. The raw data points are shown in blue. Shown in red are linear fits to the thermal dependence of these quantities.

we took to distinguish the two homogeneous phases, we *are* able to make out the spatial corrugations on the surface of the crystal that correspond to the stripe texture. An image (viz. Fig. 6.6) of the sample with enhanced contrast (an inverse transformation followed by a gamma transformation with $\gamma = 1.4$) is shown in panel a. We note the presence of stripe texture throughout the sample and the absence of a single propagating phase front, indicating a difference in the patterns of phase coexistence which occur in this material versus the monolayer ruthenate Ca_2RuO_4.

A part of the contents of the previous observation is the apparent absence of polarity asymmetry in this transition, in stark contrast to Ca_2RuO_4 where this asymmetry is marked and reliably observed. To further investigate this point we performed repeated near-field scanning optical nano-imaging along a fixed-line parallel to the *b*-axis of a 300 micron-long rectangular crystal while linearly increasing the applied current. We resolved the domain textures which form and disappear through this process in a single spot on the crystal near one of the electrodes for the two possible polarity configurations. We found (viz. panel b of Fig. 6.6) that there is no observable effect of polarity switching, reinforcing the conclusions

we drew from optical images of the transition.

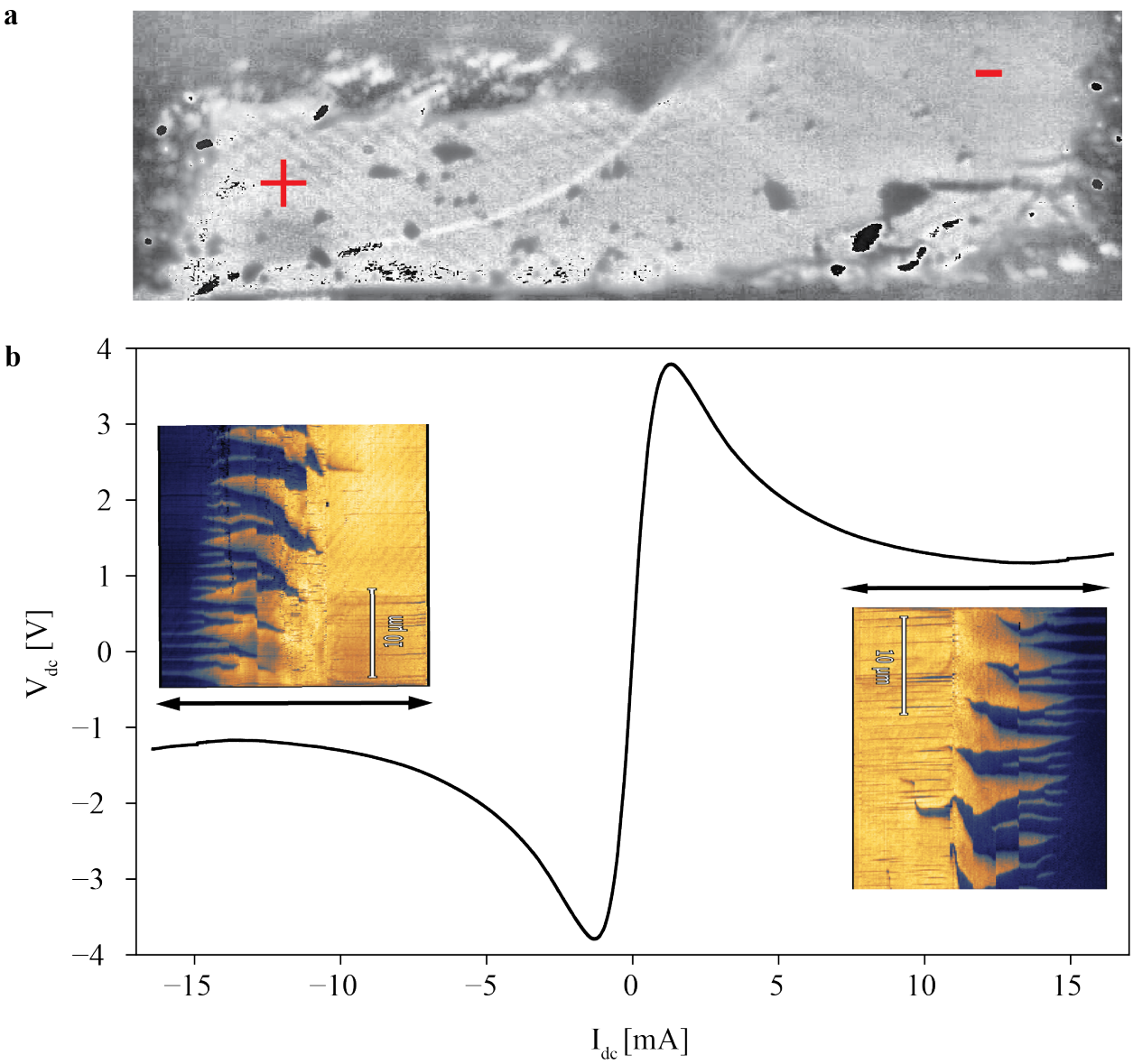

Figure 6.6: (Color online) a) An optical image of a $Ca_3(Ru_{0.9}Ti_{0.1})_2O_7$ sample undergoing current-driven metallization. Locations of the positive (negative) electrode are indicated with red plus (minus) signs. Spatial corrugations are visible which indicate the presence of stripe phase texture in those regions. We note that in contrast to Ca_2RuO_4 stripe phase coexistence patterns appear throughout the sample, not at single propagating phase front and, furthermore, polarity dependence is not observed.

6.6 Elastosusceptiblity across the field-driven IMT

To further characterize the field-driven transition in $Ca_3(Ru_{0.9}Ti_{0.1})_2O_7$ we performed elastoresistance measurements as function of applied current bias to a sample that undergoes it.

Technically, we achieved this measurement by sourcing a small alternating voltage to the piezoelectric actuators such that a small alternating strain ϵ_{ac} is applied to the sample, simultaneously with sourcing a direct, possibly large, current to the sample, I_{dc}, which tunes the sample across the field-driven transition. The resulting voltage which develops across the sample is

$$V(I_{dc}, \epsilon_{ac}) = I_{dc} R(\epsilon_{ac}) \tag{6.1}$$

Since the applied strain is small we may linearize $R(\epsilon)$ to get

$$V(I_{dc}, \epsilon_{ac}) = I_{dc} R_0 + I_{dc} \epsilon_{ac} \frac{dR}{d\epsilon} \tag{6.2}$$

where R_0 is the resistance of the sample with no external strain applied. We may then measure the elastoresistance component, represented by the second part, via the standard lock-in amplification technique and thus extract the elastoresistance $\frac{dR}{d\epsilon}$.

Our results are presented in figure 6.7. We note that due to the spatially textured nature of this transition the quantity which we plot as the susceptiblity, η, is concretely

$$\eta_{b,plot} = \frac{1}{V_{dc}/I_{dc}} \frac{dR}{d\epsilon} \tag{6.3}$$

The appropriate starting point for the discussion of this measurement are the end-points of the transition since those correspond to the fully converted phases (the equilibrium insulating phase in the case of low current and the field-induced metallic phase in the case of high current). In the low-current case we verify that the elastosusceptiblity of the sample corresponds to the value we expect based on previous elastosusceptiblity measurements (see

Chapter 4). At high currents we notice that the value of susceptibility of the fully metallized sample is coincident with the susceptibility of the equilibrium metallic phase obtained through thermal stimulus as expected based on similar evidence in the presumably related switching phenomenon in Ca_2RuO_4. We therefore conclude, tentatively, that these curved should be interpreted as measurements of the elastosusceptibility of a two-phase mixture of insulator and metal as function of d.c. current which tunes between the two homogeneous phase endpoints.

Focusing now on the structure of these curves in the region which we know is associated with phase coexistence we notice the two salient peak features, indicated by black arrows in 6.7. The values of current at which these features occur coincide with the two turning points in the current-voltage curve which we know are associated with phase boundaries: the nucleation of the first droplet of the field-stabilized metallic phase and the field-induced disappearance of the last droplet of the insulating phase for the low current and high current points, respectively. We note the remarkable similarity between this curve and the elastosusceptibility curve which the authors observed in the temperature-driven IMT [138] and where the origin of the peaks was attributed to the strain susceptiblity of the phase mixture composition (concretely, the susceptiblity of the phase fraction, $df/d\epsilon$). We suggest that it is likely the origin of the features we observe here is similar: the susceptibility of the phase mixture, here driven by the application of an electric field as opposed to temperature. More broadly, this result implies a close connection between the thermal and field-driven IMT in $Ca_3(Ru_{0.9}Ti_{0.1})_2O_7$ and it is consistent with the emerging literature consensus that, while the details of how the metallic phase is stabilized remain unclear, the effect of a field is to induce a switching between the two phases that serve as endpoints for the temperature-driven IMT.

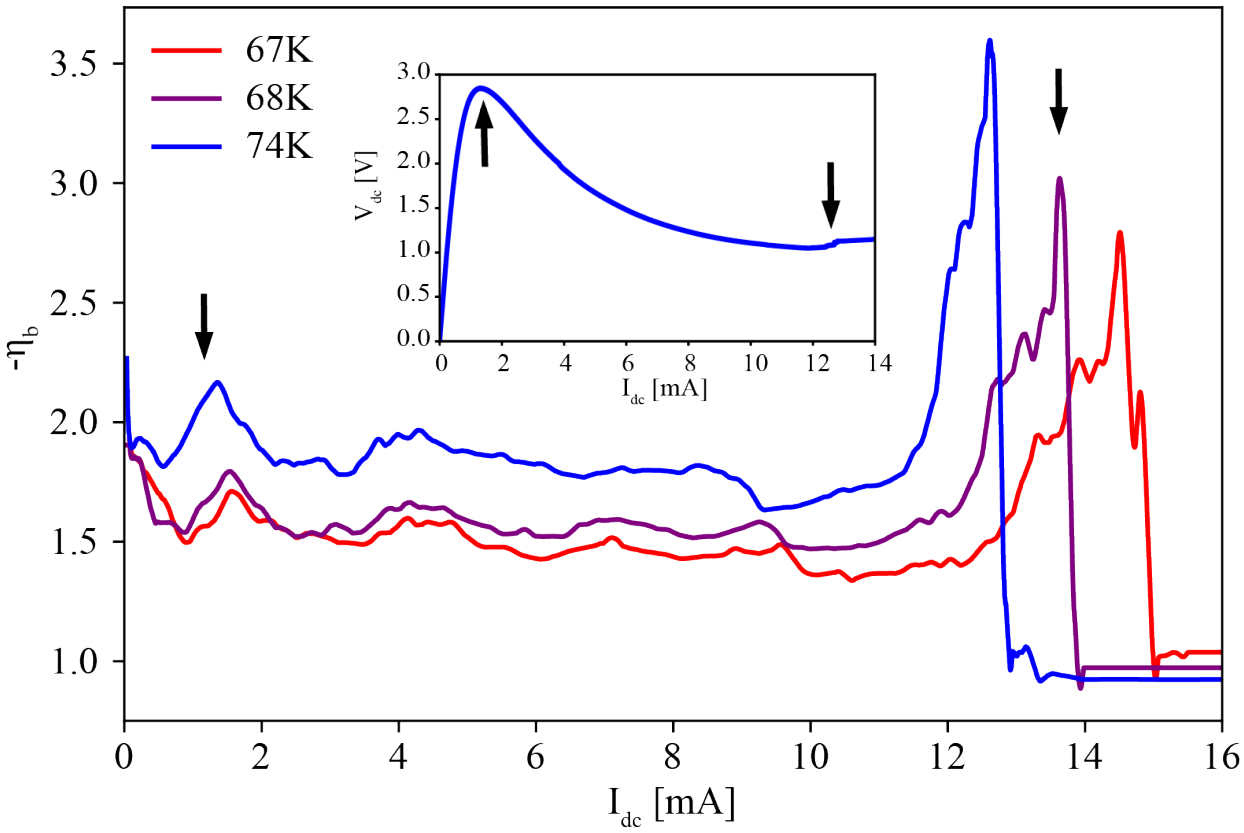

Figure 6.7: Elastosusceptiblity measurements for $Ca_3(Ru_{0.9}Ti_{0.1})_2O_7$ across the field-driven IMT. The main panel shows the negative of the b-axis susceptibility at three different temperatures $T < T_c$ below the thermal IMT transition temperature. The curves for 74K, 68K and 67K are in blue, purple and red, respectively.

References

[1] L. D. Landau and E. M. Lifshitz. Elsevier, 2013.

[2] G. Grüner, Reviews of modern physics, vol. 60, no. 4, p. 1129, 1988.

[3] W Tabis, Y Li, M Le Tacon, L. Braicovich, A Kreyssig, M. Minola, G. Dellea, E Weschke, M. Veit, M Ramazanoglu, et al., Nature communications, vol. 5, no. 1, pp. 1–6, 2014.

[4] P. Dai, Reviews of Modern Physics, vol. 87, no. 3, p. 855, 2015.

[5] J.-H. Chu, H.-H. Kuo, J. G. Analytis, and I. R. Fisher, Science, vol. 337, no. 6095, pp. 710–712, 2012.

[6] J. Mutch, W.-C. Chen, P. Went, T. Qian, I. Z. Wilson, A. Andreev, C.-C. Chen, and J.-H. Chu, Science advances, vol. 5, no. 8, eaav9771, 2019.

[7] S. Burghartz and B. Schulz, "Thermophysical properties of sapphire, aln and mgal2o4 down to 70 k," Journal of Nuclear Materials, vol. 212-215, pp. 1065 –1068, 1994, Fusion Reactor Materials.

[8] R. P. Taylor, G. F. Nellis, S. A. Klein, D. W. Hoch, J. Fellers, P. Roach, J. M. Park, and Y. Gianchandani, "Measurements of the material properties of a laminated piezoelectric stack at cryogenic temperatures," AIP Conference Proceedings, vol. 824, no. 1, pp. 200–207, 2006. eprint: `https://aip.scitation.org/doi/pdf/10.1063/1.2192352`.

[9] A. M. Simpson and W. Wolfs, "Thermal expansion and piezoelectric response of pzt channel 5800 for use in low-temperature scanning tunneling microscope designs," Review of Scientific Instruments, vol. 58, no. 11, pp. 2193–2195, 1987. eprint: `https://doi.org/10.1063/1.1139486`.

[10] S. Bukhari, M. Islam, A. Haziot, and J. Beamish, Journal of Physics: Conference Series, vol. 568, no. 3, p. 032 004, 2014.

[11] M. H. et al., Japanese Journal of Applied Physics, vol. 49, no. 9S, p. 09MD04, 2010.

[12] M. A. Trindade and A. Benjeddou, "Finite element characterization and parametric analysis of the nonlinear behaviour of an actual d 15 shear mfc," Acta Mechanica, vol. 224, no. 11, pp. 2489–2503, 2013.

[13] Q. ming Wang, B. Xu, V. D. Kugel, and L. E. Cross, vol. 2, 767–770 vol.2, 1996.

[14] R. G. Sabat, W. Ren, G. Yang, and B. K. Mukherjee, pp. 612–615, 2007.

[15] M. Barmatz, L. R. Testardi, and F. J. Di Salvo, "Elasticity measurements in the layered dichalcogenides tase2 and nbse2," Phys. Rev. B, vol. 12, pp. 4367–4376, 10 1975.

[16] C. W. Hicks, M. E. Barber, S. D. Edkins, D. O. Brodsky, and A. P. Mackenzie, "Piezoelectric-based apparatus for strain tuning," Review of Scientific Instruments, vol. 85, no. 6, p. 065 003, 2014. eprint: https://doi.org/10.1063/1.4881611.

[17] A. Pustogow, A. S. McLeod, Y. Saito, D. N. Basov, and M. Dressel, Science advances, vol. 4, no. 12, eaau9123, 2018.

[18] M. M. Qazilbash, M. Brehm, B.-G. Chae, P.-C. Ho, G. O. Andreev, B.-J. Kim, S. J. Yun, A. Balatsky, M. Maple, F. Keilmann, et al., Science, vol. 318, no. 5857, pp. 1750–1753, 2007.

[19] H. U. e. a. Yang, Review of Scientific Instruments, vol. 84, no. 2, p. 023 701, 2013.

[20] J. M. Atkin, S. Berweger, A. C. Jones, and M. B. Raschke, Advances in Physics, vol. 61, no. 6, pp. 745–842, 2012.

[21] K. Post, A. McLeod, M. Hepting, M. Bluschke, Y. Wang, G Cristiani, G. Logvenov, A. Charnukha, G. Ni, P. Radhakrishnan, et al., Nature Physics, vol. 14, no. 10, pp. 1056–1061, 2018.

[22] N. Ocelic, A. Huber, and R. Hillenbrand, Applied Physics Letters, vol. 89, no. 10, p. 101 124, 2006.

[23] L. M. Zhang, G. O. Andreev, Z. Fei, A. S. McLeod, G. Dominguez, M. Thiemens, A. Castro-Neto, D. Basov, and M. M. Fogler, Physical Review B, vol. 85, no. 7, p. 075 419, 2012.

[24] B. Knoll and F. Keilmann, Optics communications, vol. 182, no. 4-6, pp. 321–328, 2000.

[25] W. Melitz, J. Shen, A. C. Kummel, and S. Lee, Surface science reports, vol. 66, no. 1, pp. 1–27, 2011.

[26] J. Tranquada, B. Sternlieb, J. Axe, Y Nakamura, and S Uchida, nature, vol. 375, no. 6532, pp. 561–563, 1995.

[27] J Chang, E Blackburn, A. Holmes, N. B. Christensen, J. Larsen, J Mesot, R. Liang, D. Bonn, W. Hardy, A Watenphul, et al., Nature Physics, vol. 8, no. 12, pp. 871–876, 2012.

[28] C. de La Cruz, Q Huang, J. Lynn, J. Li, W Ratcliff Ii, J. L. Zarestky, H. Mook, G. Chen, J. Luo, N. Wang, et al., nature, vol. 453, no. 7197, pp. 899–902, 2008.

[29] L. e. a. Zhao, Nature Physics, vol. 13, no. 3, pp. 250–254, 2017.

[30] J Wu, A. Bollinger, X He, and I Božović, Nature, vol. 547, no. 7664, pp. 432–435, 2017.

[31] K Matano, M Kriener, K Segawa, Y Ando, and G.-q. Zheng, Nature Physics, vol. 12, no. 9, pp. 852–854, 2016.

[32] S. Yonezawa, K. Tajiri, S. Nakata, Y. Nagai, Z. Wang, K. Segawa, Y. Ando, and Y. Maeno, Nature Physics, vol. 13, no. 2, pp. 123–126, 2017.

[33] S. C. Riggs, M. Shapiro, A. V. Maharaj, S Raghu, E. Bauer, R. Baumbach, P Giraldo-Gallo, M. Wartenbe, and I. Fisher, Nature communications, vol. 6, no. 1, pp. 1–6, 2015.

[34] A. Kerelsky, L. J. McGilly, D. M. Kennes, L. Xian, M. Yankowitz, S. Chen, K Watanabe, T Taniguchi, J. Hone, C. Dean, et al., Nature, vol. 572, no. 7767, pp. 95–100, 2019.

[35] Y. Choi, J. Kemmer, Y. Peng, A. Thomson, H. Arora, R. Polski, Y. Zhang, H. Ren, J. Alicea, G. Refael, et al., Nature Physics, vol. 15, no. 11, pp. 1174–1180, 2019.

[36] Y. Cao, D. Rodan-Legrain, J. M. Park, F. N. Yuan, K. Watanabe, T. Taniguchi, R. M. Fernandes, L. Fu, and P. Jarillo-Herrero, arXiv preprint arXiv:2004.04148, 2020.

[37] B. Keimer, S. A. Kivelson, M. R. Norman, S. Uchida, and J Zaanen, Nature, vol. 518, no. 7538, pp. 179–186, 2015.

[38] R. Fernandes, A. Chubukov, and J Schmalian, Nature physics, vol. 10, no. 2, pp. 97–104, 2014.

[39] P. Malinowski, Q. Jiang, J. J. Sanchez, J. Mutch, Z. Liu, P. Went, J. Liu, P. J. Ryan, J.-W. Kim, and J.-H. Chu, Nature Physics, vol. 16, no. 12, pp. 1189–1193, 2020.

[40] M. S. Ikeda, T. Worasaran, J. C. Palmstrom, J. Straquadine, P Walmsley, and I. Fisher, Physical Review B, vol. 98, no. 24, p. 245 133, 2018.

[41] H.-H. Kuo, J.-H. Chu, J. C. Palmstrom, S. A. Kivelson, and I. R. Fisher, Science, vol. 352, no. 6288, pp. 958–962, 2016.

[42] C. W. Hicks, D. O. Brodsky, E. A. Yelland, A. S. Gibbs, J. A. N. Bruin, M. E. Barber, S. D. Edkins, K. Nishimura, S. Yonezawa, Y. Maeno, and A. P. Mackenzie, "Strong increase of tc of sr2ruo4 under both tensile and compressive strain," Science, vol. 344, no. 6181, pp. 283–285, 2014. eprint: `http://science.sciencemag.org/content/344/6181/283.full.pdf`.

[43] A. Steppke, L. Zhao, M. E. Barber, T. Scaffidi, F. Jerzembeck, H. Rosner, A. S. Gibbs, Y. Maeno, S. H. Simon, A. P. Mackenzie, et al., Science, vol. 355, no. 6321, 2017.

[44] Y Maeno, H Hashimoto, K Yoshida, S Nishizaki, T Fujita, J. Bednorz, and F Lichtenberg, nature, vol. 372, no. 6506, pp. 532–534, 1994.

[45] C Kallin and A. Berlinsky, Journal of Physics: Condensed Matter, vol. 21, no. 16, p. 164 210, 2009.

[46] A. P. Mackenzie and Y. Maeno, Reviews of Modern Physics, vol. 75, no. 2, p. 657, 2003.

[47] A. P. Mackenzie, T. Scaffidi, C. W. Hicks, and Y. Maeno, npj Quantum Materials, vol. 2, no. 1, pp. 1–9, 2017.

[48] Y Maeno, T Ando, Y Mori, E Ohmichi, S Ikeda, S NishiZaki, and S Nakatsuji, Physical review letters, vol. 81, no. 17, p. 3765, 1998.

[49] Y.-S. e. a. Li, Proceedings of the National Academy of Sciences, vol. 118, no. 10, 2021.

[50] R. Comin and A. Damascelli, Annual Review of Condensed Matter Physics, vol. 7, pp. 369–405, 2016.

[51] A. e. a. Aharony, Physical review letters, vol. 60, no. 13, p. 1330, 1988.

[52] S. Chakravarty, B. I. Halperin, and D. R. Nelson, Physical Review B, vol. 39, no. 4, p. 2344, 1989.

[53] J. G. Bednorz and K. A. Müller, Zeitschrift für Physik B Condensed Matter, vol. 64, no. 2, pp. 189–193, 1986.

[54] S. A. Kivelson, I. P. Bindloss, E. Fradkin, V. Oganesyan, J. Tranquada, A. Kapitulnik, and C. Howald, Reviews of Modern Physics, vol. 75, no. 4, p. 1201, 2003.

[55] A. Melikyan and M. Norman, Physical Review B, vol. 89, no. 2, p. 024 507, 2014.

[56] J. e. a. Robertson, Physical Review B, vol. 74, no. 13, p. 134 507, 2006.

[57] K. Seo, H.-D. Chen, and J. Hu, Physical Review B, vol. 76, no. 2, p. 020 511, 2007.

[58] A. e. a. Soumyanarayanan, Proceedings of the National Academy of Sciences, vol. 110, no. 5, pp. 1623–1627, 2013.

[59] H.-H. Kim, S. Souliou, M. Barber, E Lefrançois, M Minola, M Tortora, R Heid, N Nandi, R. A. Borzi, G Garbarino, et al., Science, vol. 362, no. 6418, pp. 1040–1044, 2018.

[60] F. Von Rohr, J.-C. Orain, R Khasanov, C Witteveen, Z Shermadini, A Nikitin, J Chang, A. Wieteska, A. Pasupathy, M. Hasan, et al., Science advances, vol. 5, no. 11, eaav8465, 2019.

[61] J. A. Wilson and A. Yoffe, Advances in Physics, vol. 18, no. 73, pp. 193–335, 1969.

[62] S. e. a. Manzeli, Nature Reviews Materials, vol. 2, no. 8, pp. 1–15, 2017.

[63] S. Z. Butler, S. M. Hollen, L. Cao, Y. Cui, J. A. Gupta, H. R. Gutiérrez, T. F. Heinz, S. S. Hong, J. Huang, A. F. Ismach, et al., ACS nano, vol. 7, no. 4, pp. 2898–2926, 2013.

[64] F. Flicker and J. van Wezel, Nature Communications, vol. 6, p. 7034, 2015.

[65] I Guillamon, H Suderow, F Guinea, and S Vieira, Physical Review B, vol. 77, no. 13, p. 134 505, 2008.

[66] J. Wilson, F. Di Salvo, and S Mahajan, Physical review letters, vol. 32, no. 16, p. 882, 1974.

[67] T. Yokoya, T Kiss, A Chainani, S Shin, M. Nohara, and H Takagi, Science, vol. 294, no. 5551, pp. 2518–2520, 2001.

[68] D. Moncton, J. Axe, and F. DiSalvo, Physical Review Letters, vol. 34, no. 12, p. 734, 1975.

[69] S. Dordevic, D. Basov, R. Dynes, and E Bucher, Physical Review B, vol. 64, no. 16, p. 161 103, 2001.

[70] F Weber, S Rosenkranz, J.-P. Castellan, R Osborn, R Hott, R Heid, K.-P. Bohnen, T Egami, A. Said, and D Reznik, Physical review letters, vol. 107, no. 10, p. 107 403, 2011.

[71] C. J. Arguello, S. P. Chockalingam, E. P. Rosenthal, L. Zhao, C. Gutiérrez, J. Kang, W. Chung, R. M. Fernandes, S. Jia, A. J. Millis, et al., Physical Review B, vol. 89, no. 23, p. 235 115, 2014.

[72] C. J. Arguello, E. P. Rosenthal, E. F. Andrade, W. Jin, P. Yeh, N. Zaki, S. Jia, R. J. Cava, R. M. Fernandes, A. J. Millis, et al., Physical review letters, vol. 114, no. 3, p. 037 001, 2015.

[73] S. Gao, F. Flicker, R. Sankar, H. Zhao, Z. Ren, B. Rachmilowitz, S. Balachandar, F. Chou, K. S. Burch, Z. Wang, J. van Wezel, and I. Zeljkovic, "Atomic-scale strain manipulation of a charge density wave," Proceedings of the National Academy of Sciences, vol. 115, no. 27, pp. 6986–6990, 2018.

[74] F. Flicker, Ph.D. dissertation, University of Bristol, 2015.

[75] K. Cho, M Kończykowski, S. Teknowijoyo, M. A. Tanatar, J Guss, P. Gartin, J. M. Wilde, A Kreyssig, R. McQueeney, A. I. Goldman, et al., Nature communications, vol. 9, no. 1, pp. 1–9, 2018.

[76] M. Leroux, I. Errea, M. Le Tacon, S.-M. Souliou, G. Garbarino, L. Cario, A. Bosak, F. Mauri, M. Calandra, and P. Rodière, Physical Review B, vol. 92, no. 14, p. 140 303, 2015.

[77] Y. Feng, J. Wang, R Jaramillo, J. Van Wezel, S Haravifard, G Srajer, Y Liu, Z.-A. Xu, P. Littlewood, and T. Rosenbaum, Proceedings of the National Academy of Sciences, vol. 109, no. 19, pp. 7224–7229, 2012.

[78] F. Flicker and J. van Wezel, Physical Review B (Rapid Communications), vol. 92, 201103(R), 2015.

[79] F. Flicker and J. van Wezel, "Charge order in **nbse**2," Phys. Rev. B, vol. 94, p. 235 135, 23 2016.

[80] F. Weber, S. Rosenkranz, J.-P. Castellan, R. Osborn, R. Hott, R. Heid, K.-P. Bohnen, T. Egami, A. H. Said, and D. Reznik, Phys. Rev. Lett., vol. 107, p. 107 403, 10 2011.

[81] F. Weber, R. Hott, R. Heid, K.-P. Bohnen, S. Rosenkranz, J.-P. Castellan, R. Osborn, A. H. Said, B. M. Leu, and D. Reznik, Phys. Rev. B, vol. 87, p. 245 111, 24 2013.

[82] M. R. Norman, H. Ding, H. Fretwell, M. Randeria, and J. C. Campuzano, Phys. Rev. B, vol. 60, pp. 7585–7590, 10 1999.

[83] D. J. Rahn, S. Hellmann, M. Kalläne, C. Sohrt, T. K. Kim, L. Kipp, and K. Rossnagel, Phys. Rev. B, vol. 85, p. 224 532, 22 2012.

[84] S. V. Borisenko, A. A. Kordyuk, V. B. Zabolotnyy, D. S. Inosov, D. Evtushinsky, B. Büchner, A. N. Yaresko, A. Varykhalov, R. Follath, W. Eberhardt, L. Patthey, and H. Berger, Phys. Rev. Lett., vol. 102, p. 166 402, 16 2009.

[85] X. e. a. Xi, Nature nanotechnology, vol. 10, no. 9, pp. 765–769, 2015.

[86] A. Tsen, B Hunt, Y. Kim, Z. Yuan, S Jia, R. Cava, J Hone, P. Kim, C. Dean, and A. Pasupathy, Nature Physics, vol. 12, no. 3, pp. 208–212, 2016.

[87] A. Benyamini, D. M. Kennes, E. J. Telford, K. Watanabe, T. Taniguchi, A. J. Millis, J. Hone, C. R. Dean, and A. N. Pasupathy, Nano Letters, 2020.

[88] E. Dagotto, Science, vol. 309, no. 5732, pp. 257–262, 2005.

[89] G. Milward, M. Calderon, and P. Littlewood, Nature, vol. 433, no. 7026, pp. 607–610, 2005.

[90] E. Dagotto. Springer Science & Business Media, 2013, vol. 136.

[91] T. Li, A. Patz, L. Mouchliadis, J. Yan, T. A. Lograsso, I. E. Perakis, and J. Wang, Nature, vol. 496, no. 7443, pp. 69–73, 2013.

[92] M. Imada, A. Fujimori, and Y. Tokura, Reviews of modern physics, vol. 70, no. 4, p. 1039, 1998.

[93] J.-P. Locquet, J Perret, J Fompeyrine, E Mächler, J. W. Seo, and G Van Tendeloo, Nature, vol. 394, no. 6692, pp. 453–456, 1998.

[94] B. Burganov, C. Adamo, A. Mulder, M Uchida, P. King, J. Harter, D. Shai, A. Gibbs, A. Mackenzie, R. Uecker, et al., Physical review letters, vol. 116, no. 19, p. 197 003, 2016.

[95] X.-Z. Lu and J. M. Rondinelli, Nature materials, vol. 15, no. 9, pp. 951–955, 2016.

[96] J. H. Park, J. M. Coy, T. S. Kasirga, C. Huang, Z. Fei, S. Hunter, and D. H. Cobden, Nature, vol. 500, no. 7463, pp. 431–434, 2013.

[97] J. Wu, Q. Gu, B. S. Guiton, N. P. De Leon, L. Ouyang, and H. Park, Nano letters, vol. 6, no. 10, pp. 2313–2317, 2006.

[98] N. B. Aetukuri, A. X. Gray, M. Drouard, M. Cossale, L. Gao, A. H. Reid, R. Kukreja, H. Ohldag, C. A. Jenkins, E. Arenholz, et al., Nature Physics, vol. 9, no. 10, pp. 661–666, 2013.

[99] M. Hepting, M. Minola, A. Frano, G. Cristiani, G Logvenov, E Schierle, M Wu, M Bluschke, E Weschke, H.-U. Habermeier, et al., Physical review letters, vol. 113, no. 22, p. 227 206, 2014.

[100] C. Dietl, S. Sinha, G Christiani, Y Khaydukov, T Keller, D Putzky, S Ibrahimkutty, P Wochner, G Logvenov, P. van Aken, et al., Applied Physics Letters, vol. 112, no. 3, p. 031 902, 2018.

[101] Q. Han and A. Millis, Physical review letters, vol. 121, no. 6, p. 067 601, 2018.

[102] Z. e. a. Huang, Physical Review B, vol. 86, no. 1, p. 014 410, 2012.

[103] J. Zhang, X. Tan, M. Liu, S. W. Teitelbaum, K. W. Post, F. Jin, K. A. Nelson, D. N. Basov, W. Wu, and R. D. Averitt, Nature materials, vol. 15, no. 9, pp. 956–960, 2016.

[104] A. S. McLeod, J. Zhang, M. Gu, F. Jin, G Zhang, K. W. Post, X. Zhao, A. J. Millis, W. Wu, J. M. Rondinelli, et al., Nature materials, vol. 19, no. 4, pp. 397–404, 2020.

[105] T Kissikov, R Sarkar, M Lawson, B. Bush, E. I. Timmons, M. A. Tanatar, R. Prozorov, S. Bud'ko, P. C. Canfield, R. Fernandes, et al., Nature communications, vol. 9, no. 1, pp. 1–6, 2018.

[106] M. D. Bachmann, G. Ferguson, F. Theuss, T. Meng, C. Putzke, T. Helm, K. Shirer, Y.-S. Li, K. A. Modic, M. Nicklas, et al., Science, vol. 366, no. 6462, pp. 221–226, 2019.

[107] E. F. Andrade, A. N. Berger, E. P. Rosenthal, X. Wang, L. Xing, X. Wang, C. Jin, R. M. Fernandes, A. J. Millis, and A. N. Pasupathy, arXiv preprint arXiv:1812.05287, 2018.

[108] P Limelette, A Georges, D Jérome, P Wzietek, P Metcalf, and J. Honig, Science, vol. 302, no. 5642, pp. 89–92, 2003.

[109] H. Taniguchi, K. Nishimura, R. Ishikawa, S. Yonezawa, S. K. Goh, F. Nakamura, and Y. Maeno, Physical Review B, vol. 88, no. 20, p. 205 111, 2013.

[110] S. Riccò, M. Kim, A. Tamai, S. M. Walker, F. Y. Bruno, I. Cucchi, E. Cappelli, C. Besnard, T. K. Kim, P. Dudin, et al., Nature communications, vol. 9, no. 1, pp. 1–7, 2018.

[111] M. Liu, M Wagner, E Abreu, S Kittiwatanakul, A McLeod, Z Fei, M Goldflam, S Dai, M. Fogler, J Lu, et al., Physical review letters, vol. 111, no. 9, p. 096 602, 2013.

[112] M. Liu, M. Wagner, J. Zhang, A. McLeod, S. Kittiwatanakul, Z. Fei, E. Abreu, M. Goldflam, A. J. Sternbach, S. Dai, et al., Applied physics letters, vol. 104, no. 12, p. 121 905, 2014.

[113] A. McLeod, E Van Heumen, J. Ramirez, S Wang, T Saerbeck, S Guenon, M Goldflam, L Anderegg, P Kelly, A Mueller, et al., Nature Physics, vol. 13, no. 1, pp. 80–86, 2017.

[114] J. Peng, X Ke, G. Wang, J. Ortmann, D. Fobes, T. Hong, W. Tian, X. Wu, and Z. Mao, Physical Review B, vol. 87, no. 8, p. 085 125, 2013.

[115] J. Lee, S. Moon, B. Yang, J. Yu, U Schade, Y Yoshida, S.-I. Ikeda, and T. Noh, Physical review letters, vol. 98, no. 9, p. 097 403, 2007.

[116] X. Ke, J Peng, D. Singh, T. Hong, W. Tian, C. D. Cruz, and Z. Mao, Physical Review B, vol. 84, no. 20, p. 201 102, 2011.

[117] B. Barker, S. Dutta, C Lupien, P. McEuen, N Kikugawa, Y Maeno, and J. Davis, Physica B: Condensed Matter, vol. 329, pp. 1334–1335, 2003.

[118] J. Lee, M. Allan, M. Wang, J Farrell, S. Grigera, F. Baumberger, J. Davis, and A. Mackenzie, Nature Physics, vol. 5, no. 11, pp. 800–804, 2009.

[119] E. K. Salje, Annual Review of Materials Research, vol. 42, pp. 265–283, 2012.

[120] Y. e. a. Yoshida, Physical Review B, vol. 72, no. 5, p. 054 412, 2005.

[121] M Zhu, J Peng, T Zou, K Prokes, S. Mahanti, T. Hong, Z. Mao, G. Liu, and X Ke, Physical review letters, vol. 116, no. 21, p. 216 401, 2016.

[122] J Peng, M. Gu, X. Gu, G. Zhou, X. Gao, J. Liu, W. Xu, G. Liu, X Ke, L Zhang, et al., Physical Review B, vol. 96, no. 20, p. 205 105, 2017.

[123] T Zou, H. Cao, G. Liu, J Peng, M Gottschalk, M Zhu, and Z. et al., Physical Review B, vol. 94, no. 4, p. 041 115, 2016.

[124] G. Stone, D. Puggioni, S. Lei, M. Gu, K. Wang, Y. Wang, J. Ge, X.-Z. Lu, Z. Mao, J. M. Rondinelli, et al., Physical Review B, vol. 99, no. 1, p. 014 105, 2019.

[125] S. Lei, M. Gu, D. Puggioni, G. Stone, J. Peng, J. Ge, Y. Wang, B. Wang, Y. Yuan, K. Wang, et al., Nano letters, vol. 18, no. 5, pp. 3088–3095, 2018.

[126] Y. S. Oh, X. Luo, F.-T. Huang, Y. Wang, and S.-W. Cheong, Nature materials, vol. 14, no. 4, pp. 407–413, 2015.

[127] J. M. Rondinelli and C. J. Fennie, Advanced Materials, vol. 24, no. 15, pp. 1961–1968, 2012.

[128] M. Liu, A. J. Sternbach, M. Wagner, T. V. Slusar, T. Kong, S. L. Bud'ko, S. Kittiwatanakul, M. Qazilbash, A. McLeod, Z. Fei, et al., Physical Review B, vol. 91, no. 24, p. 245 155, 2015.

[129] J. Zhang, A. S. McLeod, Q. Han, X. Chen, H. A. Bechtel, Z. Yao, S. G. Corder, T. Ciavatti, T. H. Tao, M. Aronson, et al., Physical Review X, vol. 9, no. 1, p. 011 032, 2019.

[130] L. Miao, P. Silwal, X. Zhou, I. Stern, J. Peng, W. Zhang, L. Spinu, Z. Mao, and D. Ho Kim, Applied Physics Letters, vol. 100, no. 5, p. 052 401, 2012.

[131] S. S. Hong, J. H. Yu, D. Lu, A. F. Marshall, Y. Hikita, Y. Cui, and H. Y. Hwang, Science advances, vol. 3, no. 11, eaao5173, 2017.

[132] M. Sanati and A. Saxena, American Journal of Physics, vol. 71, no. 10, pp. 1005–1012, 2003.

[133] J. Paglione, C Lupien, W. MacFarlane, J. Perz, L. Taillefer, Z. Mao, and Y Maeno, Physical Review B, vol. 65, no. 22, p. 220 506, 2002.

[134] G Cao, J Bolivar, S McCall, J. Crow, and R. Guertin, Physical Review B, vol. 57, no. 18, R11039, 1998.

[135] F. e. a. Nakamura, Scientific reports, vol. 3, no. 1, pp. 1–6, 2013.

[136] Y. Ding, L. Yang, C.-C. Chen, H.-S. Kim, M. J. Han, W. Luo, Z. Feng, M. Upton, D. Casa, J. Kim, et al., Physical review letters, vol. 116, no. 21, p. 216 402, 2016.

[137] N. A. Benedek and C. J. Fennie, Physical review letters, vol. 106, no. 10, p. 107 204, 2011.

[138] A. McLeod, A. Wieteska, G Chiriaco, B Foutty, Z Rui, Y Yuan, V. Millis AJ Gopalan, Z. Mao, L. Chen, A. Pasupathy, and D. Basov, 2021.

[139] A. Gangshettiwar, Y. Zhu, Z. Jiang, J. Peng, Y. Wang, J. He, J. Zhou, Z. Mao, and K. Lai, Physical Review B, vol. 101, no. 20, p. 201 106, 2020.

[140] .

[141] Q. Han, Ph.D. dissertation, Columbia University, 2019.

[142] M. Rozenberg, I. Inoue, and M. Sanchez, Physical review letters, vol. 92, no. 17, p. 178 302, 2004.

[143] I. H. Inoue and M. J. Rozenberg, Advanced Functional Materials, vol. 18, no. 16, pp. 2289–2292, 2008.

[144] W. Shi, J. Ye, Y. Zhang, R. Suzuki, M. Yoshida, J. Miyazaki, N. Inoue, Y. Saito, and Y. Iwasa, Scientific reports, vol. 5, no. 1, pp. 1–10, 2015.

[145] Y. Cao, V. Fatemi, S. Fang, K. Watanabe, T. Taniguchi, E. Kaxiras, and P. Jarillo-Herrero, Nature, vol. 556, no. 7699, pp. 43–50, 2018.

[146] A. L. Sharpe, E. J. Fox, A. W. Barnard, J. Finney, K. Watanabe, T. Taniguchi, M. Kastner, and D. Goldhaber-Gordon, Science, vol. 365, no. 6453, pp. 605–608, 2019.

[147] B. Huang, G. Clark, D. R. Klein, D. MacNeill, E. Navarro-Moratalla, K. L. Seyler, N. Wilson, M. A. McGuire, D. H. Cobden, D. Xiao, et al., Nature nanotechnology, vol. 13, no. 7, pp. 544–548, 2018.

[148] A. Ghiotto, E.-M. Shih, G. S. Pereira, D. A. Rhodes, B. Kim, J. Zang, A. J. Millis, K. Watanabe, T. Taniguchi, J. C. Hone, et al., arXiv preprint arXiv:2103.09796, 2021.

[149] Y. Cao, V. Fatemi, A. Demir, S. Fang, S. L. Tomarken, J. Y. Luo, J. D. Sanchez-Yamagishi, K. Watanabe, T. Taniguchi, E. Kaxiras, et al., Nature, vol. 556, no. 7699, pp. 80–84, 2018.

[150] K. F. Mak, C. H. Lui, J. Shan, and T. F. Heinz, Physical review letters, vol. 102, no. 25, p. 256 405, 2009.

[151] L. Li, E. O'Farrell, K. Loh, G. Eda, B Özyilmaz, and A. C. Neto, Nature, vol. 529, no. 7585, pp. 185–189, 2016.

[152] X. Xi, H. Berger, L. Forró, J. Shan, and K. F. Mak, Physical review letters, vol. 117, no. 10, p. 106 801, 2016.

[153] G. Meijer, Science, vol. 319, no. 5870, pp. 1625–1626, 2008.

[154] A. M. Waser R., Nanoscience And Technology: A Collection, pp. 158–165, 2010.

[155] T. Kanki, K. Kawatani, H. Takami, and H. Tanaka, Applied Physics Letters, vol. 101, no. 24, p. 243 118, 2012.

[156] C. Alexander, G Cao, V Dobrosavljevic, S McCall, J. Crow, E Lochner, and R. Guertin, Physical Review B, vol. 60, no. 12, R8422, 1999.

[157] H. Fukazawa and Y. Maeno, Journal of the Physical Society of Japan, vol. 70, no. 2, pp. 460–467, 2001.

[158] R. Vitalone, B. Foutty, A. McLeod, J. Wieteska, C. Sow, F. Nakamura, Y. Maeno, A. Pasupathy, and D. Basov, vol. 2019, 2019, H07–007.

[159] T. e. a. Zou, Journal of Physics: Condensed Matter, vol. 31, no. 19, p. 195 602, 2019.